Alma Mater Studiorum · Università di Bologna

Scuola di Scienze
Corso di Laurea Magistrale in Fisica del Sistema Terra

Study of anabatic flows using large-eddy simulations in a simplified geometry

Relatore:
Prof. Silvana Di Sabatino

Presentata da:
Dario Di Santo

Correlatore:
Dott. Carlo Cintolesi

Sessione III
Anno Accademico 2018/2019

Abstract

English version

Buoyancy driven flows along a slope are a common feature in complex terrain and can strongly affect the dynamics of the troposphere. In the last decades, there has been an increasing interest in these small scale circulation phenomena and near-surface turbulent processes, also in light of their influence in the planetary boundary layer dynamics. Among them, the katabatic wind (downslope flow) has been extensively studied, while less attention has been given to the anabatic wind (upslope flow). Investigations have been typically carried out through field and laboratory experiments, however there is an increasing interest towards numerical simulations. These allow a detailed analysis under controlled geometrical and physical conditions in order to highlight the fundamental mechanisms that are not yet fully understood. A better knowledge of such mechanisms will be beneficial for a number of applications at different scales: from the tuning of meteorological models to improve weather predictions to the evaluation of the ventilation and pollutant transport in urban areas. Anabatic flow arises, for example, over heated mountains, where the upward buoyancy force drives the flow along the slope. This is typical in an early morning configuration when the rise of the sun rapidly heats up the terrain. The flow rises from the slope bottom, increasing in intensity and in turbulence content along the slope and confined to a short region near the surface, where velocity reaches a maximum and rapidly decreases along the normal-slope direction.

In the present work, the turbulent anabatic flow generated over a uniformly heated slope in neutral stratification is originally studied through a large-eddy simulation (LES) technique. The LES directly resolves the large scale of motion (highly energetic), modelling the smaller scales. This methodology is in between the direct numerical simulations (DNS), which resolve all the scales, and the Reynolds-averaged Navier-Stokes (RANS) simulations, that just reproduce the main flow. The LES leads to a time-dependent simulation with a lower computational cost than the former and more accurate results compared to the latter given that small scales of motion exhibit universal features and can be modelled more accurately.

The present study is, to the best of the author's knowledge, the first case of a LES applied to anabatic flows in neutral stratification. The simulation

approach is succesfully validated against three data sets: experimental, DNS and theoretical. One of the primary objectives of the study is to characterise the instantaneous turbulent structures triggered by the vertical buoyancy force responsible for the increase the turbulent mixing in the boundary layer. Such structures are hardly detected in both field and laboratory experiments and cannot be reproduced by steady-state numerical simulations. A new expression of the characteristic length scale of the thermal boundary layer is proposed and applied to derive alternative scaling parameters. Three principal regions are detected in the near-surface temperature profiles: a conduction region that contains most of the temperature decrease, a convective region dominated by flow convection and an equilibrium region that is almost not influenced by the heated slope. The newly proposed length scale resulted to be linked to the evolution of instantaneous turbulent structures identified as Rayleigh-Taylor instabilities which are analyzed and described. Their characteristic frequency is determined through a spectral analysis and their geometric dimensions are studied and linked to the extension of the vertical mixing zone inside the convection region. Three simulations are performed at different Rayleigh numbers to understand if there is a critical value above which the anabatic flow results Rayleigh-independent. the sensitivity analysis is carried out concluding that the analyzed flows are not Rayleigh-independent.

Italian version

I flussi guidati dalla buoyancy lungo un pendio sono fenomeni tipici dei terreni di orografia complessa e possono influenzare fortemente la dinamica della troposfera. Negli ultimi decenni, c'è stato un crescente interesse per fenomeni di circolazione su questi processi turbolenti a piccola scala in prossimità della superficie, anche alla luce della loro influenza nella dinamica dello strato limite planetario. Tra questi, il vento catabatico (flusso in discesa) è stato ampiamente studiato, mentre minore attenzione è stata data al vento anabatico (flusso in salita). Le indagini sono state tipicamente condotte attraverso esperimenti sul campo e in laboratorio, anche se c'è una crescente attenzione alle simulazioni numeriche. Queste ultime permettono un'analisi dettagliata in condizioni geometriche e fisiche controllate per evidenziare i meccanismi fondamentali che governano la fisica atmosferica, non ancora pienamente compresi. Una migliore conoscenza di tali meccanismi sarà utile per una serie di applicazioni a diverse scale: dalla messa a punto di modelli meteorologici per migliorare le previsioni meteorologiche, alla valutazione della ventilazione delle aree urbane e del trasporto degli inquinanti. Il flusso anabatico può nascere, ad esempio, sopra una montagna riscaldata, dove la forza di galleggiametno verso l'alto spinge il flusso lungo il pendio. Si tratta di una tipica configurazione mattutina, quando il sorgere del sole riscalda rapidamente il terreno. Il flusso sale dal fondo del pendio, aumentando di intensità e di contenuto di turbolenza lungo il pendio stesso. È confinato in una breve regione vicino alla superficie, dove la velocità raggiunge il massimo e diminuisce rapidamente lungo la dirzeione normale al pendio.

Nel presente lavoro, il flusso turbolento anabatico generato su un pendio uniformemente riscaldato in stratificazione neutra, viene studiato attraverso una tecnica di large-eddy simulation (LES). Il LES risolve direttamente le grandi scale del moto (altamente energetico), modellando le scale più piccole. Questa metodologia si colloca tra le direct numerical simulations (DNS), che risolvono tutte le scale, e le simulazioni Reynolds-averaged Navier-Stokes (RANS), che riproducono solo il flusso principale. Il LES porta ad una simulazione time-dependent, con un costo di calcolo inferiore rispetto al primo e risultati più accurati rispetto al secondo, dato che le piccole scale di movimento presentano caratteristiche universali e possono essere modellate in modo più accurato.

Il presente studio è, per quanto a conoscenza dell'autore, il primo caso di un LES applicato a flussi anabatici in stratificazione neutra. Il modello Smagorinsky utilizzato è validato con successo tramite il confronto con tre serie di dati: sperimentale, DNS e teorico. Uno degli obiettivi primari dello studio è quello

di caratterizzare le strutture turbolente istantanee innescate dal galleggiamento verticale forceresponsibile per l'aumento della miscelazione turbolenta nello strato limite. Tali strutture sono difficilmente rilevabili sia negli esperimenti sul campo che in laboratorio e non possono essere riprodotte da simulazioni numeriche a stato stazionario.

Una nuova espressione della scala di lunghezza caratteristica del thermal boundary layer viene proposta e applicata per ricavare parametri di scala alternativi. Tre regioni principali sono rilevate nei profili di temperatura vicino alla superficie: una regione di conduzione che contiene la maggior parte della decrescita della temperatura, una regione convettiva dominata dalla convezione di flusso e una regione di equilibrio che risulta quasi non influenzata dalla superficie riscaldata. La nuova scala di lunghezza proposta è risultata essere legata all'evoluzione delle strutture turbulente istantanee identificate come instabilità di Rayleigh-Taylor che vengono analizzate e descritte. La loro frequenza caratteristica è determinata attraverso un'analisi spettrale e le loro dimensioni geometriche sono studiate e collegate all'estensione della zona di mixing verticale all'interno della regione di convezione. Vengono effettuate tre simulazioni a diversi numeri di Rayleigh per capire se esiste un valore critico oltre cui il flusso anabatico risulta indipendente da Rayleigh. L'analisi di sensitivity viene effettuata concludendo che i flussi analizzati non sono indipendenti da Rayleigh.

Contents

List of Figures

List of Tables

Introduction

魔風, Mafū, lit. devilish wind, the Oroshi wind which causes unpredictable damage (Masasumi Tobikura, 1853).

Description

The developing of wind breezes over mountainous terrain is a phoenomena observed since ancient times. This particular kind of winds forms locally near the surface over complex orography such as mountains or valleys, in which heat fluxes are involved.

Even though these local winds can function as accelerators for large scale winds that develop in pressure systems and passes through complex topographies, their dynamic is totally independent from the synoptic scale flows. Instead, they are principally driven by the diurnal cycle which continuously modifies the local

temperature gradients that form along the orography. During the day, heated slopes generate low pressures zones over them. The low pressure folds isothermal surfaces above the ground and draws in, from the plain level, the air masses, producing anabatic wind (anabatic, from the greek "*ἀναβατικός*", ascending). During the night, cooling of the slopes has the opposite effect: the buoyancy of the fluid above the slopes results modified in such a way that the air masses tend to fall from the mountain under gravity, producing katabatic wind (from the greek "*καταβατός*", descending). This is analogous to what happens in the probably more notorious sea-land breeze configuration (see Figure 1).

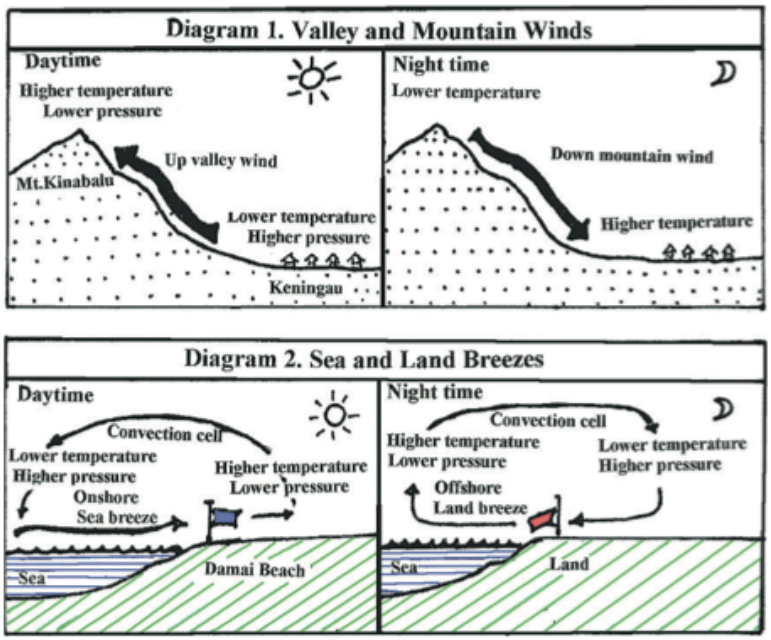

Figure 1: Schematic mechanism of slope winds and sea breezes.

In real situations, this simplified scheme should include many more factors: the surface stresses, the heat fluxes, the atmosphere stratification, the slope angle, the actual orographic geometry and roughness, the differential heating, the presence of vegetation, ice, a nearby ocean or lake and many other tangles. Resounding examples of downslope winds that also have a strong impact on human life are the Bora that develops in the seaside mountain chain of Croazia and reaches Adriatic Sea, the Bohemian wind that descends the Ore mountains, Santa Ana winds of South California, the Japanese Oroshi across the Kanto Plain and also the dreadful Antarctic fall winds that can reach and exceed 300 km/h (Figure 2). Upslope winds generally are the cause of cumulus that form even in clear sky conditions above the mountain peaks, as it often happens in the Great Mountain of Utah or Hawaiian Islands (Figure 3).

Figure 2: Katabatic wind at Commonwealth Bay.

Figure 3: Anabatic cumulus clouds over Hawaiian islands.

Research questions

Slope winds strongly affect the mesoscale dynamic over complex terrain. Considering that the vast majority of urban areas is located in proximity of such kind of regions, our capability of understanding such phenomena directly affects our ability to understand, predict and handle urban meteorological and climate scenarios.

It is known in literature (Banta, 1984; Hanley et al., 2011; Chao, 2012) that

accounting for the heat carried by separated flow in thermally driven circulation is important to correctly predict precipitation, moisture distribution and unsteady phenomena over orographic terrains. From an urban standpoint it has been shown (Ellis et al., 2000) that upslope wind transports urban pollution plumes over mountains and, when flow separation occurs, pollutant are lofted forming a recirculating flow within the convective boundary layer (Lu and Turco, 1994; Reuten, Steyn, and Allen, 2007; De Wekker, 2008; Fernando, 2008; Serafin and Zardi, 2010b; Serafin and Zardi, 2010a). In case the separation does not occurs, pollutants tend to return back to the cities with downslope winds at night (Fernando et al., 2001). Flow separation is also important to be taken into account for safety in aviation (Politovich et al., 2011), especially because it can makes challenging take-off maneuvers. Even though these flows are known from ancient times, their comprehension is strongly linked to the progresses of the tools available for their study. For example, numerical solutions for anabatic and katabatic flows are sensitive to the turbulent model that is employed. The treatment of these flows is therefore strictly related to the efforts in developing a good closure for numerical models.

The numerical approach to these dynamic problems is relatively young. Numerical simulations allows to generate results under full control of each of the physical and geometrical conditions, thus providing an optimal tool of investigation to combine with experiments, for which it is difficult to reach such conditions. Recently, the large-eddy simulation (LES) method began to spread, because it allow to study transitional phenomena and instantaneous turbulent structure that other numerical methods cannot enable to see and because they are less expensive than a Direct Numerical Simulation (DNS) and more accurate than a Raynolds-Averaged Navier-Stokes (RANS) simulation. This also means that problems, which were too much expensive to afford with a DNS, can be investigated thanks to the LES approach. In the field of natural convection, however, the LES method is difficult to accomplish, because, in order to be correctly reproduced, this dynamics requires accurate numerical schemes and realistic turbulent models. To the best of the author knowledge, few numerical simulations are found in literature about the slope wind subject, even less simulations treat slope winds in neutral stratification and no article has been found about LES performed over anabatic flows.

The new possibilities of investigating problems that could not be properly simulated in the past are still now shaping the scientific knowledge of fluid dynamics.

Literature review

One of the first theories of upslope wind (Wenger, 1923) makes use of the Bjerknes theorem for describing them as the lower part of a closed circulation wheel generated in a baroclinic atmosphere. Later on, a multitude of theories laid the foundations for the actual understanding of the involved mechanisms.
Prandtl's theoretical model (Prandtl, 1942) is the most common starting point still utilized today for comparison with modern results: it considered steady laminar flow over an infinite plate in a stratified atmosphere with Boussinesq approximation, and provide analytical solution for both velocity and temperature; Defant (1951) added non stationarity, simulating the diurnal cycle; Egger (1981) considered inhomogeneous heating over the slope; Ye, Segal, and Pielke (1987) introduced a finite depth boundary layer with varying eddy viscosity; Kuwagata and Kondo (1989) exploited a one layer hydraulic model with integrally averaged equations; Crook and Tucker (2005) analysis considered the transition between flow staying along-slope and flow separation from the slope in terms of the balance between vorticity of the upslope heated flow and vorticity generated by the baroclinity of the atmosphere.

From the earlier studies, a combination of both the implementation of numerical models and analytical approaches provide a lot of useful information for testing and developing future models. Some of those are currently considered well established knowledge: Orville (1964) was one of the first that identified features of the upslope surface layer, in particular his layer thickness increasing uphill and the anti-slope current aloft, compensating the flow at plain level and making a cell circulation pattern; Brown (1980) observed coherent pattern of convective cells with longitudinal rolls and explained them in terms of dynamical instabilities of velocity profiles with an inflection point; Bader and McKee (1983) interpreted heat transmission to the whole volume of the fluid in terms of gravity waves generated when heat flux provided by surface became sufficient to penetrate the overlying stratification; Segal, Ookuchi, and Pielke (1987) found that maximum velocity depends linearly on heat flux and slope angle as $sin\alpha$ and results instead fairly independent from background stratification; Schumann (1990) studied the fine structure of turbulence identifying transverse roll vortexes starting from small slopes and longitudinal roll vortexes starting only at large angles. More recently, Allen and Brown (2006) showed that instability reduces speed-up and pressure drag for low hills, while for hills steep enough for separation to happen in neutral conditions, instability reduces the strength and size of separated bubble, but pressure drag is almost independent from it; Princevac, Hunt, and Fernando (2008) found that the initial transient decaying quasi-stationary oscillatory pattern of the spatially integrated variables have a normalized oscillation frequency proportional

to the slope angle; furthermore Princevac and Fernando (2008) found that stable stratification tends to suppress separation of the flow; Grisogono et al. (2014) found maximum velocity height to be proportional to the slope angle as well; Shapiro and Fedorovich (2014) derived scaling relations that eliminates dependency of the solution on slope angle; Shapiro and Fedorovich (2017) also associated rapid dumping of integral oscillations in laminar Prandtl flow with the surface stress term's action; Oldroyd et al. (2016) observed slope-normal fluxes.

More recently, numerical approaches have been successful in gaining more knowledge on this topic, and pushing the science capability to answer more questions: other phenomena have been issued, like transitional fronts (Hunt, Fernando, and Princevac, 2003); Grisogono and Axelsen, 2009), effects of varying slope angle (Smith and Skyllingstad, 2005), transferring mechanisms of heating through air circulation (Noppel and Fiedler, 2002) application of more realistic turbulent diffusivity models (Giometto et al., 2017a), introduction of Coriolis effects (Shapiro and Fedorovich, 2008), study on the time dependence of solution (Zardi and Serafin, 2015).

Direct numerical simulations has been done by Fedorovich and Shapiro (2009), which simulated a stratified fluid along steep slopes parametrized through an integral Reynolds number; in another work the same authors (2009) studied natural convection along a vertical plate; Giometto et al. (2017) simulated a turbulent slope flow analysis in terms of the Grashof number.

Within the large-eddy simulations framework, from the pioneering work of Schumann, other works explored the possibilities of studying the fine scale structure of turbulence, such as Skyllingstad (2003) and Axelsen and van Dop (Axelsen and van Dop, 2009a; Axelsen and van Dop, 2009b) which focused on the analysis of the bulk solution's sensitivity to various parameters; Chow et al. (2006) compared their simulation with surface and radiosonde observations on Swiss Alpine valley issuing the need of high-resolution surface datasets for best results; Chemel, Staquet, and Largeron (2009) compared the along-slope oscillations and the generated internal gravity waves by katabatic winds in an idealized Alpine valley, showing that oscillations near the slope do not propagate inside the fluid; Lehner and Witheman (2012) simulated a spatially and temporally varying heat flux and studied the formation of a double circulation cell's pattern in the case of background wind; Burns and Chemel (2015) as well as Arduini, Staquet, and Chemel (2016) studied the interaction between a downslope flow and a region of developing cold air pool inside a valley.

Even though this studies has gathered some information, the field of anabatic and katabatic winds on slope or valley systems is still dynamically shaping itself and continuously developing. Cheng-Nian and S. (2019) studied the stability of

Prandtl model, identifying transverse modes as stationary vortical flow structures aligned in the along-slope direction, and longitudinal modes emerged as waves propagating in the base-flow direction; Łobocki (2017) showed that exchanges between potential energy of mean flow and total turbulent mechanical energy are controlled by potential temperature gradient's inclination; Shapiro (2016) presented a theory for the Great plains low-level jets, in which the jet emerges in the slope boundary layer as the nocturnal phase of an oscillation arising from diurnal variations in turbulent diffusivity (i.e. Blackadar mechanism) and surface buoyancy (i.e. Holton mechanism); Everard et al. (2018) builted a new closure model for simulating katabatic flows; Giometto et al. (2016) generalized for katabatic flows the Niewstadt closed-form solution for the stationary Ekman layer for spatially varying eddy viscosity and diffusivity, and constant Pr number; Hang et al. (2018) modified Monin-Obukhov similarity function for katabatic flows; Ingel (2018) studied the limit to the case of zero angle of the classical Prandtl solution showning that no paradoxes arise if ones do not consider buoyancy sources of infinite spatial scale; Ingel (2018) also generalized Prandtl model for an homogeneous stationary source of heavy admixture that significantly changes the medium density; Lebonnois et al. (2018) studied the planet boundary layer's slope winds observed on Venus surface.

Chapter 1

Theoretical background

1.1 Dynamics equations

Before entering the topic of this thesis, it will be presented a brief review of the basic mathematical elements of fluid dynamics, which will be widely implemented in the discussion. It will be used an Eulerian framework described in local tangent plane coordinates (x, y, z) jointed with an air particle moving on the earth surface, having x and y the directions $\hat{i}$ along longitude (positive eastward) and $\hat{j}$ along latitude (positive northward) respectively, while $\hat{k}$ is normal to the surface and positive in the outgoing direction (Figure 1.1).

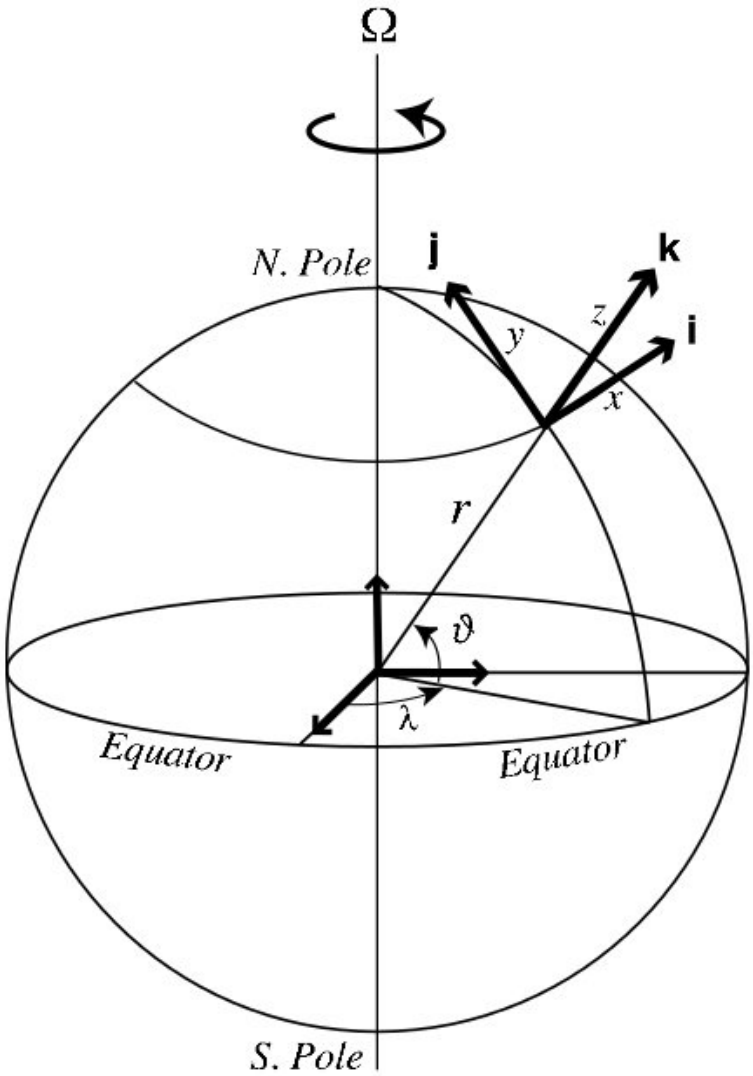

Figure 1.1: Local tangent plane coordinate system.

Velocity of the fluid parcel will be denoted by using the tensorial expression u_i indicating the generic i-component for $i = 1, 2, 3$ (for more details on the tensorial formalism, see Kundu and Cohen, 2001 for reference). It will be assumed neglectable the Coriolis force that would normally appear if one considers the Earth's rotation effect, i.e. the term $\epsilon_{ij3} f u_j$ (where f is the Coriolis frequency and ϵ indicates the

Levi-Civita symbol for product vector in tensorial notation). This is typical in the study of slope winds and the reason can be shown introducing the Rossby number $Ro = \frac{U}{fL}$, defined as a ratio between inertial forces acting on the particle and rotational force due to planetary angular momentum. Because length scales are smaller than mesoscale (10^3 m compared to 10^6 m), $f = 10^{-4}\text{s}^{-1}$ and typical U values are of the order of 1 m/s, Ro numbers are high, thus indicating that inertial forces are much stronger than Coriolis effect. This implies that winds interacting with the slope are *antitriptic*, i.e. solely determined by a balance between pressure gradient and friction.

1.1.1 Mass conservation

Being $\rho(x, y, z, t)$ the fluid density, $M = \int_V \rho dV$ the fluid mass inside a volume V, in absence of any sources of mass the principle of mass conservation implies $d_t M = 0$. Reynolds transport theorem (see, for example, Kundu and Cohen, 2001) defines the time derivative of an integral property inside a volume, by which mass conservation became:

$$\int_V (\partial_t \rho + \partial_k(\rho u_k)) dV = 0 \quad . \tag{1.1}$$

For the arbitrariness of choice of the volume V, the same condition must be verified by the argument of the integral:

$$\partial_t \rho + \partial_k(\rho u_k) = 0 \quad . \tag{1.2}$$

Assuming the density ρ constant and defining the material derivative as the operator $d_t = \partial_t + u_j \partial_j$, Equation (1.1) becomes:

$$\frac{1}{\rho} d_t \rho = -\partial_k u_k \quad , \tag{1.3}$$

which is the general form of the continuity equation.

1.1.2 Momentum equation

The general form of the momentum equation is expressed in terms of the symmetric stress tensor of surface forces τ_{ij} and the generic body force f_i, both applied to a fluid parcel of density ρ:

$$\rho d_t u_i = \partial_j \tau_{ij} + \rho f_i \quad . \tag{1.4}$$

The stress tensor τ_{ij} can be rewritten as the sum of an isotropic part, identified as the mechanical pressure $p(x, y, z, t) = -\frac{1}{3}\tau_{kk}(x, y, z, t)$, and his deviatoric part

$\tau_{ij}^d = \tau_{ij} - \frac{1}{3}\tau_{kk}\delta_{ij}$. In other words, it is writable as:

$$\tau_{ij} = -p\delta_{ij} + \tau_{ij}^d \quad . \tag{1.5}$$

Furthermore, in the case of Newtonian fluids, response to applied stress is linear, which implies:

$$\tau_{ij}^d = \mu(\partial_j u_i + \partial_i u_j - \frac{2}{3}\partial_k u_k) \quad ,$$

where μ is the dynamic viscosity coefficient with units of Pascal per second (see Kundu and Cohen, 2001 for the demonstration). Overall, considering gravity as the body force acting on the system antiparallel to the z axis, the momentum equation is called *Navier-Stokes equation* and reads as follows:

$$\rho d_t u_i = -\partial_i p + \partial_j(\mu(\partial_j u_i + \partial_i u_j - \frac{2}{3}\partial_k u_k)) - \rho g\delta_{i3} \quad . \tag{1.6}$$

Considering also incompressible fluids, for which $\partial_k u_k = 0$, this leads to write, together with the assumption that will be made from here on that μ is a constant, equation (1.6) becomes:

$$\rho d_t u_i = -\partial_i p + \mu\partial_j^2 u_i - \rho g\delta_{i3} \quad , \tag{1.7}$$

which is the simpler incompressible Navier-Stokes equation for homogeneous fluids.

1.2 Boussinesq approximation

Simpler equations are obtained considering the fluid incompressible, but completely neglecting the density variations makes impossible to describe thermal phenomena, such as convection. Therefore the Boussinesq approximation, which retains the density variations associated with the buoyancy of the fluid, is often used. Decomposing the density ρ as the sum of a reference value ρ_0 plus a deviation $\Delta\rho$, the momentum equation reads:

$$(\rho_0 + \Delta\rho) d_t u_i = -\partial_i p + \mu\partial_j^2 u_i - (\rho_0 + \Delta\rho) g\delta_{i3} \quad . \tag{1.8}$$

Recalling the hydrostatic balance, for which $0 = -\partial_i p + \rho_0 g\delta_{i3}$ on the $\hat{k}$ direction, it is also usually defined a new pressure $\tilde{p}$, which is the total pressure p deprived of the hydrostatic pressure. Equation (1.8) is then:

$$(\rho_0 + \Delta\rho) d_t u_i = -\partial_i \tilde{p} + \mu\partial_j^2 u_i - \Delta\rho g\delta_{i3} \quad . \tag{1.9}$$

If $\Delta\rho \ll \rho_0$, small density perturbations makes difference only for the gravity term $\Delta\rho g\delta_{i3}$ and, instead, have little impact on the acceleration term $\Delta\rho d_t u_i$. This is the

approximation of Boussinesq, for which the momentum equation can be written as:

$$d_t u_i = -\frac{1}{\rho_0}\partial_i \tilde{p} + \nu \partial_j^2 u_i - \frac{\Delta\rho}{\rho_0} g \delta_{i3} \quad , \tag{1.10}$$

where ν is the kinematic viscosity $\frac{1}{\rho_0}\mu$, in units of m^2/s.

1.3 Thermodynamic equations

1.3.1 Density and Temperature relation

Any substance has a density that can be generally written as a function $\rho = \rho(p, T)$ of the pressure p and temperature T state variables. The differential of the function $\rho(p, T)$ is $d\rho = \rho\alpha dp - \rho\beta dT$, from which are defined the isothermal compressibility coefficient

$$\alpha = \left(\frac{1}{\rho}\frac{\partial\rho}{\partial p}\right)_T \tag{1.11}$$

and the isobaric thermal expansivity coefficient

$$\beta = -\left(\frac{1}{\rho}\frac{\partial\rho}{\partial T}\right)_p \quad , \tag{1.12}$$

where subscripts T and p refers to taking a partial derivative at constant temperature T or pressure p, respectively.

Expanding the density ρ around a reference state (ρ_0, p_0, T_0) leads to

$$\rho = \rho_0 + \rho_0\alpha_0(p - p_0) - \rho_0\beta_0(T - T_0) + ... \quad . \tag{1.13}$$

In the water case, in a temperature range of 20-80 °C, the isothermal compressibility coefficient α is about 3.6×10^{-5} and the isobaric thermal expansivity coefficient β is about 2.1×10^{-4}), so that the Equation (1.13) can be approximated to: $\frac{\Delta\rho}{\rho_0} = -\beta\Delta T$.

Finally, it can be demonstrated (Tampieri, 2013) that pressure differences $\Delta p = p - p_0$ arising from motion are of the order of $\rho_0 u_i^2$. This implies that typical velocities u_i are many orders of magnitude smaller than p_0, so the term $-\frac{\Delta T}{T_0}$ dominates, i.e. the momentum equation (1.10) reads as

$$d_t u_i = -\frac{1}{\rho_0}\partial_i \tilde{p} + \nu \partial_j^2 u_i + \beta\Delta T g \delta_{i3} \quad . \tag{1.14}$$

This is the last form of the Navier-Stokes equation that will be used hereafter.

1.3.2 Energy equations

In order to find a conservation law for the energy, a brief recall of the first principle of thermodynamics is necessary. This principle relates variations of energy dU, heat dQ and work dL:

$$dU = dQ + dL \quad . \tag{1.15}$$

In a more general way, the energy variation dU can be viewed as the sum of two contributions: the variation of internal energy dE and of kinetic energy dK. Applying this decomposition, the time derivative of the first principle (Equation (1.15)) leads to

$$d_t L + d_t Q = d_t E + d_t K \quad , \tag{1.16}$$

which has the following integral form (Kundu and Cohen, 2001):

$$\int_V \left(\frac{1}{2}\rho d_t u^2 + \tau_{ij}\frac{1}{2}(d_j u_i + d_i u_j) \right) dV + \int_V -d_i q_i dV = \int_V \rho d_t \epsilon dV + \int_V \frac{1}{2}\rho d_t u^2 dV \quad , \tag{1.17}$$

where $q_i = -k d_i T$ is the heat flux through the unit area in the unit time and ϵ is the specific internal energy per unit mass. The first integral is composed by two terms: the first one, $\frac{1}{2}\rho d_t u^2$, is the work exerted by volume and surface forces to increase the kinetic energy; the second one, $\tau_{ij}\frac{1}{2}(d_j u_i + d_i u_j)$, is the work exerted by surface forces to increase the deformation of the volume.

For the arbitrariness of choice of the volume V, all arguments inside the integrals must balance as well:

$$\rho d_t \epsilon = -d_i q_i + \tau_{ij}\frac{1}{2}(d_j u_i + d_i u_j) \quad , \tag{1.18}$$

where the kinetic energy terms $\frac{1}{2}\rho d_t u^2$ were simplified on both sides. It can be shown that (Kundu and Cohen, 2001), using the Equation (1.5), the deformation work of the Equation (1.18) can be written as $\tau_{ij}\frac{1}{2}(d_j u_i + d_i u_j) = -p d_i u_i + \phi$, where

$$\phi = \mu\frac{1}{2}(d_j u_i + d_i u_j)(d_j u_i + d_i u_j) - \frac{2}{3}(d_i u_i)^2 \quad , \tag{1.19}$$

is a quantity related to the dynamic viscosity μ and it is always a positive term. In other words, the deformation work, consists of a reversible work of compression $-p d_i u_i$ and an irreversible work of viscous friction ϕ. Thus, the Equation (1.18) becomes

$$\rho d_t \epsilon = -d_i q_i - p d_i u_i + \phi \quad , \tag{1.20}$$

which is known as internal energy equation. An alternative form of this equation is

$$\rho d_t h = -d_i q_i + d_t p + \phi \quad . \tag{1.21}$$

where the specific enthalpy $h = \epsilon + \frac{p}{\rho}$ was used.

1.3.3 Temperature equations

For a general fluid under Boussinesq approximation, Equation (1.20) can be simplified, because incompressibility implies $\frac{1}{\rho} d_t \rho = 0$ and, in terms of volume variations, $d_t V = V(\partial_i u_i)$. Thus, the time derivative of internal energy written as a function of volume and temperature is:

$$d_t \epsilon = (\partial_T \epsilon)_V d_t T + (\partial_V \epsilon)_T d_t T \simeq c_v d_t T \quad , \tag{1.22}$$

where the approximation is due to the error made in the incompressibility assumption and becomes an equality for the ideal gases, in which internal energy can depend only on temperature.

Substituting the result of Equation (1.22) into the Equation (1.20) and explicitating Fourier equation $q_i = -k_T \partial_i T$, the expression (1.22) becomes a Temperature equation:

$$\rho c_v d_t T = k_T \partial_i^2 T + \phi \quad , \tag{1.23}$$

in which appears the thermal conductivity k_T. Furthermore, a scaling analysis shows that ϕ is neglectable:

$$\frac{\phi}{\rho c_p d_t T} \simeq \frac{\mu u^2 / L^2}{\rho c_p \delta T u / L} = \frac{\nu u}{c_p L \delta T} \quad , \tag{1.24}$$

in which, for the water case, the dynamic viscosity ν is 10^-6 m^2/s, the specific heat c_p is 3.68×10^3 J/kg K and the ratio ν / c_p is significantly small.

Shapiro and Fedorovich (2004) made some observations about the temperature equation used over unsteady convectively driven flow over a vertical plate immersed in a stratified fluid. Even in their work, it is pointed out that viscous dissipation is smaller than other terms, including pressure work, so that the irreversible term ϕ disappears. More importantly, they shown that the error in assuming pressure work neglectable (i.e. the Boussinesq approximation) is of the same order of magnitude of considering constant the properties k and ν (Shapiro and Fedorovich, 2004).

In this framework of hypothesis, the Equation (1.23) becomes:

$$d_t T = \frac{k_T}{\rho c_v} \partial_i^2 T \quad , \tag{1.25}$$

which is the diffusion equation for temperature in absence of any other sources of heat.

1.3.4 Buoyancy equation

A density variation $\Delta\rho$ will be associated to a temperature variation $\Delta T = T - T_0$, which can be inserted into the Equation (1.25) leading to:

$$d_t \Delta T = \frac{k_T}{\rho c_v} \partial_i^2 \Delta T + (k_T \partial_i^2 T_0 - u_j \partial_j T_0) \quad . \tag{1.26}$$

A constant value for T_0 gives zero for the term inside the parenthesis. Now multiplying by $-g_i\beta$ and assuming β as constant, a buoyancy equation is obtained:

$$d_t(g_i\beta\Delta T) = \frac{k_T}{\rho c_v} \partial_i^2 (g_i\beta\Delta T) \quad , \tag{1.27}$$

where $g_i\beta\Delta T$ is the buoyancy field also denoted as b. This quantity will be the starting point for investigating the mechanisms of natural convection over heated slopes in Chapter 3.

1.3.5 Potential temperature equation

Often, in meteorology, the need of accounting for the pressure variation in the measured temperature profiles leads to define a new variable: the *potential temperature*. The temperature equation (1.23) with neglected dissipation ϕ, but retained pressure work, reads as:

$$\rho c_p d_t T = -k_T d_i^2 T + d_t p \quad . \tag{1.28}$$

In order to account for the change in temperature due to pressure variations, material derivative of temperature T and pressure work $d_t p$ are combined together into this single variable, the potential temperature θ, defined as:

$$\theta = T \left(\frac{p_s}{p} \right)^{\frac{R_d}{c_p}} \quad , \tag{1.29}$$

where R_d is the gas constant of dry air and p_s is a reference pressure. Temperature equation (1.28) is thus often rewritten as:

$$\rho c_p d_t T - d_t p = \rho c_p T d_t ln(\theta) = -k_T d_i^2 T \quad . \tag{1.30}$$

Such definition implies that potential temperature is the temperature that a fluid parcel would have if brought from pressure p to the reference pressure p_s through an adiabatic process. As Shapiro and Fedorovich (2003, 2004) point out, pressure only has a small impact and is neglected in Boussinesq approximation, regardless from the distinction between considering air or water. Thus, hereafter, temperature

T and potential temperature θ will be two interchangeable variables.

1.4 Vorticity equation

As will be discussed in Chapter 3, the *vorticity* of the fluid has a major role in the slope winds mechanism. This Section will discuss the strong realtion between the thermal nature of the problem and vorticity.

Vorticity is defined as $\omega = \nabla \times u$ and is related (see Kundu and Cohen, 2001) to the rotational tensor $d_j u_i - d_i u_j$ such that it represents a local measure of the instantaneous velocity rotation of the fluid. In tensorial notation, using the permutation symbol e_{ijk} (see Kundu and Cohen, 2001), it writes

$$\omega = e_{ijk}\partial_j u_k \quad .$$

Writing the Navier-Stokes equation in a non-rotating reference frame as

$$\partial_t u_k + u_l \partial_l u_k = -\frac{1}{\rho}\partial_k p - \partial_k(gz) + \nu(\nabla^2 u_k + \frac{1}{3}\frac{\partial^2 u_l}{\partial x_k \partial x_l}) \quad , \tag{1.31}$$

reformulating the advection term as

$$u_l \partial_l u_k = -e_{klm} u_l \omega_m + \frac{1}{2}\partial_k^2 u \quad , \tag{1.32}$$

and applying the rotor operator $e_{ijk}\partial_j$, the vorticity equation is obtained:

$$\partial_t \omega_i - \nabla \times (u \times \omega) = \frac{1}{\rho^2} e_{ijk}\partial_j \rho \partial_k p + \nu \nabla^2 \omega_i \quad . \tag{1.33}$$

The first term on the right-hand side is zero if the fluid is *barotropic* (i.e. if density is only a function of pressure), in which surfaces of constant density are also surfaces of constant pressure, thus the gradients are parallel to each others. However, this is not the case in thermal convection problems, such the one that concerns the topic of this work. A fluid whose density depends on temperature is called barocline and, in this case, the resultant torque of the non-parallel gradients generates rotation inside the fluid (Figure 1.2).

Another way to express the baroclinicity in the vorticity equation is in terms of the buoyancy force acting on the fluid parcel, as it appears in Hocut, Liberzon, and Fernando (2015):

$$\partial_t \omega_i + u\nabla\omega = \omega\nabla u + \nabla \times (b\hat{k}) + \nu\nabla^2\omega \quad . \tag{1.34}$$

The role of buoyancy in the vorticity production and how this leads to the generation

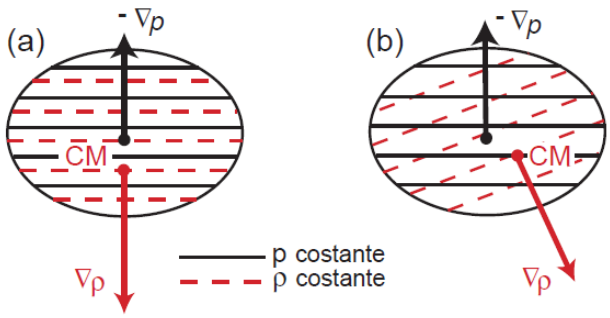

Figure 1.2: Baroclinic torque generation of vorticity (Bonafede, Nov. 2016).

of slope flows will be recovered in Section 3.1.

1.5 Non-dimensional equations and scale analysis

The procedure of adimensionalization for a generic variable G consists in writing it in the form $G_r G^*$, where G_r is a reference value which represents the *unit measure* of G, containing the dimensional information, and G^* is the adimensional value of G, of which represents the *measure*. In this way it is possible to characterize the dynamics of the problem with universal scales that do not depend upon the specific values of the problem. Choosing our problem to be represented by the length scale L, the velocity scale U, and the buoyancy scale $N = (\frac{1}{\rho_0} d_z \rho(z))^{\frac{1}{2}}$, each term of the Navier-Stokes equation (1.10) can be rewritten as:

$$d_t u_i = \frac{U^2}{L} d_t u_i^* \quad , \tag{1.35}$$

$$\partial_i \tilde{p} = \rho_0 U^2 \partial_i \tilde{p}^* \quad , \tag{1.36}$$

$$\partial_j^2 u_i = \frac{U}{L^2} \partial_j^2 u_i^* \quad , \tag{1.37}$$

$$\frac{\Delta\rho}{\rho_0} g_i = L N^2 \Delta\rho^* \quad . \tag{1.38}$$

Dividing each therm for $\frac{L}{U^2}$, the Equation (1.10) assumes the following non-dimensional form:

$$d_t u_i^* = -\partial_i \tilde{p}^* + Re^{-1} \partial_j^2 u_i^* + Fr^{-2} \Delta\rho^* \quad , \tag{1.39}$$

where two adimensional numbers that characterize the dynamic of the fluid has been introduced: the Reynolds number $Re = \frac{UL}{\nu}$, which is the ratio between inertial

and viscous forces acting on the fluid, and the Froude number $Fr = \frac{U}{NL}$, which is the ratio between inertial and gravity forces.

Using also the temperature scale T, the T-equation (1.25) became:

$$d_t T = Pr Re^{-1} \partial_i^2 T \quad , \tag{1.40}$$

where Pr is the Prandtl number, defined as:

$$Pr = \frac{\nu}{D} \quad , \tag{1.41}$$

where $D = \frac{k_T}{\rho c_v}$ is the thermal diffusion coefficient.

Another number regarding the buoyancy force in free convection is the Grashof number, defined as the ratio between buoyancy and viscous forces:

$$Gr = \frac{g \beta_T \Delta T L^3}{\nu} \quad , \tag{1.42}$$

where β_T is the fuid thermal expansion coeffcient, L is the characteristic length, and $\Delta T = (T_{\text{surface}} - T_\infty)$ is the system difference of temperature between the heated surface and the environment.

From this number can be derived the Rayleigh number, which is also non-dimensional and strongly related to the natural convection problems such as the one discussed in this work. It can be defined as the product between the Grashof number and the Prandtl number, i.e.:

$$Ra = \frac{g k_T T \beta_T L^3}{\nu D} \quad . \tag{1.43}$$

The Rayleigh number can be interpreted as the ratio between the time scale of thermal diffusion and that one of the thermal convection. Depending on the problem, there is a critical value above which turbulence is triggered and another one below which there is no fluid motion and heat is transferred by conduction rather than convection. The critical Ra at which the natural convection starts depends from the case geometry and the boundary conditions: in a convective motion between parallel plates, the critical value is $Ra_c = 1708$. Notice that this non-dimensional number is particularly sensitive to the characteristic length, which appears in equation 1.43 to the power third. Instead, there is a linear dependency from the difference of temperature; hence, it has a limited influence on the first order of magnitude.

Typical scale values for the principal non-dimensional quantities inside an atmospheric boundary layer are $U \simeq 10$ ms^{-1}, $L \simeq 1000$ m, $N \simeq 10^{-2}$ s^{-1}, so that $Re \simeq 10^9$, $Fr \simeq 1$, $Ra \simeq 10^{17}$ and viscous term results small compared to the

inertial advection and pressure gradient.

1.6 Turbulence

1.6.1 Main features of turbulence

As the Reynolds number *Re* that characterizes the fluid increases, the inertial non-linear term becomes progressively more important compared to the viscous forces acting on the fluid. Intrinsic instabilities begin to rise and each one of them can be assumed acting as an harmonic perturbation with a characteristic frequency. When *Re* number is large enough, the overlap of all the instability frequencies acts as fluctuations over the mean motion that can be modelled as a stochastic behaviour. The superposition of this dynamical structures (the *eddies*), each one characterized by a different temporal and length scale, is called *turbulent flux*.

Fluid's particles that moves in space as a fluctuation of the mean motion, preserve the temperature and momentum of their original positions. This means that turbulence acts inside the fluid as a transport of momentum and heat, as well as any other property that undergoes fluctuations from the mean value.

Because of this transport role, the presence of shear inside a fluid drives turbulence eddies to act as a flux that diffuses properties, mixing them and smoothing any gradient inside the fluid.

Diffusing efficiency of turbulence is many order of magnitude stronger than molecular diffusion and, as such, when turbulence is fully developed, molecular diffusion and viscosity are neglectable for the biggest eddies.

For the same physical mechanisms that act on the mean flow, eddies can have fluctuations themselves, generating sub-scale eddies that generate other eddies and so on, until viscosity becomes no more neglectable, blocking the eddies cascade and dissipating energy into heat (Figure 1.3. Travel of energy in this process can be understood from the kinetic energy equations that will be described in Section 1.6.5, but as a general rule it is well acknowledged that first eddies extract energy directly from the mean flow. Subscales eddies takes instead energy from the eddies that generate them, thus the energy is transferred up to the smallest scales without significant dissipation, where heat came into play. Thus an energy cascade corresponds univocally to the eddies cascade (even though there are cases in which the energy goes up from the small eddies to larger ones).

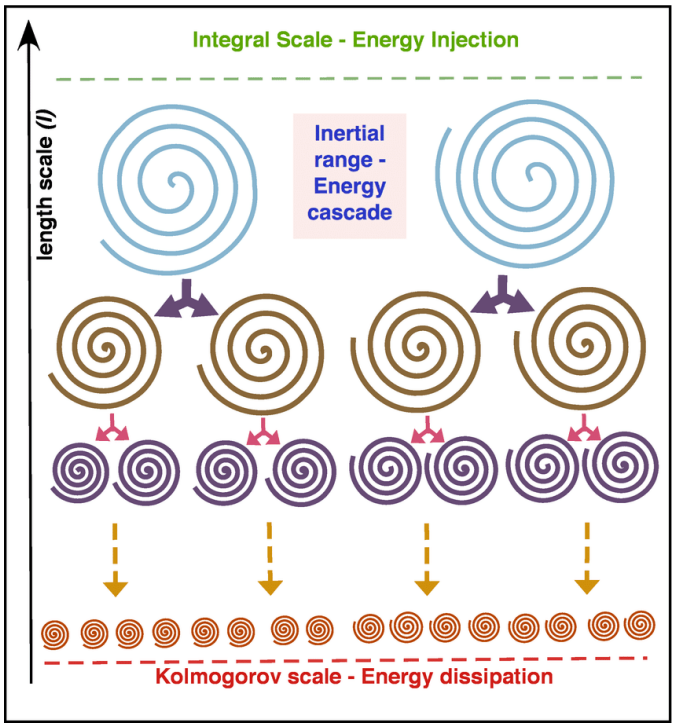

Figure 1.3: Sketch of the energy cascade (Banerjee, Nov. 2014).

1.6.2 Statistical approach

Consider a generic meteorological time series obtained from sampling a velocity variable $u_i(x_j, t)$, as depicted in Figure 1.4. From this signal, it is possible to define a mean value $\overline{u_i}(x_j)$ and fluctuations around that value $u_i'(x_j, t) = u_i(x_j, t) - \overline{u_i}$.

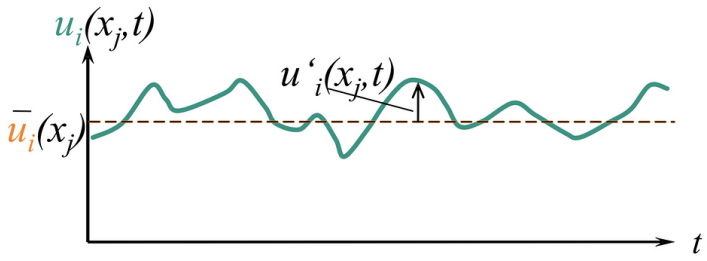

Figure 1.4: Conceptual sketch of mean value and fluctuation of a variable $u_i(x_j, t)$.

Covariances are defined as

$$\mathrm{Cov}(\zeta_1, \zeta_2) = \int_{-\infty}^{\infty} (\zeta_1 - \overline{\zeta}_1)(\zeta_2 - \overline{\zeta}_2) P_{12}(\zeta_1, \zeta_2) d\zeta_1 d\zeta_2 = \overline{\zeta_1' \zeta_2'} \quad .$$

It is possible to relate covariance to the concept of correlation between two variables: $R_{ij}(r) = \overline{u_i'(0) u_j'(r)}$ is the spatial correlation between velocities u measured in two points separated by a distance r for homogeneous variables; $R_{ij}(\tau) = \overline{u_i'(0) u_j'(\tau)}$ is the temporal correlation between velocities u measured at 2 times separated by

a time distance τ for stationary variables. A strong correlation means a strong simultaneous variability of the two variables in space or time, so that, inside a turbulent flux, R_{ij} is an index of the probabilty that the variables measured at a distance r or at a time distance t belongs to the same eddy.

Writing the original signal as the sum of a mean field and a fluctuation field is called *Reynolds decomposition* if the variable satisfies the following conditions: it must be a stationary or weakly-stationary stochastic variable associated to sampled signals with mean value $\overline{u}$ and zero mean fluctuations $\overline{\sigma}_u^2 = 0$.

Reynolds also prescribes some properties to be satisfied for the mean operator. In particular, the property $\overline{\overline{uv}} = \overline{uv}$ is not satisfied by all kind of means, but only by the ensemble average: $\overline{\zeta} = \frac{1}{N}\sum_{i=2}^{N}\zeta^i(\vec{x},t)$.

This is an operative problem because it is not possible to make measures in an ensemble sense. Thus, a more strict constraint must be imposed: the sampled variable must satisfy the *ergodicity* conditions of *stationarity* (or at least *weakly-stationarity*), *homogeneity* and *isotropy*, to ensure that ensemble averages are equivalent to time averages:

$$\overline{\zeta} = \frac{1}{N}\sum_{i=2}^{N}\zeta^i(\vec{x},t) = \lim_{T\to\infty}\frac{1}{T}\int_0^T \zeta(t)dt \quad .$$

A turbulent flux is said to be: *stationary* when the variance σ_u^2 of the field u remains constant in time; *weakly-stationary* if at least both first moments (i.e. means, fluctuations) and autocorrelations are constant in time, and second moments (i.e. variances and covariances between the components of u) is finite for all times. Periodic signals represents an example of weak-stationarity. In atmospheric boundary layer, the turbulent scales are typically $\Delta t = 15$ mins $\div$ 1 hrs, i.e. the range of time in which turbulent frequencies results well isolated from any other scale's influence (1.5). Turbulent meteorological signals sampled at turbulent scales often can reach, after a transient phase, a stationary state: in this case the meteorological signal is said to be in a *fully developed turbulence* state.

Homogeneity means that variables are spatially uniform, so that statistical properties are invariant under arbitrary translations of the coordinate axes. This is in general true for fully developed turbulence.

Isotropy means the absence of preferential directions, i.e. the statistical properties are invariant for rotations and reflections of the coordinate axes. As will be shown in Section 1.6.3, the isotropy is part of the Kolmogorov hypotesis for the eddies sub-scales, while, for the bigger scales, anisotropy arise in dynamic instabilities and vertically in thermal instabilities, so eddies can be considered isotropic only far from boundary walls and in thermally neutral conditions.

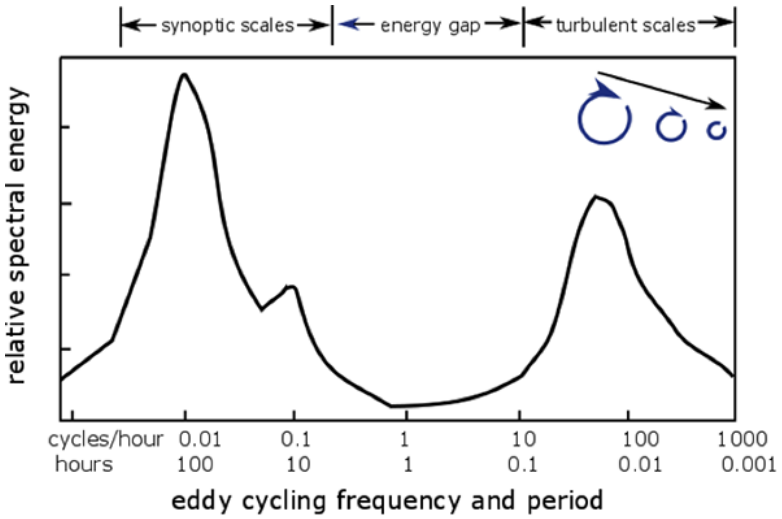

Figure 1.5: Spectral energy of the atmospheric phoenomena in the range of synoptic and turbulent scale.

Temporal and spatial scales that characterize the turbulent eddies can be evaluated from the correlations: an eddy's characteristics length scale on $\hat{k}$ direction is

$$L_{ij}^{k} = \frac{1}{\overline{u_i' u_j'}} \int_0^\infty R_{ij}(r) dr_k \quad ;$$

an eddy's characteristics time scale is

$$T_{ij} = \frac{1}{\overline{u_i' u_j'}} \int_0^\infty R_{ij}(\tau) d\tau \quad .$$

Since kinetic energy of the mean flux is $\frac{1}{2}(\overline{u}^2 + \overline{v}^2 + \overline{w}^2)$, the kinetic energy of the turbulent flux is

$$\frac{1}{2}(\sigma_u^2 + \sigma_v^2 + \sigma_w^2) \quad . \tag{1.44}$$

This means that the kinetic turbulent energy is directly related to the correlation coefficients R_{ii}. Indeed, since turbulent fluxes can be viewed as a superposition of infinite eddy frequencies, the energy spectrum can be defined as the Fourier transform of the correlation coefficient in spatial (wavenumber k) domain:

$$E(k) = \frac{1}{(2\pi)^3} \int_0^\infty R_{ij}(r) e^{-ik \cdot r} dr_1 dr_2 dr_3$$

and in temporal (frequency $\hat{\omega}$) domain:

$$E(\hat{\omega}) = \frac{2}{\pi} \int_0^\infty R(\tau) cos(\hat{\omega}\tau) d\tau \quad .$$

The relation between $E(k)$ and $R_{ij}(r)$ will be further discussed in the next Section.

1.6.3 Kolmogorov's Theory

From the definition of Reynolds number, very high values of Re ($Re \gg 1$) mean that inertial forces dominate over viscosity and thus the latter can be neglected. The range of scales in which this is valid is called *inertial subrange*. As it will be justified in Section 1.6.5, dissipation appears inside the turbulent kinetic energy's conservation equation as a $[\frac{u^3}{l}]$ quantity, where u and l are intended as eddy's characteristic scales. The inferior limit of this range must be that scale η at which $Re = \frac{u_\eta \eta}{\nu} = 1$. From this, it is possible to obtain (see Kundu and Cohen for a detailed demonstration) the scales of the smallest inertial eddy: $\eta = \nu^{3/4}\epsilon^{-1/4}$, $u_\eta = (\nu\epsilon)^{1/4}$ and $\tau_\eta = \frac{\nu}{\epsilon}^{1/2}$.

In Section 1.6.2 it has been said that R_{ij} is the Fourier antitransform of the energy spectrum, such that

$$R_{ii}(0) = \overline{u}'^2 = \int_0^\infty E(k)dk \quad .$$

Thus $E(k)dk = u_l^2$ is the energy density in the range $[k, k+dk]$, where eddies have velocities scaled as u_l, defined in the length range $[l, l+dl]$. From this, it can be showed that $E(k) \sim \epsilon^{2/3}k^{-5/3}$ (Figure 1.6).

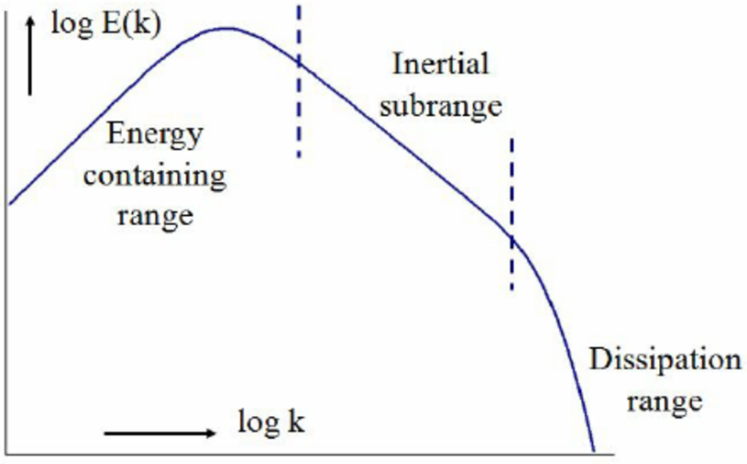

Figure 1.6: Kolmogorov spectral energy ranges in logaritmic scale.

Ratio between the largest eddy's scales l_0, u_0, τ_0 and the smallest eddy's scales η, u_η, τ_η gives the amplitude of the scale's ranges in terms of Reynolds number:

$$\frac{l_0}{\eta} = Re^{3/4} \quad , \frac{u_0}{u_\eta} = Re^{1/4} \quad , \frac{\tau_0}{\tau_\eta} = Re^{1/2} \quad .$$

Finally, the largest length scale l_0 can be found by knowing that $u(l_0) = u_0 \approx \sigma_u =$

$\sqrt{\frac{2}{3}k_t} \sim U$, from which $\epsilon \sim \frac{u^3}{l_0} \sim \frac{k_t^{3/2}}{l_0}$, thus

$$l_0 \sim \frac{k_t^{3/2}}{\epsilon} \quad .$$

Turbulence ranges are depicted in Figure 1.7. Kolmogorov made some hypothesis regarding the energy cascade structure and the associated eddies properties that formalize the aforementioned statements:

- there is a length scale $l_{EI} \sim \frac{l_0}{6}$, that separates energy production scales from transfer (inertial) scales. Every eddy in the cascade process that has $l < l_{EI}$, has lost all directional biases of the mean flow. Thus, below l_{EI}, total isotropy can be assumed;
- there is a length scale $l_{DI} \sim 60\eta$, that separates transfer (inertial) scales from dissipative scales, for which every eddy in the cascade process that has $l < l_{DI}$ has lost any information about mean flux and boundary conditions, thus universality can be assumed. Also such scales depend both on ϵ and ν;
- there are intermediate scales $l_{DI} < l < l_{EI}$ for which Re is still large, such that they depend only on ϵ.

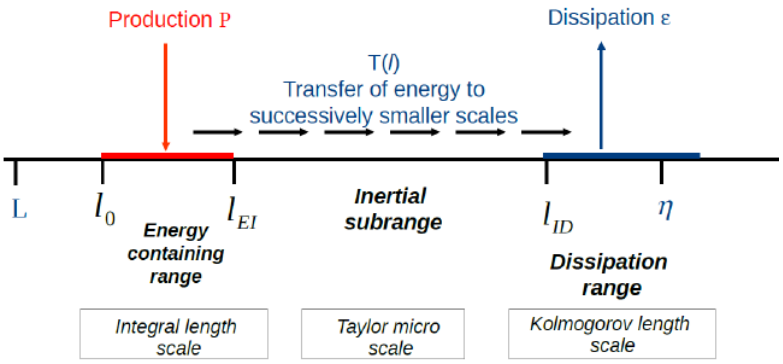

Figure 1.7: Different length scales and ranges in turbulence energy cascade. Taken by Saeedipour et al., 2014

The information gathered tells us that the energy spectrum has a trend $\propto k^{-5/3}$ in an interval between l_0 and η, which is known as inertial subrange, that is univocally defined by the Reynolds number. The complete form of $E(k)$, that also contains the ranges outside the inertial subrange, is a function of the *integral* length scale L of the mean flow (inside the energy production range) and the Kolmogorov scale η (inside the dissipative range):

$$E(k) = C f_L f_\eta \epsilon^{2/3} k^{-5/3} \quad .$$

To underline the role of production range and dissipative range, the following observations can be made:

- the integral $\int_{l_{EI}}^{6l_0} E(k)dk$ gives 90% of the total turbulent kinetic energy, meaning that those scales produce the largest amount of energy in the cascade process;
- the integral $\int_{8\eta}^{60\eta} D(k)dk$, where $D(k)dk$ is the dissipation energy density in $k, k+dk$, gives 90% of the total dissipation (Figure 1.8), meaning that those scales make almost all the dissipation in the cascade process.

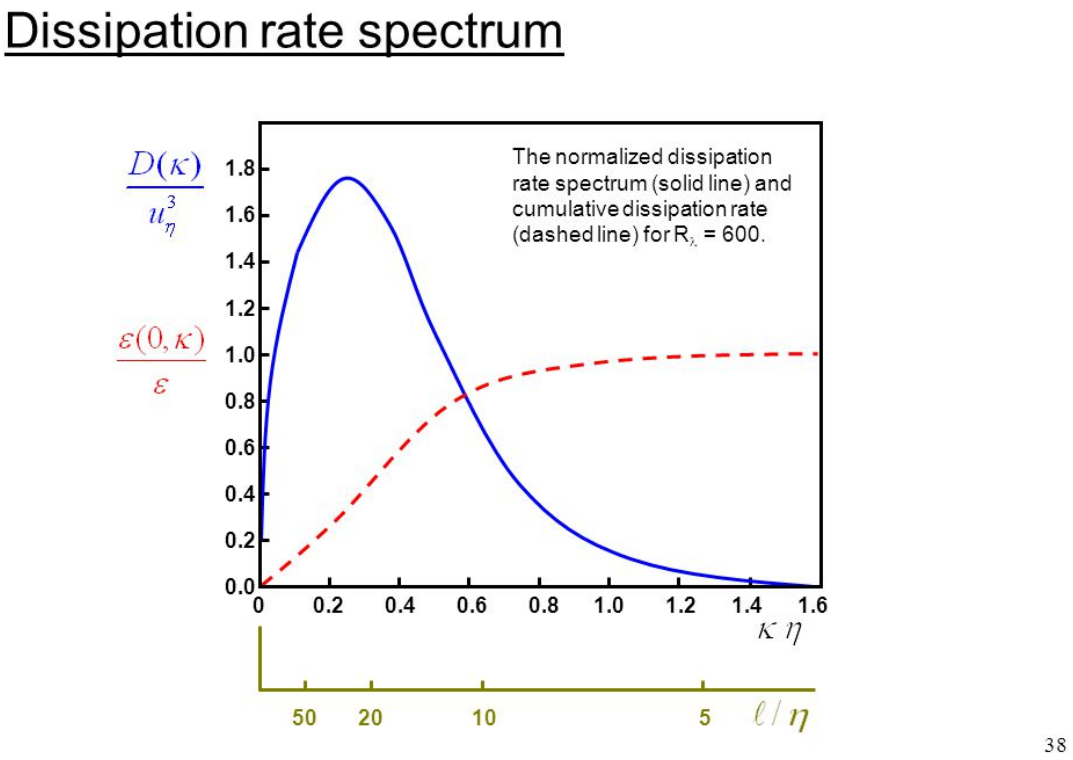

Figure 1.8: Dissipation energy spectrum and cumulative function.

Because the generic eddy's lifetime can be written as $\tau = \frac{k_t}{\epsilon}$, this means that an eddy spends 90% of his lifespan into the production range, then breaks up into the inertial range and becomes dissipated after just $\frac{\tau}{10}$, the cascade timescale.

1.6.4 Reynolds averaged equations

Assuming that turbulent fluctuations are stochastic deviations from the mean value and that they have zero mean, the equations can be adapted to the turbulence presence.

Hereafter the Reynolds decomposition will be used, i.e. every field will be expressed as $f(x,y,z,t) = \overline{f} + f'(x,y,z,t)$, where the mean is an ensemble average. The momentum equation becomes:

$$\partial_t(\overline{u}_i + u'_i) + (\overline{u}_j + u'_j)\partial_j(\overline{u}_i + u'_i) = -\frac{1}{\rho_0}\partial_i(\overline{p} + p') + \nu\partial_j^2(\overline{u}_i + u') + \beta(\overline{\Delta T} + T')g\delta_{i3} \quad . \tag{1.45}$$

Knowing that fluctuations have zero mean and that $\overline{\overline{u}} = \overline{u}$, averaging the above equation gives the *Reynolds Averaged Navier-Stokes* equation (*RANS*):

$$\partial_t\overline{u}_i + \overline{u}_j\partial_j\overline{u}_i = -\frac{1}{\rho_0}\partial_i\overline{p} + \nu\partial_j^2\overline{u}_i - u'_j\partial_j u'_i + \beta\overline{\Delta T}g\delta_{i3} \quad . \tag{1.46}$$

The new term can be reformulated knowing that the fluctuation's continuity equation $\partial_i u'_i = 0$ is valid. Thanks to this, it is possible to write $u'_j\partial_j u'_i = u'_j\partial_j u'_i + u'_i\partial_j u'_j = \partial_j u'_i u'_j$. Because the average of the product of fluctuations is generally different from zero, averaging this term gives a value that cannot be assumed as zero. This term remains into the Reynolds equation and has the dimensions of the stress. As such, it is called *Reynolds stress*:

$$\tau^r_{ij} = -\rho_0\overline{u'_i u'_j} \quad . \tag{1.47}$$

The components of the Reynolds stress τ^r correspond to the ones of the correlation matrix R defined in Section 1.6.2 multiplied by $-\rho_0$, so its trace is two times the turbulent kinetic energy (Equation (1.44)), while its deviatoric part contains the momentum fluxes (that will be better described in Section 1.7). After the substitution, the Equation (1.46) becomes:

$$\partial_t\overline{u}_i + \overline{u}_j\partial_j\overline{u}_i = -\frac{1}{\rho_0}\partial_i\overline{p} + \frac{1}{\rho_0}\partial_j(\mu\partial\overline{u}_i + \tau^r_{ij}) + \beta\overline{\Delta T}g\delta_{i3} \quad . \tag{1.48}$$

An analogous reasoning for the temperature leads to a Reynolds averaged temperature equation:

$$\partial_t T + \overline{u}_j\partial_j T = \frac{1}{\rho_0}\partial_j\left(\frac{k}{c_v}\partial_j T - \rho_0\overline{u'_j T'}\right) \quad . \tag{1.49}$$

The system composed by Equations (1.48) and (1.6.4) must be closed in order to be solved. The closure issue will be discussed in more detail in Section 1.7.

1.6.5 The Turbulent Kinetic Energy

Defining $k_m = \frac{\overline{u_i u_i}}{2}$ the mean kinetic energy (MKE), its conservation equation is derived by multiplying Equation (1.48) by $\overline{u}_i$ and rearranging:

$$\partial_t k_m + \overline{u}_j \partial_j k_m = \frac{1}{\rho_0}\partial_j(\overline{u}_i \tau^r_{ij} - \overline{u_i p} - \mu \partial_j k_m) - \nu \partial_j \overline{u}_i \partial_j \overline{u}_i - \tau^r_{ij}\partial_j \overline{u}_i + \beta \overline{\Delta T}\,\overline{u}_i g \delta_{i3} \quad . \tag{1.50}$$

It is worth to point out that even if the Coriolis force were considered into the momentum equation, it would not have added any contribute inside the MKE conservation, because this force does not perform work.

Of the four terms on the right-hand side, the first one is the *transport term* and, integrated over a volume, gives a flux of energy that transport energy inside or outside that volume. The second one is the *viscous dissipation* term and represents a loss of energy caused by viscous forces. The third term is the *shear production*, that implies a loss of energy caused by turbulent fluxes (as better explained later in this Section). The fourth term is the buoyancy, which can be an energy sink or production term depending on the sign of $\overline{u}_i \delta_{i3}$, but in any case represents an energy conversion between kinetic and potential energy.

The turbulent kinetic energy (TKE) equation can be derived by subtracting the Reynolds equation (1.48) to the Navier-Stokes Reynolds-decomposed equation (1.46). This leads to an equation for the fluctuation u'_i:

$$\partial_t u'_i + \overline{u}_j \partial_j u'_i = -\frac{1}{\rho_0}\partial_i p' + \nu \partial^2_j u'_i + \partial_j(u'_i u'_j - \overline{u'_i u'_j}) + \overline{u'_j \partial_j u'_i} + \beta T' g \delta_{i3} \quad . \tag{1.51}$$

From this, an equation for the turbulent kinetic energy (TKE) $k_t = \frac{\overline{u'_i u'_i}}{2}$ is obtained by multiplying the above equation for u'_i and by averaging:

$$\partial_t k_t + \overline{u}_j \partial_j k_t = -\frac{1}{\rho_0}\partial_j(\overline{u'_j k'_t} + \overline{u'_i p'} - \mu \partial_j k_t) + \tau^r_{ij}\partial_j \overline{u}_i + \beta \overline{T' u'_i} g \delta_{i3} - \nu \overline{\partial_j u'_i \partial_j u'_i} \quad . \tag{1.52}$$

As for the MKE equation, it is possible to distinguish the same four kind of terms. The *transport* term generally includes the coupling between pressure and velocity fluctuations $\overline{u'_i p'}$, that arise in presence of turbulence, and the turbulent transport of TKE $\overline{u'_j k'}$.

The term $\tau^r_{ij}\partial_j \overline{u}_i$ is the *shear* term and represents a mechanism that transfers energy between the mean flow and the turbulent flow, since it appears with an opposite sign in both MKE and TKE equations. As will be seen in Section 1.7, adopting an eddy-viscosity model which assumes a relation between fluxes and gradient of the kind $\overline{u'_i u'_j} = -\nu_t(\partial_j \overline{u}_i + \partial_i \overline{u}_j)$, the shear term will always be positive, and this implies that, in such case, the energy transfer is always from the mean to

the turbulent flow.

The *buoyancy* term $\beta\overline{T'u_i'}g\delta_{i3}$ can be a production or a sink term for the TKE, depending on the sign of the sensible heat flux $\overline{T'u_i'}$.

The *dissipation* term is $\nu\overline{\partial_j u_i' \partial_j u_i'}$ and is always positive. This term is usually labeled as ϵ and its dimensions are $[\epsilon] = [\frac{m^2}{s}][\frac{u}{l}][\frac{u}{l}] = [\frac{m^2}{s^3}]$, which are consistent with the Kolmogorov analysis undertook in Section 1.6.3.

1.6.6 Turbulent fluxes and thermal stability

Consider now a simpler situation of stationariety and horizontal homogeneity (i.e. $u_3 = 0$), neglecting molecular viscosity ($\nu\nabla^2 u_i$). Those are common assumptions made over an horizontal surface and will be useful for our boundary layer treatment. In order to lighten the notation, it will be substituted the velocity tensorial notation u_i for $i = 1, 2, 3$ with the more common meteorological notation (u, v, w), with directions $(\hat{x}, \hat{y}, \hat{z})$ (being $\hat{z}$ the gravity direction). The TKE-equation will be:

$$-\frac{1}{\rho_0} d_z(\overline{w'k'} + \overline{wp}) - (\overline{u'w'} d_z\overline{u} + \overline{v'w'} d_z\overline{v}) + \beta\overline{T'w'}g - \epsilon \sim 0 \quad . \tag{1.53}$$

Richardson flux number is defined as the ratio between the two production/sink terms of turbulent kinetic energy

$$Ri_f = \frac{\beta\overline{T'w'}g}{\overline{u'w'} d_z\overline{u} + \overline{v'w'} d_z\overline{v}} \tag{1.54}$$

and it can be utilized to rewrite the above equation:

$$-d_z(\mathcal{T}) - (\overline{u'w'} d_z\overline{u} + \overline{v'w'} d_z\overline{v})(1 - Ri_f) - \epsilon \sim 0 \quad , \tag{1.55}$$

where $\mathcal{T}$ is the generic transport term that includes the pressure coupling and the TKE turbulent transport.

From his definition, Ri_f is able to give information about the thermal stability of the fluid: $Ri_f < 0$ implies a positive heat flux and thus a thermally instable stratification, while $Ri_f > 0$ implies a negative heat flux and thus a thermally stable stratification. Ri_f has great negative values when heat flux is strong and/or shear production is weak (*free convection*). $Ri_f = 0$ means absence of heat flux and thus energy completely generated by mechanical shear production (*forced convection*). If $Ri_f > 1$ the second term of the momentum equation (1.55) changes sign because of the strong positive heat flux that dominates over the mechanical shear. This situation completely suppress turbulence. The critical value at which turbulence begins to arise from the balance between buoyancy and shear, in the

form of Kelvin-Helmholtz instabilities, is $Ri_{f_c} \sim \frac{1}{4}$.

1.7 The closure issue

1.7.1 A physical interpretation of turbulence

The principal problem with turbulence equations is clear when looking at the Reynolds equations (1.48): the addition of fluctuations as new unknown variables leads to new equations to be solved.

There are two ways to proceed:

- the first one is using the $\overline{u_i' u_j' u_k'}$ equation to solve for $\overline{u_i' u_j'}$, but then would be needed a $\overline{u_i' u_j' u_k' u_h'}$ equation to solve for $\overline{u_i' u_j' u_k'}$, and so on;
- the second one is to approach the problem according to the interested quantity: if $\overline{u_i' u_j'}$ is the term of interest, the extra term $\overline{u_i' u_j' u_k'}$ will be parametrized in terms of $\overline{u_i' u_j'}$ itself, while if $\overline{u_i}$ is the term of interest, the extra term $\overline{u_i' u_j'}$ will be parametrized in terms of the $\overline{u_i}$ field itself.

A physical justification for taking the second approach was given by Prandtl's mixing length theory reasoning on diffusion: he pointed out that considering the mean profile of a quantity $c(z)$ of the kind $d_z \overline{c} < 0$ (see Figure 1.9), any vertical motion's fluctuation $w' > 0$ would take a parcel of fluid on a height characterized by a fluid with smaller c.

As a consequence, the parcel will transport upward the property c as a fluctuation $c' > 0$. In other words, the sign of $\rho_0 \overline{w'c'}$ will be positive, meaning a positive flux of c in the z direction. The same sign would be obtained with $w' < 0$, causing a fluctuation $c' < 0$.

For a positive $d_z \overline{c}$ profile, a $w' > 0$ fluctuation would lead to a $c' < 0$ fluctuation, while a $w' < 0$ would lead to a $c' > 0$ fluctuation. So, in both cases, it results in a negative products $\rho_0 u_i' u_j'$, thus a negative flux of c.

From the above discussion it is possible to understand that the justification of relating $\overline{u_i' u_j'}$ to the mean field is the turbulent analogous of the Fick's law of diffusion $J = -D d_x \phi$ that relates a flux J of a property ϕ with his gradient $d_x \phi$ through some diffusivity parameter D.

The most common of these diffusive models is the Eddy Viscosity Model, in which the eddy viscosity ν_t (or alternatively the dynamic viscosity μ_t) relates the generic shear Reynolds stress $u_i' u_j'$ to the mean deformation velocity: $\overline{u_i' u_j'} = -\nu_t(\partial_j \overline{u}_i + \partial_i \overline{u}_j)$, but in order for the sum over the normal stresses $\overline{u_i' u_i'}$ to be equal

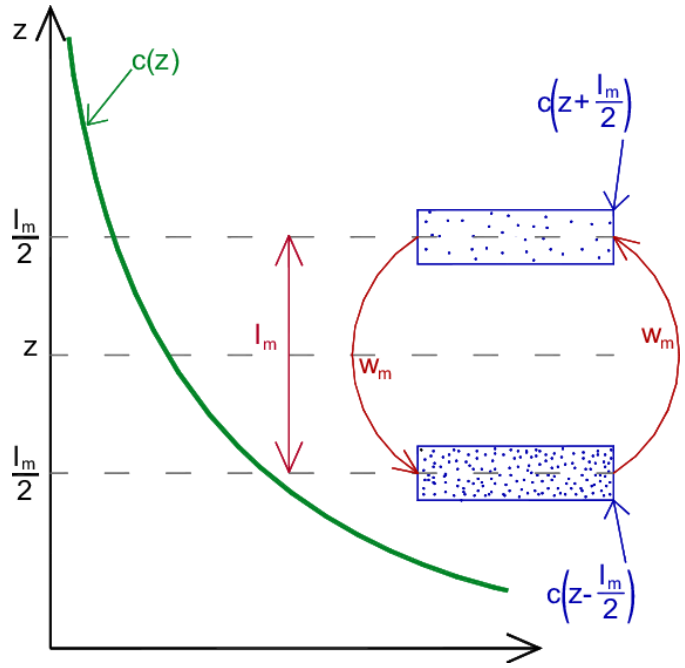

Figure 1.9: Sketch of eddy-viscosity models interpretation (Nielsen and Teakle,Jan. 2011).

to $2k_t$, one can write $\tau_{ij}^r = -\rho\overline{u_i' u_j'} = -\frac{2}{3}\rho k_t \delta_{ij} + \mu_t(\partial_j \overline{u}_i + \partial_i \overline{u}_j)$. Reynolds equation can be reformulated in a more compact manner defining the *corrected pressure* $\overline{p}_* = \overline{p} + \frac{2}{3}\rho k_t$:

$$\rho_0 d_t \overline{u}_i = -\partial_i \overline{p}_* + \partial_j((\mu + \mu_t)\partial_j \overline{u}_i + \partial_i \overline{u}_j) + \beta\overline{\Delta T} g \delta_{i3} \quad , \tag{1.56}$$

which is a closed equation in terms of u_i, for a given $\overline{p}_*$.

1.8 Planetary Boundary Layer

1.8.1 Structure and daily evolution

As a solid boundary is approached, velocities goes to zero, becoming less and less relevant compared to viscosity, and Reynolds number tend to zero. The proximity of a surface thus generates a layer in which viscosity is no more neglectable, and a sub-layer in which the latter is dominant upon any other force acting on the fluid. Therefore, the velocity of the fluid adapts to the presence of a solid surface following a profile that tends to zero exactly at surface level (see Figure 1.10. This can generally be called a *mechanical boundary layer*.

A *thermal boundary layer* is a region near a physical surface in which the fluid temperature is directly influenced by the heat fluxes that it receives from the surface. The two boundary layers do not coincide, and have in general different thicknesses, but they depends on each other. This dependence is generally described by the

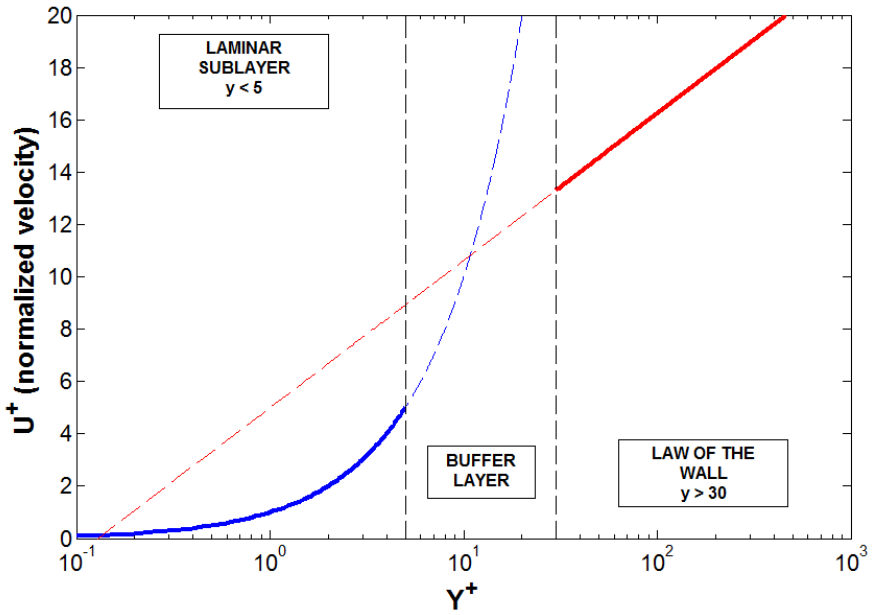

Figure 1.10: The different regimes of viscosity influence over normalized velocity.

Prandtl number: the ratio between momentum and thermal diffusivities. That is, $Pr \ll 1$ means that heat diffuses much quicker than velocity does, and thermal conduction dominates the heat transfers, while $Pr \gg 1$ shift the dominant role to the momentum diffusion, and heat transfer is strongly convective. This describes also what happens over the Earth's surface, where a boundary layer generates, with characteristics that depends on atmospheric stability, surface heat fluxes, friction, topography and any source or sink of mechanical and thermal nature that involves the surface. The *planetary boundary layer* (PBL) extends typically on the first 1-2km of the troposphere[1] (Figure 1.11), and his thickness is extremely sensible to the diurnal cycle (Figures 1.12, 1.13). During the day it appears as a strong *convective boundary layer* (CBL), with a thermally unstable surface viscous layer of about 200 m, upon which resides a thick turbulent mixed layer of $\sim$ 1 km, followed by a strong stable inversion layer of $\sim$ 200 m (the *entrainment layer* EL), and then the free geostrophic atmosphere of the large scales dynamic. As the sun goes down, heat fluxes decrease and a *stable boundary layer* begins to arise from the surface (the nocturnal SBL), suppressing turbulence and leaving the mixed layer to the inertial acceleration (*neutral residual layer*), while the inversion layer loses his entrainment role and becomes a stable *capping layer*. When the diurnal cycle starts over, entrainment begins from the surface and feeds a new convective boundary layer.

[1]The troposhere is the portion of the atmosphere that covers the first 10-15 km from the surface, characterized by an overall decreasing temperature profile (except near the surface where it is affected by the boundary layer's influence)

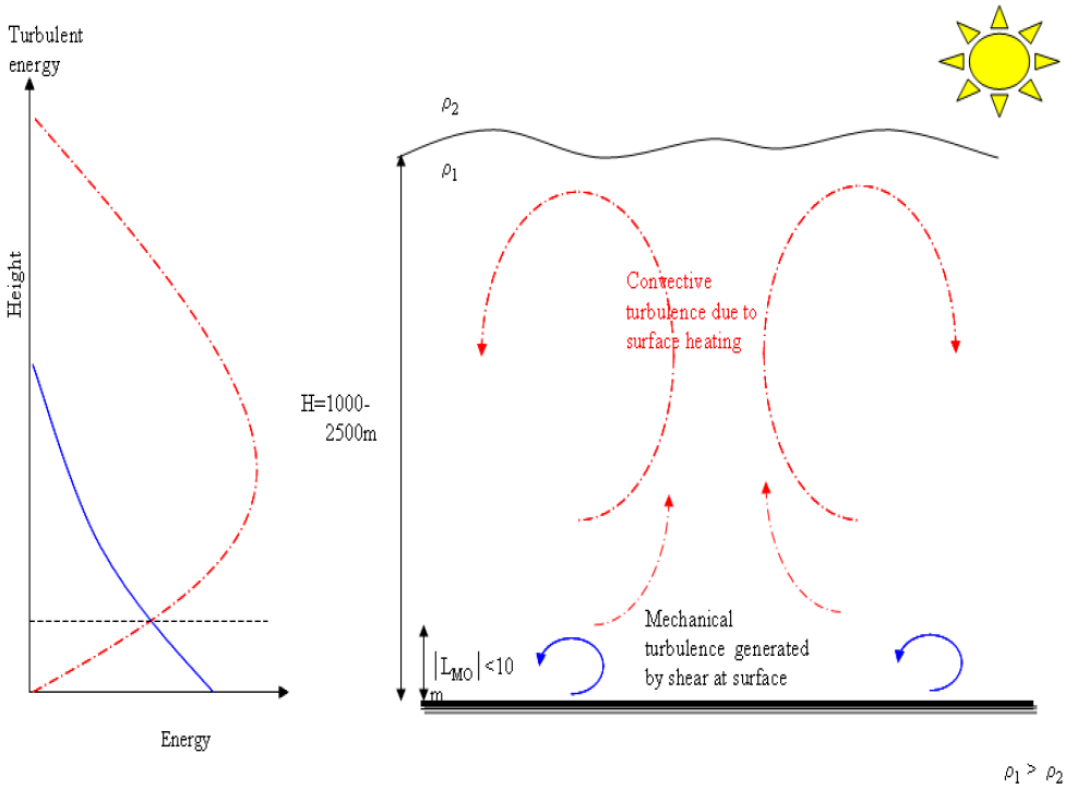

Figure 1.11: Turbulent kinetic energy in a planetary convective boundary layer.

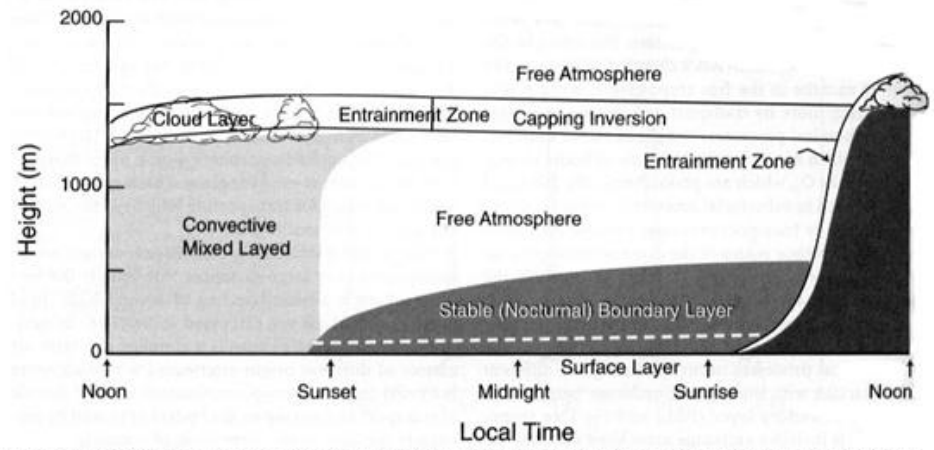

Figure 2.7. Typical diurnal evolution of the planetary boundary layer under a high pressure system. (adapted from Stull, Boundary Layer Meteorology, Kluwer, 1988)

Figure 1.12: Diurnal cycle of the planetary boundary layer (Tampieri, Sept. 2013).

An example of *neutral boundary layer* is the atmosphere above oceans, where particular conditions such as the adaptable free surface and the constant humidity, make the diurnal cycle less important and heat fluxes do not significantly influences the BL structure.

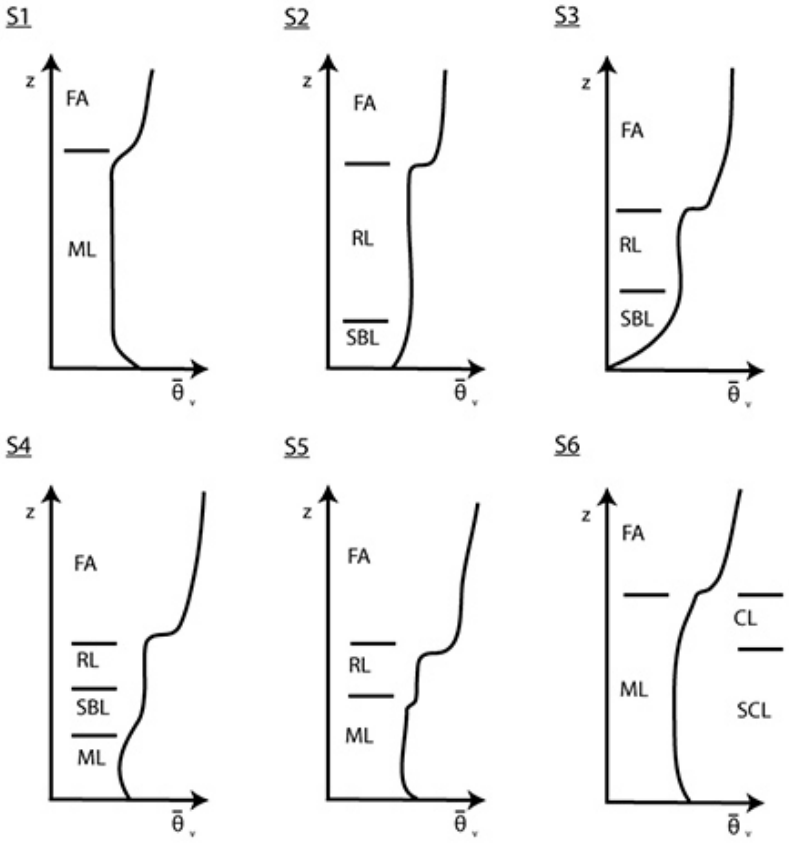

Figure 1.13: Profiles of the diurnal cycle of the planetary boundary layer (Tampieri,Sept. 2013).

1.8.2 Vertical profiles and scales inside the planetary boundary layer

Horizontal shear stress over the surface can be modeled as $\tau = \rho u_*^2$, where u_* is the *friction velocity* $u_*^2 = \sqrt{(\overline{u'w'} + \overline{v'w'})}$. This parameter can be used to scale the mechanical forcing inside the surface layer (where turbulent fluxes are nearly constant), together with the mixing length l_m, defined as the length that a particle need to travel along z in order to lose it's identity and completely mix into the environment.

The two scales define the horizontal shear as $u* = l_m d_z \overline{u}$. Velocity profile depends on environmental stability:

- Neutral planetary boundary layer: temperature has no influence on the dynamics, Richardson number is small, l_m depends only on the distance from the ground $l_m = \kappa z$ with κ von Karman constant, then $d_z\overline{u} = \frac{u*}{\kappa z}$ implies $\overline{u} = \frac{u*}{\kappa} ln(\frac{z}{z_0})$. The last relation takes the name of *law of the wall*.

- Non-neutral planetary boundary layer: as the buoyancy increases, turbulence increases and diffusivity changes, i.e. vorticity size changes. The usual approach for the surface layer is to modify the mixing length definition as $l_m = \frac{\kappa z}{\Phi_m}$ leaving to the adimensional Φ_m the stability influence, as a function of $\zeta = \frac{z}{L}$ the so called *Monin-Obukhov parameter*. This parameter is linked to the Richardson number, and the $L = -\frac{u*^3}{\kappa\beta(\overline{w't'})_0}$ height can be interpreted as that height at which buoyancy and shear production are of the same order. This implies that the buoyancy dominant region and the shear dominant region are distinguishable with the conditions $z \gg L$ and $z \ll L$. Furthermore, $\frac{z}{L} > 0$ is the condition for stability, $\frac{z}{L} < 0$ is the condition for instability, while $\frac{z}{L} = 0$ ($L = \pm\infty$) is the neutral condition (Figure 1.14). Temperature inside the surface layer of a non-neutral boundary layer can be parameterized in the same way as $d_z\overline{T} = \frac{T*}{\kappa z}\Phi_h(\frac{z}{L})$ that implies again a logarithmic profile.

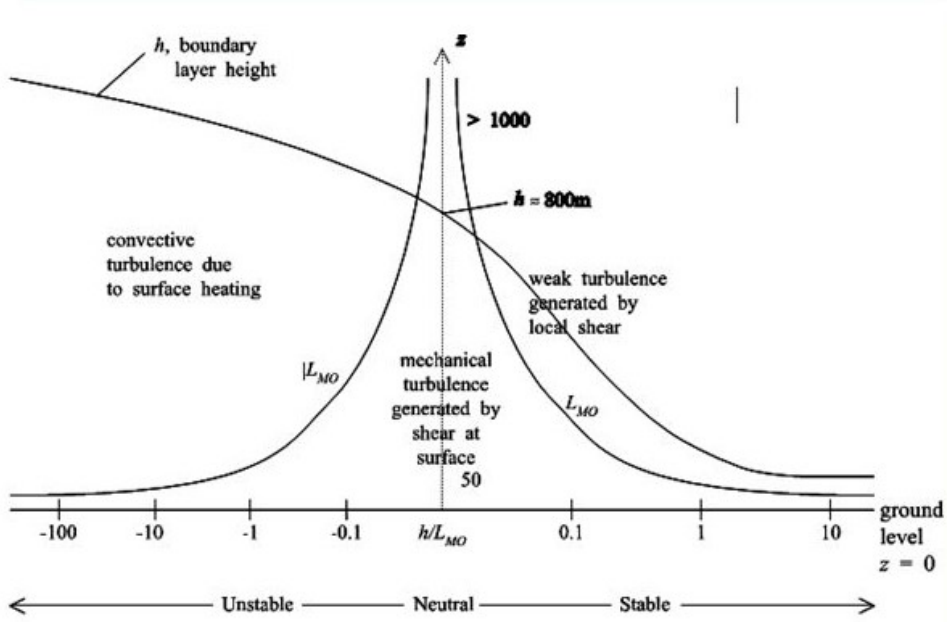

Figure 1.14: Monin-Obukhov length and boundary layer height for different stratification's conditions (Tampieri,Sept. 2013).

If conditions are convectively non-neutral, above the surface layer must be found new characteristic scales, because turbulence changes them. Knowing that updraft comes from buoyancy, a scaling for the vertical velocity can be extrapolated directly from the heat flux: $w_* = (\beta\overline{(w'T')}_0 z)^{1/3}$, so that where buoyancy becomes comparable with shear ($z \sim L$), horizontal velocity scale and temperature scale can be redefined as $u_{**} = \frac{u_*^2}{w_*}$ and $T_{**} = \frac{\overline{T'w'}}{w_*}$. As buoyancy becomes the only relevant force ($z >> L$), convective vertical velocity becomes the only significant velocity scale, so that gradients are parameterized directly as $d_z\overline{u} \sim \frac{w_*}{z}$ and $d_z\overline{T} \sim \frac{T_{**}}{z}$.

If conditions are neutral, above the surface layer one gets a velocity profiles that respond to a classical Ekman-type dynamic for which

$$\epsilon_{ijk} f(\overline{u}_j - u_{gj}) = d_z(\overline{u'w'}) \quad , \tag{1.57}$$

that has the Ekman spiral as a velocity solution and $u_j = u_{gj}$ at the top of the Ekman layer.

As diurnal cycle transits from a convective boundary layer to a nocturnal stable boundary layer, leaving a neutral *residual layer* above the *surface layer*, turbulence inside this layer disappears and leaves the fluid free of reaching the geostrophic velocity. This transient adaptation gives velocity field's oscillations, so that $\overline{u}$ can assume values that oscillate around $\overline{u}_g$. These oscillations are the origin of the so called *low level jets* (LLJ).

From the definition of the vertical velocity scale $w_* = (q_0 z)^{1/3}$, another reformulation of the Reynolds number is possible: $Re = \frac{UL}{\nu} = \frac{(q_0 H)^{1/3} H}{\nu}$.

1.8.3 Turbulent kinetic energy in a boundary layer

As already seen in equation 1.52, TKE conservation is regulated by four terms:

- the *transport* term:

$$-\frac{1}{\rho_0}\partial_j(\overline{u'_j k'} + \overline{u'_i p'} - \mu \partial_j k_t) \quad ,$$

- the *mechanical production* term:

$$\tau^r_{ij}\partial_j \overline{u}_i \quad ,$$

- the *buoyancy* term:

$$\beta \overline{T' u'_i} g \delta_{i3} \quad ,$$

- the *dissipation*:

$$-\nu \overline{\partial_j u'_i \partial_j u'_i} \quad .$$

Thus the TKE equation is:

$$\text{TKE} = \text{TRANS} + \text{PROD} + \text{BUOY} + \text{DISS} \quad . \tag{1.58}$$

In a boundary layer perspective, this four terms have different relevance as a function of the height above the solid surface. As a general consequence of the fact that velocities go quickly to zero near the surface, mechanical production is much

greater than other terms in that region. Also dissipation is much stronger near the surface where viscosity becomes a relevant factor. Depending on the stability of the atmosphere and the heat flux value assumed at the surface, thermal contribute of buoyancy can be more or less relevant inside the thermal layer (Figure 1.15). Investigation of the behaviour of each term can give us useful insight about how

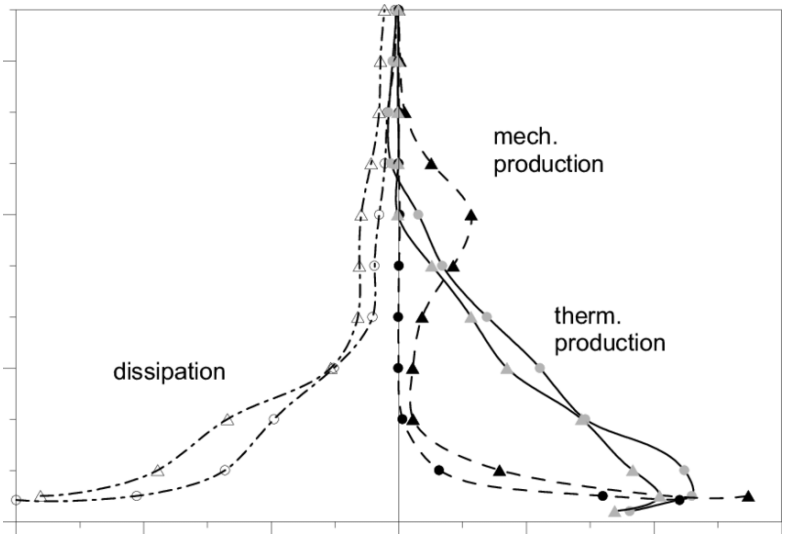

Figure 1.15: Profiling of each of the turbulent kinetic energy terms as a function of the distance from the surface (Tampieri,Sept. 2013).

strong the energy fluxes are in a boundary layer and on which directions they propagate inside the fluid.

Chapter 2

Large-Eddy Simulations

In section 1.6.4 it has been shown that Reynolds-Averaged Navier-Stokes (RANS) equations introduce a turbulent stress term that must be modelled in order to close the system. In order to reproduce with accuracy the physics of the real problems, the turbulent model implemented must be able to represent every scale of the turbulence. It is possible to implement a general model that represents the smallest scales, for which universal assumptions can be made, but it is not possible to do the same for the largest scales, that are sensible to the boundary conditions and have to be specifically modelled from case-to-case.

In section 1.6.3 was showed that large scales set the dissipation for all the other scales and contain the largest portion of turbulent energy. Thus, implementing a general model which is accurate only for the small scales, is an excessive approximation for a precise analysis of the problem. In order to solve this, the model used should be adapted each time depending on the problem under consideration. An alternative to this is the Direct Numerical Simulation (DNS) method, the most accurate one, which computes the whole range of spatial and temporal scales of the turbulence without modeling assumption, solving the equation (1.14) instead of (1.48). However, DNS requires the highest computational cost.

In order for a simulation to be accurate in relation to the problem analyzed, it must have a domain size much larger than the largest eddie's scale L and a mesh cell width of the order of the smallest scale η (Piomelli, Jan. 2018). If so, the number of points on a 3d grid on which one would compute Navier-Stokes equations

would be proportional to $N_x N_y N_z \propto \frac{L^3}{\eta^3}$, that from Piomelli's scale analysis results in $Re^{9/4}$ points.

The cost of a calculation can be estimated considering that all the grid points $N_x N_y N_z$ must be computed for the total number of time steps. Each time step limited by the need of resolving the life-time of the smallest eddy and is assumed to satisfy the Courant-Friedrichs-Lewy stability criterion (in our case $\Delta t \Delta x \leq 1$). this criterion is a necessary constraint for the convergence of our partial differential equation's numerical solution, and requires a temporal step that is at most $\Delta t \sim \frac{1}{\Delta x}$. This condition implies that, assuming the simulation time to be at least equal to the integral time scale T, the number of time steps is $\frac{T}{\Delta t} = (N_x N_y N_z)^{1/3}$, i.e. the total cost of the simulation is $(N_x N_y N_z)^{4/3} = Re^3$.

An alternative that is more expensive but more precise than RANS, and less expensive but less precise than DNS, are the Large Eddies Simulations (LES). The LES approach consists in modelling (as in the case of RANS) the smallest scales, that are suitable to be modelled, and computing (as in the case of DNS) the largest scales, that cannot be universally modelled. In doing this, the Reynolds number that a simulation can computationally afford drastically lowers (Chapman, 1979 estimates at most $Re^{1.8}$) compared to a DNS so that problems at highest Re can be studied and finer physical phenomena can be observed.

2.1 Filtered equations

The LES methodology of computing only the largest scales is carried out by a filtering operation. This filtering acts as a cutoff that must operate in the inertial subrange (see previous section). Filtering operation is defined such that the filtered variable is:

$$\widehat{f}(x) = \int_D f(x') G(x, x', \widehat{\Delta}) dx' \quad , \tag{2.1}$$

where G is the filter function integral kernel that determines the filtered scales, while $\widehat{\Delta}$ is the filter width, or the size of the smallest filtered eddies, usually taken proportional to the grid cell width h .

If the problem is anisotropic, then h is usually an average of the grid cell width in the x, y, z direction, for example $(h_x h_y h_z)^{1/3}$.

From this definition of $\widehat{\Delta}$, it can be said that the unresolved eddies are essentially those smaller than the grid resolution. The most common types of filter function are:

the sharp Fourier cutoff defined in wave space:

$$\hat{G}(k) = \begin{cases} 1 \text{ if } k \leq \frac{\pi}{\widehat{\Delta}} \\ 0 \text{ otherwise} \end{cases} \quad , \tag{2.2}$$

the Gaussian filter:

$$G(x) = \sqrt{\frac{6}{\widehat{\Delta}^2 \pi}} e^{-\frac{6x^2}{\widehat{\Delta}^2}} \quad , \tag{2.3}$$

the tophat filter defined in real space:

$$G(x) = \begin{cases} \frac{1}{\widehat{\Delta}} \text{ if } |x| \leq \frac{\widehat{\Delta}}{2} \\ 0 \text{ otherwise} \end{cases} \quad . \tag{2.4}$$

Each of them is shown in figure 2.1:

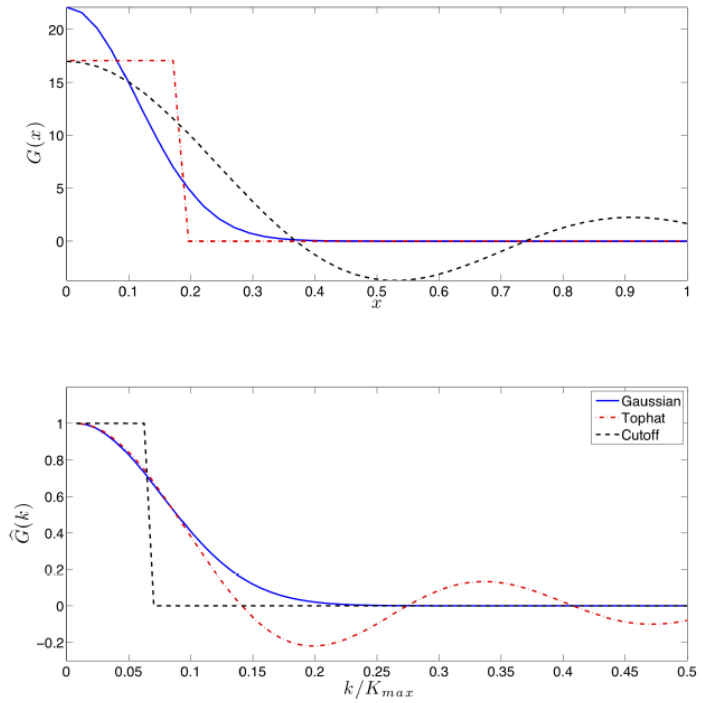

Figure 2.1: Filter functions in both real space and Fourier space (Piomelli, Jan. 2018).

Applying the filtering operation over the Navier-Stokes equations, under incompressible assumption, neglecting here body forces for simplicity, one gets:

$$\partial_t \widehat{u}_i + \partial_j(\widehat{u}_i \widehat{u}_j) = -\frac{1}{\rho_0} \partial_i \widehat{p} + \nu \partial_j(\partial_j \widehat{u}_i + \partial_i \widehat{u}_j) \quad , \tag{2.5}$$

with continuity equation that reads $\partial_i \widehat{u}_i = 0$. The filtered field is defined as

$u'_i = u_i - \widehat{u}_i$. Note that this is different from the Raynolds fluctuation defined in Section 1.6.4, because here contributes of small scales is absent.

The non linear term $\widehat{u_i u_i}$ is decomposed as

$$\widehat{u_i u_i} = (\widehat{u}_i + \widehat{u'_i})(\widehat{u_j} + \widehat{u'_j}) = \widehat{\widehat{u}_i \widehat{u}_i} + \widehat{\widehat{u}_i u'_j} + \widehat{\widehat{u}_j u'_i} + \widehat{u'_i u'_j} \quad . \tag{2.6}$$

It is common to define the Cross-stress tensor:

$$C_{ij} = \widehat{\widehat{u}_i u'_j} + \widehat{\widehat{u}_j u'_i} \quad , \tag{2.7}$$

the Reynolds tensor:

$$R_{ij} = \widehat{u'_i u'_j} \quad , \tag{2.8}$$

and the Leonard tensor:

$$L_{ij} = \widehat{\widehat{u}_i \widehat{u}_i} - \widehat{u}_i \widehat{u}_j \quad . \tag{2.9}$$

The three tensors define the subgrid-scale residual stress (SGS) tensor $\tau_{ij} = L_{ij} + C_{ij} + R_{ij} = \widehat{u_i u_j} - \widehat{u}_i \widehat{u}_j$ (the *triple decomposition*, Garnier, Sagaut, and Adams, 2009), through which the equation 2.6 is expressed as:

$$\partial_t \widehat{u}_i + \partial_j (\widehat{u}_i \widehat{u}_j) = -\frac{1}{\rho_0} \partial_i \widehat{p} + \partial_j \tau_{ij} + \nu \partial_j (\partial_j \widehat{u}_i + \partial_i \widehat{u}_j) \quad . \tag{2.10}$$

In a similar manner the temperature equation becomes:

$$\partial_t \widehat{T} + \partial_j (\widehat{T} \widehat{u}_j) = -\partial_j Q_j + k \partial_j^2 \widehat{T} \quad , \tag{2.11}$$

where $Q_j = \widehat{T u_j} - \widehat{T} \widehat{u}_j$ is the sub-filter scale heat flux .

The equation for the resolved kinetic energy $\widehat{q}_r^2 = (\widehat{u}_i \widehat{u}_i)/2$ is:

$$\begin{aligned} \partial_t \widehat{q}_r^2 = -\partial_j (\widehat{q}_r^2 \widehat{u}_j) + \tau_{ij} \partial_j \widehat{u}_i - \nu \partial_j \widehat{u}_i \partial_j \widehat{u}_i - \partial_i (\widehat{u}_i \widehat{p}) + \partial_i (\nu \partial_i q_r^2) + \\ + \widehat{u}_i \widehat{u}_j \partial_j \widehat{u}_i - \partial_j (\widehat{u}_i \tau_{ij}) \quad , \end{aligned} \tag{2.12}$$

inside which the first term on the right hand side is the advection term, the second is the sub-grid scale dissipation, the third is the viscous dissipation, the fourth is the pression diffusion, the fifth is the viscous diffusion, the sixth is the production and the seventh is the diffusion by interaction with subgrid scales.

Subtracting the large scale equation (2.6) from the unfiltered equation, the

momentum equations for the small scale is obtained:

$$\partial_t \widehat{u_i'} + \partial_j((\widehat{u}_i + u_i')(\widehat{u}_j + u_j') - \widehat{u}_i\widehat{u}_j) = -\frac{1}{\rho_0}\partial_i\widehat{p} + \partial_j\tau_{ij} + \nu(\partial_j^2\widehat{u}_i{}' + \partial_i^2\widehat{u}_j{}') \quad . \tag{2.13}$$

The equation for the filtered sub-grid kinetic energy $\widehat{q}^2_{sgs} = (\widehat{u}_k'\widehat{u}_k')/2$ is obtained by multiplying (2.13) by u_i' and filtering the resulting equation:

$$\begin{aligned}\partial_t q^2_{sgs} = -\partial_j(q^2_{sgs}\widehat{u}_j) - \frac{1}{2}\partial_j(\widehat{u_iu_iu_j} - \widehat{u}_i\widehat{u_iu_j} - \partial_j(\widehat{pu_j} - \widehat{p}\widehat{u}_j) + \\ +2\nu\partial_j q^2_{sgs} + \partial_j(\tau_{ij}\widehat{u}_i) - \nu(\widehat{\partial_j u_i \partial_j u_i}) - \tau_{ij}\partial_j\widehat{u}_i \quad ,\end{aligned} \tag{2.14}$$

in which the first term on the right hand side is the advection term, the second is the turbulent transport, the third is the pression diffusion, the fourth is the viscous diffusion, the fifth is the sub-grid scales diffusion, the sixth is the viscous dissipation and the seventh is the sub-grid dissipation.

As in the MKE and TKE equations (1.50), the energy lost by the resolved scales in equation (2.12) appears as a source term in equation 2.14, i.e. both diffusion and dissipation terms have opposite signs in the two equations.

2.2 Sub-grid models

In general, subgrid-scale models relate the sub-grid stress tensor τ_{ij} to the large-scale strain rate tensor $S_{ij} = \partial_j\widehat{u}_i$ through an eddy viscosity ν_T parametrized in order to avoid an additional equation to solve, using the fact that small scales are more isotropic and homogeneous than large scales:

$$\tau_{ij} - \frac{\delta_{ij}}{3}\tau_{kk} = -2\nu_T\widehat{S}_{ij} \quad . \tag{2.15}$$

Such eddy viscosity is dimensionally the product of a length scale, the filter width, and a velocity scale, usually taken as $\sqrt{q^2_{sgs}}$.
In many cases the transport equation for q^2_{sgs} is simplified by an equilibrium assumption (Piomelli, 2018), considering that small scales have shorter time scales than the large ones, so they adjust more rapidly and all the terms drops out except the production term and the viscous dissipation of sub-grid scale energy: $-\tau_{ij}\widehat{S}_{ij} = \epsilon_v$.

2.2.1 Smagorinsky model

Under the equilibrium assumption, expressing viscous dissipation as $\epsilon_v \simeq \frac{q_{sgs}^3}{\widehat{\Delta}}$ ones obtains:

$$\nu_T = (C_s\widehat{\Delta})^2|\widehat{S}| \quad , \tag{2.16}$$

C_s being a real number, implying that viscous term is always negative. Many estimates in literature has been made about appropriate C_s values, commonly used values are in the range $[0.065, 0.1]$.
In the presence of solid boundaries, length scale are modified using a damping factor (van Driest, 1956), which makes use of y^+:

$$\nu_T = (C_s\widehat{\Delta}(1 - e^{-\frac{y^+}{25}}))^2|\widehat{S}| \quad . \tag{2.17}$$

The above method applied to the momentum equation can also be applied to the thermodynamic equation, leading to a sub-filtered scale thermal diffusivity α_T modeled as the viscous dissipation term through a coefficient C_t:

$$\alpha_T = (C_t\widehat{\Delta})^2|\widehat{S}| \quad , \tag{2.18}$$

which is used to solve Equation (2.1).

2.3 Resolved and modeled scales

Figure 2.2 displays the differences between the resolved parts of the total turbulent energy spectrum discussed in Section 1.6.3, for different numerical methods.

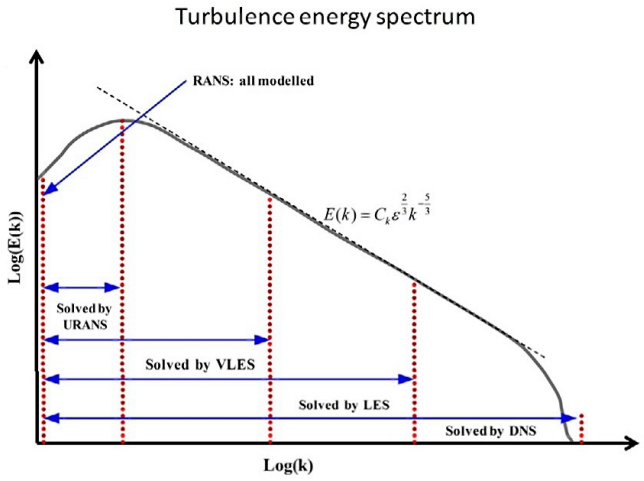

Figure 2.2: Turbulence energy spectrum and resolved scales for different numerical methods. Taken by Argyropoulos and Markatos, 2015.

Focusing on the three models discussed in this thesis it is possible to summarize the following:

- a DNS completely resolves all the turbulent scales computing equation (1.10);
- a LES resolves all the scales below the wavenumber $k = 2\pi/\widehat{\Delta}$ defined by the filter width $\widehat{\Delta}$. The scales above this wavenumber are modelized closing equations (2.6) (e.g. with a Smagorinsky model).
- a RANS takes the equations (1.48) and modelize all the scales (e.g. through the closure method discussed in (1.7)).

Thus pointing out the premise of this Chapter: the LES method is significantly more accurate than the RANS method, and computationally less demanding than a DNS method.

2.4 Boundary Conditions

2.4.1 Periodic conditions

In case the flow analyzed by the simulation presents one or more directions of homogeneity, it can be convenient to specify a periodic boundary condition on that direction, in order to significantly reduce the calculations and the computational costs. Such condition imposes that the domain repeats itself an infinite number of times.

2.4.2 Walls

No-slip condition must be respected in presence of walls; wall stresses are accurately calculated only if wall-layer is well resolved. This is generally accomplished based on a y^+ analysis of the problem, which makes use of the dimensionless wall distance $y^+ = \frac{yu_\tau}{\nu}$, being $u_\tau = (\frac{\tau_w}{\rho})^{1/2}$ (τ_w is the Reynolds shear stress at the wall). Dimensionless velocity is then $u^+ = \frac{u}{u_\tau}$. This parameters are used to estimate the sub-layers thicknesses near a wall.

Referring to Figure 2.3, in the viscous layer ($y^+ < 5$), the fluid is dominated by the viscous effect, so it can be assumed that the Reynolds shear stress is negligible. The "linear velocity law" is given by: $u^+ = y^+$.

In the logarithmic layer ($y^+ > 30$), turbulence stress dominate the flow and velocity profile varies very slowly with a logarithmic function along the wall normal distance: $u^+ = \frac{1}{\kappa} ln(y^+) + B$, where B is a constant.

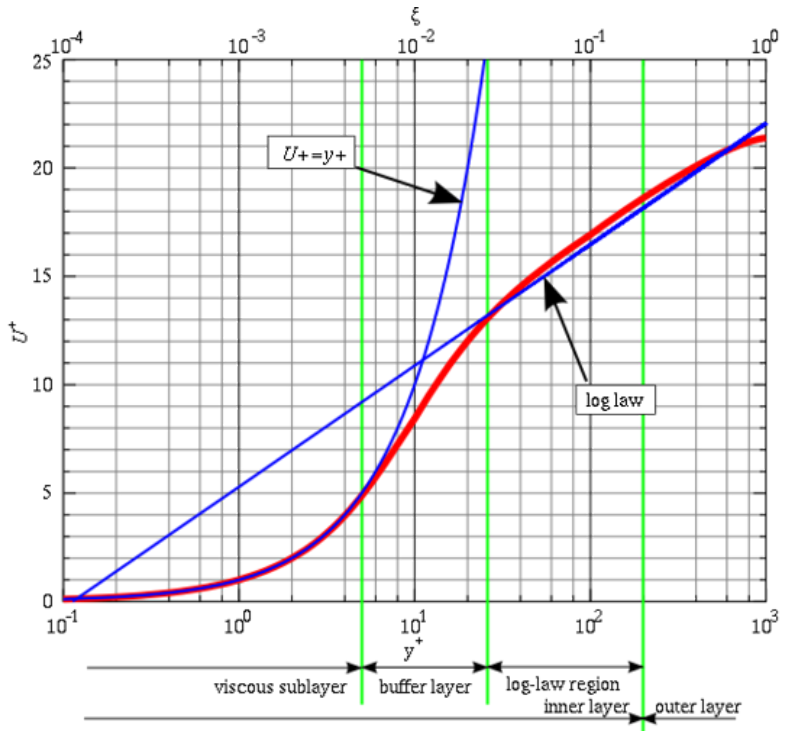

Figure 2.3: Profile of the logarithmic law of the wall.

The buffer layer ($5 < y^+ < 30$) is the transition region between the viscosity-dominated region and turbulence-dominated part of the flow. Viscous and turbulent stresses are of similar magnitude and the velocity profile is not well defined.

Considering this distinction, a wall-layer can be considered resolved if the first grid cell is sufficiently inside the viscous layer (generally $y^+ < 1$) in order to ensure that this layer is not excluded in numerical calculations.

Wall boundary conditions can be also respected using specific wall functions. This are equations empirically derived and used to bridge the inner region between the wall and the turbulence fully developed region. When using the wall functions approach, there is no need to resolve the boundary layer causing a significant reduction of the mesh size and the computational domain. The wall function approach was first proposed by Spalding, 1961. An example is given by the $\nu_t - U$ Spanding wall function which is based on the special relationship between y^+ and u^+:

$$y^+ = u^+ + \frac{1}{B}(e^{\kappa u^+} - 1 - \kappa u^+ - \frac{1}{2}(\kappa u^+)^2 - \frac{1}{6}(\kappa u^+)^3) \quad . \tag{2.19}$$

The curve of this empirical function can fit the curve of $u^+ = y^+$ in the viscous layer and $u^+ = By^+/\kappa$ in the log area.

Chapter 3

Thermally driven circulation inside a mountain boundary layer

The complications that arise trying to approach the problem of a turbulent anabatic flow in neutral stratification are mainly due to the lack of experiments, simulations and theoretical background in the current literature regarding this subject. In order to validate the results of a numerical model, to see if it is adequate to reproduce realistic features or to generate predictions, it is necessary to have at least a work of reference for comparison. This chapter will discuss what the author considered to be the significant background about the concerning topic, through the review of some works useful for reference. It will start describing the basic theoretical mechanisms of slope winds, then it will approach the flow separation problem investigated experimentally by Hocut, Liberzon, and Fernando (2015), followed by the theoretical steady laminar model designed by Prandtl (1942) and finally the DNS performed by Fedorovich and Shapiro (2009) on slope winds in stable stratification. Each of these works will serve as a reference in the following analysis.

3.1 Upslope winds

One of the first mechanisms proposed to explain slope winds back in 1920's was the vorticity production by baroclinicity of the air above a heated surface (Wenger, 1923). Bjerknes' circulation theorem (see, for example, Kundu and Cohen, 2001) says that integral circulation of the wind field U along a closed path l, $C = \oint U \cdot dl$ varies in time according to variations in latitude ϕ, area of integration A and

interactions between pressure and density fields:

$$d_t C = -2\Omega d_t(A sin\phi) + \frac{dp}{\rho} \quad , \tag{3.1}$$

where Ω is the angular velocity of the Earth. Last term of the equation is not zero only in a baroclinic stratification (because in barotropic case it is immediately seen using the hydrostatic balance that the integral became $\oint g dz = 0$).

The circuitation C is also the local vorticity of the fluid (see this by applying the Stokes' theorem). Thus if the baroclinicity varies, vorticity is generated and a circulation develops.

Aside from Wenger explanation, baroclinicity is expressed in the vorticity equation (1.34) as the baroclinic torque $\nabla \times b\hat{k}$, in which appears the buoyancy. Thus the vorticity generation can be intuitively described in terms of buoyancy force that is acting on a fluid particle over the slope: if heat flux is transmitted from the slope surface to the fluid above it, isothermal lines are folded downward creating a non-zero horizontal temperature gradient. Referring to Figures 3.1 and 3.2, in which potential temperature θ is used, this translates into a difference $\theta_2 - \theta_3 < 0$ and $\theta_2 - \theta_1 > 0$ respectively in the katabatic and the anabatic problem.

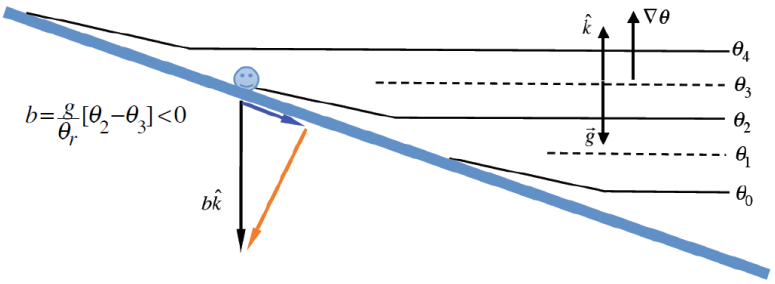

Figure 3.1: cascade

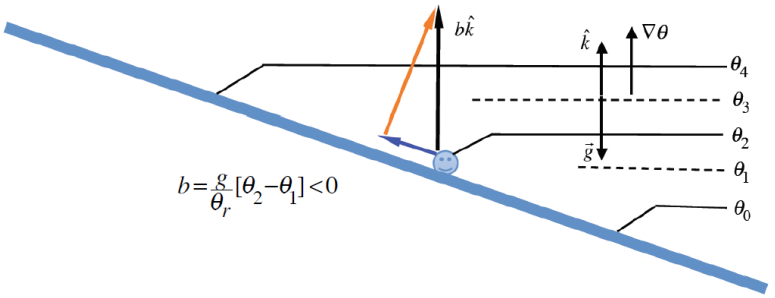

Figure 3.2: Sketch of buoyancy generated motion (Shapiro,June 2012)

The along slope component of the buoyancy force is thus negative in the katabatic case, generating a downward motion, and positive in the anabatic case,

generating an upward motion.

3.1.1 Hocut's work on flow separation

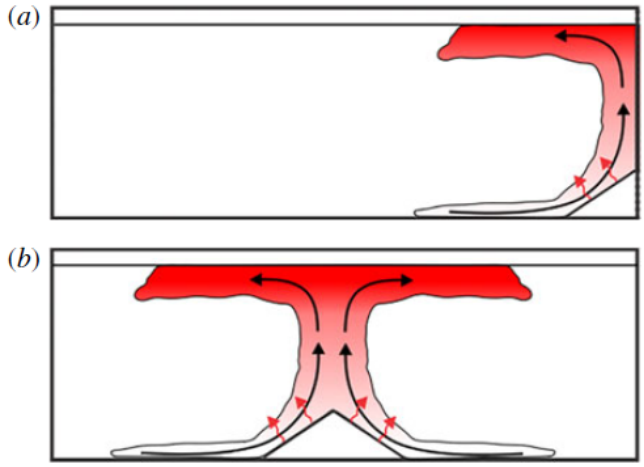

Figure 3.3: Hocut's tank configuration (Hocut, Liberzon, and Fernando, 2015).

Hocut, Liberzon, and Fernando (2015) studied flow separation occurrence over a uniformly heated slope immersed in a neutral stratified fluid. The study has been conducted monitoring a tank full of water of dimensions $125 \times 30 \times 30$ cm with two different configurations, as depicted in Figure 3.3: a single slope of 15.6×30 cm positioned on one side of the tank, and a double slope positioned at the center of the tank. Both configurations has been proved to be equivalent in the flow behaviour along the slopes. Neutral stratification has been established letting the fluid have a homogeneous background temperature, while heating of the slope has been accomplished applying a constant DC current from an external power supply. Experiments has been done for variations of β from 0° to 45°, and variations of supplied heat flux from 9.4W/m^2 to 2KW/m^2, leading to a Reynolds number $Re = \frac{(q_o H)^{1/3}}{\nu} = 0 \div 300$. Flow was monitored by the Particle Tracking Image method via CCD camera of 752 pixel resolution and 5fps of sampling frequency, pathlines was analyzed by an image analysis software in order to locate the point separation of the flow (see fig 3.4).

Theoretical approach of the article is the following: taking the vorticity equation written in (s, y, n) coordinates (see figure 3.5):

$$\partial_t \omega + u \cdot \nabla \omega = \omega \cdot \nabla u + \nabla \times b\hat{k} + \nu \nabla^2 \omega \quad , \tag{3.2}$$

focusing on the y component of the vorticity equation, neglecting viscosity, one gets:

$$\partial_t \omega_y = (\nabla \times b\hat{k})_y - u\partial_s \omega_y \quad . \tag{3.3}$$

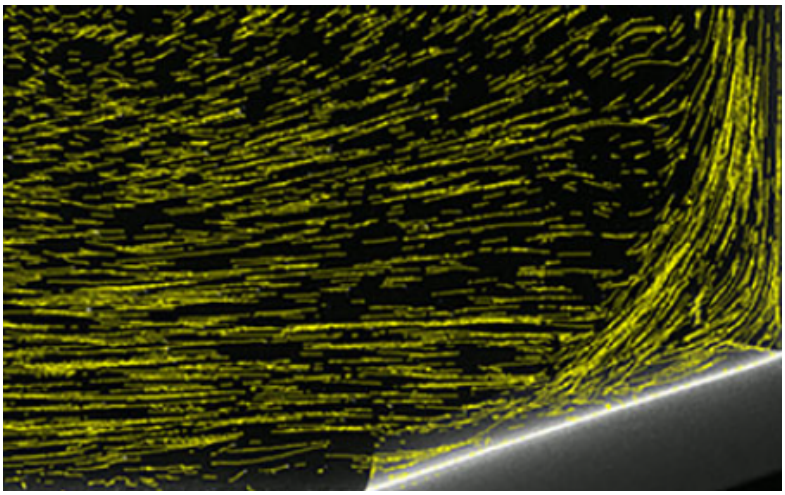

Figure 3.4: Particle tracking done by Hocut, Liberzon, and Fernando, 2015.

If density profiles are strongly temperature dependent, $\nabla \times b\hat{k}$ can result in a value higher than vorticity advection due to shear flow, thus causing the fluid to separate from the slope.

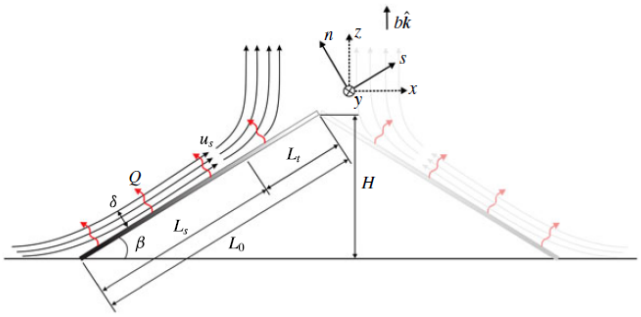

Figure 3.5: Sketch of vorticity production taken by Hocut, Liberzon, and Fernando, 2015

From a scaling analysis, the authors derived a functional relation between the separation length L_s, i.e. the distance from the bottom of the slope to the point at which separation occurs, and the slope angle β:

$$\frac{L_s}{L_0} = (1 + \Pi \frac{sin^{1/4} 2\beta}{sin\beta})^{-1} \quad , \tag{3.4}$$

where Π is a proportionality constant arising from scaling. The fitting curve is showed in Figure 3.6. Scale analysis done by Hocut is valid only under the assumptions of neutral stratification and for β values greater than a critic $\beta_c = 20$, under which there seems to be a regime transition. Observations confirm that above such critic angle, separation length increases with increasing slope angle.

Sampling showed in Figure 3.7 demonstrates the independence of length separation from the Reynolds number.

This graph is also useful to estimate which values of separation length one can

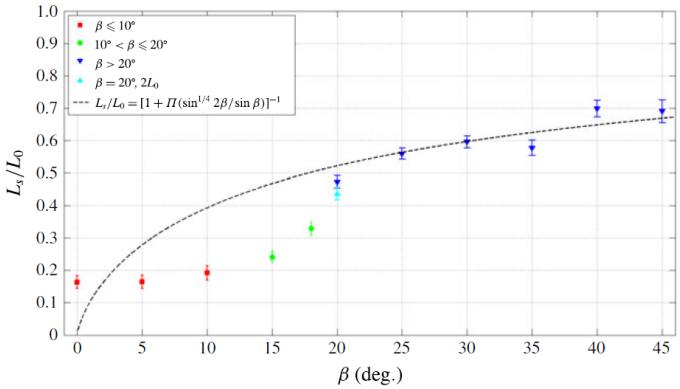

Figure 3.6: Relation between separation length and slope angle found by Hocut, Liberzon, and Fernando, 2015

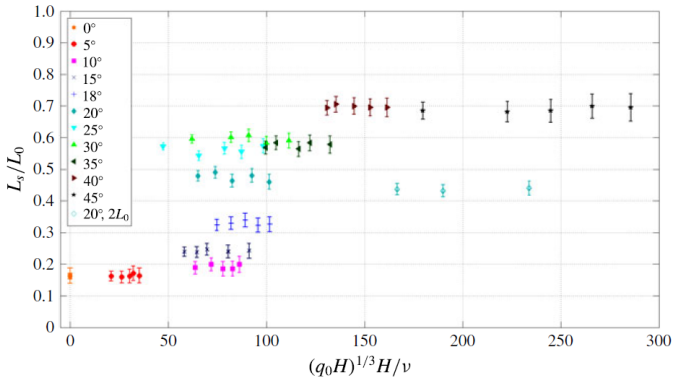

Figure 3.7: Independence of length separation from Reynolds number found by Hocut, Liberzon, and Fernando, 2015.

expect for a certain Reynolds number and a certain slope angle. Even in this case, as in Figure 3.6, a regime change seems to be observed between under-critical and super-critical slope angles.

3.1.2 Prandtl's model

Prandtl formulated in 1942 a set of equations for velocity and buoyancy of slope winds in slope-following coordinates (XYZ) defined in figure 3.8.

The model assumed steady state ($\partial_t = 0$), infinite plane of constant angle α,

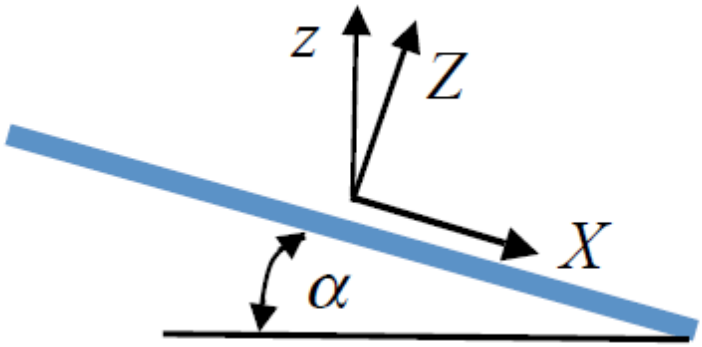

Figure 3.8: Reference system for the governing equations.

constant Brunt-Vaisala frequency $N = \sqrt{\frac{g}{\theta_r} d_z \theta}$, constant eddy viscosity ν and eddy diffusivity α, no external forcing, neglected Coriolis force, and uniform heat flux. Equations written in terms of u, v, w velocities, b buoyancy and $\tilde{p}$ the non hydrostatic pressure, are:

$$d_t u = \frac{1}{\rho_r} \partial_X \tilde{p} - b sin\alpha + \nu \nabla^2 u \quad , \tag{3.5}$$

$$d_t v = \frac{1}{\rho_r} \partial_Y \tilde{p} + \nu \nabla^2 v \quad , \tag{3.6}$$

$$d_t w = \frac{1}{\rho_r} \partial_Z \tilde{p} + b cos\alpha + \nu \nabla^2 w \quad , \tag{3.7}$$

$$d_t b = u N^2 sin\alpha - w N^2 cos\alpha + k \nabla^2 b \quad . \tag{3.8}$$

At the slope (Z=0) the boundary conditions are: no slip condition $u, v = 0$ and impenetrability $w = 0$ for velocity, and prescribed b flux at surface. At $Z \to \infty$ both buoyancy and velocity goes to zero. Once boundary conditions are applied, they implies that $v = w = 0$ everywhere and $u, b, \tilde{p}$ are only functions of Z:

$$0 = -b sin\alpha + \nu d_z^2 u \quad , \tag{3.9}$$

$$0 = u N^2 sin\alpha + k d_z^2 b \quad . \tag{3.10}$$

Solving with respect to u, one obtains:

$$0 = d_z^4 u + \frac{N^2 sin^2\alpha}{\nu k} u \quad . \tag{3.11}$$

Assuming a solution of the kind $u = \sum C_i e^{m_i Z}$, applying boundary conditions, one obtains an explicit solution for u and b:

$$u = -\frac{b_0}{N}\sqrt{\frac{k}{\nu}} e^{-\frac{Z}{\delta}} sin(\frac{Z}{\delta}) \quad , \tag{3.12}$$

$$b = b_0 e^{-\frac{Z}{\delta}} cos(\frac{Z}{\delta}) \quad . \tag{3.13}$$

The characteristic profile of such solutions is sketched in figure 3.9 Some qualitative

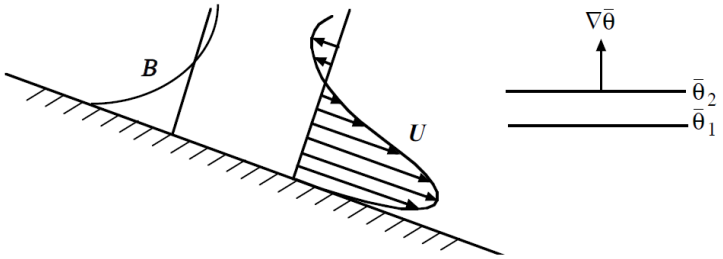

Figure 3.9: Prandtl linear model solutions sketched over the slope.

features can be assessed from Figure (3.9): velocity's profile is characterized by a marked peak's region near the surface and an upper velocity region of inverted sign. Buoyancy is characterized by a monotonic increase (or decrease in anabatic case) and an upper region of inverted sign. These solutions will be further analyzed in Section 3.2.1 and Section 4.6.3.

3.2 Numerical modeling of a slope wind

3.2.1 Fedorovich and Shapiro direct numerical simulations

Fedorovich and Shapiro (2009) performed DNS simulations of a buoyantly driven slope flow of a stratified fluid along a double-infinite inclined surface whithin the conceptual framework of the Prandtl model of which are reported, in Figure 3.10, vertical profiles of u and b for $\alpha = 10, 30, 60, 90$ and two types of heat flux specification: type I specifies b value at the surface $b_s = 0.1 m/s^2$, type II specifies b flux at the surface $B_s = (-\nu d_z b)_s = 1 m^2/s^3$ for $\nu = 1 m^2/s$ and $N = 10^{-2} s^{-1}$.

The authors points out that the surface buoyancy value, as well as the elevation and intensity of the velocity maximum, increases with decreasing slope angle as $sin^{-1/2}\alpha$.

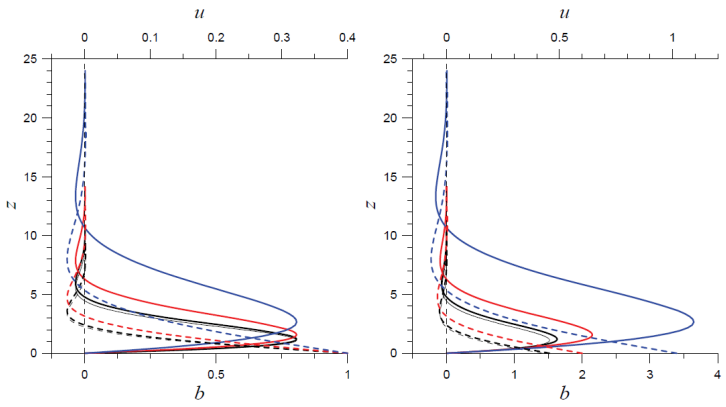

Figure 3.10: Prandtl solutions profiles from the work of Fedorovich and Shapiro (2009)

Turbulent flow equations are then written in a reference system of coordinates (x, y, z) rotated with respect to the z' axis. Averaging the governing equations over

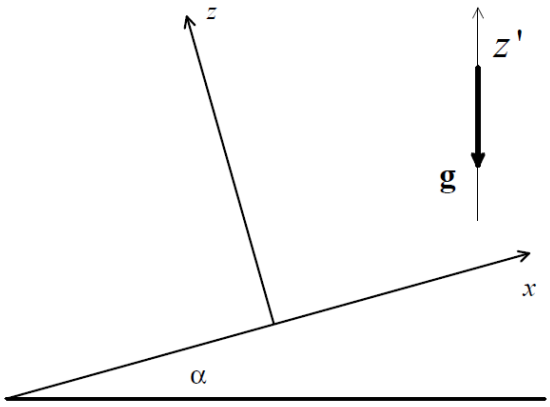

Figure 3.11: Reference system for the governing equations.

time and spatially over x-y planes parallel to the slope they obtained:

$$\overline{b}sin\alpha + \nu\partial_z^2\overline{u} - \partial_z\overline{u'w'} \quad , \tag{3.14}$$

$$-N^2\overline{u}sin\alpha + \nu\partial_z^2\overline{b} - \partial_z\overline{b'w'} \quad , \tag{3.15}$$

$$-d_z\overline{\pi} + \overline{b}cos\alpha - \partial_z\overline{w'w'} = 0 \quad , \tag{3.16}$$

in which primes signify deviations from average, denoted by overbars. Boundary conditions are $\overline{u} = 0$, $-\nu d_z\overline{b} = B_s$ at $z = 0$, and $\overline{u} = 0$, $\overline{b} = 0$ at $z \to \infty$.

By integrating equation 4.6.3.2 from 0 to ∞ the volume flux is obtained:

$$V_I L_I = \int_0^\infty \overline{u}dz = \frac{B_z}{N^2 sin\alpha} \quad . \tag{3.17}$$

From this, integral Reynolds number is derived as: $Re_I = \frac{|V_I L_I|}{\nu} = \frac{|F_{pb}|}{sin\alpha}$, defining the flow forcing parameter $F_{pb} = B_s \nu^{-1} N^{-2}$.

Simulations were performed with Re_I in the range from 3000 to 10000 in a $256 \times 256 \times N_z$ grid with N_z varying from 400 to 800 and uniform spacing Δ such that $\Delta < 2(\nu^{3/4}|B_s|^{-1/4})$ as an analogous of the Kolmogorov scale. Buoyancy flux are prescribed for both katabatic case ($B_s < 0$) and anabatic case ($B_s > 0$). Figure 3.12 shows the moinitored temporal evolution of the anabatic flow along-slope velocity and buoyancy at four different distance above the slope. They noted quasi-stationary oscillations after an initial transitional phase between laminar and turbulent regime. The frequency $Nsin\alpha$, consistently with other works, has been associated with internal gravity waves . Turbulent fluctuations has been seen gradually fading with distance from the wall while periodic oscillations persisted inside the outer laminar region before fading out.

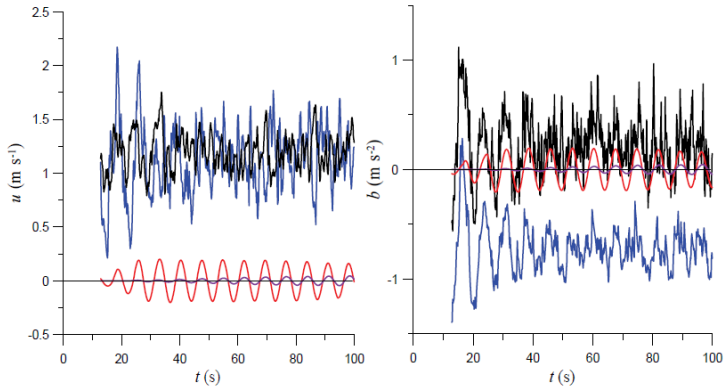

Figure 3.12: Time evolution of velocity and buoyancy at different heights from the slope. Taken by Fedorovich and Shapiro (2009).

In their profile analysis, Fedorovich and Shapiro, 2009a) found that flows appears similar to the corresponding laminar Prandtl counterparts, with more differences in the anabatic case than in the katabatic ones: in the turbulent katabatic flow, fluid cooler than environment descends along the sloping surface, whilst fluid warmer than environment moves upslope at some distance from the surface; turbulent anabatic flow exhibits the opposite behaviour. In the katabatic flow, turbulence in the immediate vicinity of the slope resulted suppressed by the combination of stable background stratification and negative surface buoyancy. Also a sharp near-surface buoyancy increase has been observed, supposedly enhanched by suppression of vertical exchange of heat, due to stable stratification. Jet maximum has not been observed to shift away from the slope with decreasing angle as noticeably as in the Prandtl model. In the anabatic flow, the positive surface buoyancy flux at the near surface region are seen acting as a turbulence production mechanism, opposing the effects of stable stratification togheter with shear generation. Vertical mixing has been observed to be moer efficient with decreasing slope angle. Effects of enhanced

mixing are also seen by the authors in the reduced values of the surface buoyancy profile and a near independence of the surface buoyancy from the angle.

Buoyancy variance has been observed to assume maximum magnitude very close to the wall, inside the region where maximum gradients are observed in the mean buoyancy profile. Slope-normal fluxes of momentum $\overline{u'w'}$ and buoyancy $\overline{b'w'}$, featured maximum and minima closely co-located with the zero crossing in the mean profiles of u and b. The authors also report that ordinates of zero fluxes were closely co-located with the ordinates of zero gradients of the corresponding mean profiles. Thus turbulent fluxes appeared generally anti-correlated with the corresponding mean gradients for both the simulated flow types.

No region of flux constancy has been observed. The authors argued that this may be a specific feature of the slope flows in the presence of ambient stratification.

No region has been found in which any of the governing parameters (B_s, ν, N or α) could be dropped from consideration.

The authors observed that the development of velocity fluctuations normal to the wall was hampered by the presence of the wall, explaining in this way the slow growth with z and smaller values of $\overline{w'w'}$ compared to $\overline{u'u'}$ and $\overline{v'v'}$. Profiles of both $\overline{u'u'}$ and $\overline{v'v'}$ showed presistents secondary maxima in the vicinity of the wall, at distances comparable to those of the mean velocity maxima/minima.

Finally, studying forcing sensitivity of the flow under $|F_{pb}| = 3000, 5000$, The author found that they exhibits little changes in magnitude but no differences in maxima's height.

Chapter 4

Numerical approach and validation

4.1 Discretization of equations

In order to solve the Navier-Stokes equations with a LES or RANS approach, a discretization procedure of the equations is needed. In doing so, algebraic expressions can be obtained and computed. As a following step, a resolution strategy must be carried out for solving the coupled discretized momentum and continuity equation. For the sake of clarity, this section will consider a simplified form of the PISO alghoritm (Oliveira and Issa,2001) in order to explain the construction of the discretized algorithm.

It will be considered a one dimensional inviscid flow along the x direcion aligned with gravity. From here on will be defined $\rho_k = 1 - \beta(T - T_0)$ to account for the Boussinesq approximation. Momentum equations reads:

$$\partial_t u + \partial_j(uu) = -\partial_x p + \rho_k g \quad . \tag{4.1}$$

This equation contains a non-linear convection term coupling the velocity u and a linear term coupling p and u. According to Nillson[1]: on low Courant numbers (small time-step), the pressure-velocity coupling is much stronger than the non-linear coupling. It is therefore possible to repeat a number of pressure correctors without updating the discretization of the momentum equation. In such a setup, the first pressure corrector will create a conservative velocity field, while the second and following will establish the pressure distribution.

Therefore at each time step, velocity is predicted in a *predictor* step and then both velocity and pressure will be corrected in a *corrector* step.

Consider, for example, an Euler implicit first-order method with time step n and spatial step i, with second-order linear interpolation of values from the cell center positioned in i to the cell faces shifted by a factor $\frac{1}{2}$, where linearization of the convective term is done by taking it from the old time step n. The predictor step is:

$$(\frac{1}{\Delta t} + \frac{u^n_{i+1/2} - u^n_{i-1/2}}{2\Delta x})\Delta V u^*_i + (\frac{u^n_{i+1/2}}{2\Delta x})\Delta V u^*_{i+1} - (\frac{u^n_{i-1/2}}{2\Delta x})\Delta V u^*_{i-1} = \frac{u^n_i}{\Delta t}\Delta V - (\partial_x p)^n_i \Delta V + (\rho_k g)^n_i \Delta V \quad , \tag{4.2}$$

where the pressure term taken from the old n is yet unknown. In matricial form it is written

$$Cu^* = r - \nabla p^n + \rho_k g^n \quad , \tag{4.3}$$

with C the coefficient array of the discretization method adopted, r contains the

[1] `http://www.tfd.chalmers.se/~hani/kurser/OS_CFD_2008/implementApplication.pdf`

explicit source terms except the pressure gradient. Including viscous and turbulent stress terms would modify the matrix C without changing the general form. Writing $C = A + H'$ as the sum of diagonal and off diagonal matrices, the equation **??** is rewritten as

$$Au^* + H'u^* = r - \nabla p^n + \rho_k g^n \quad . \tag{4.4}$$

The corrector step solves the velocity u^{**} from the just predicted u^*, the old velocity u^n and the first corrected pressure p^* that, however, is still unknown. The step is written as:

$$(\frac{1}{\Delta t} + \frac{u^n_{i+1/2} - u^n_{i-1/2}}{2\Delta x})\Delta V u^{**}_i + (\frac{u^n_{i+1/2}}{2\Delta x})\Delta V u^*_{i+1} - (\frac{u^n_{i-1/2}}{2\Delta x})\Delta V u^*_{i-1} = \frac{u^n_i}{\Delta t}\Delta V - (\partial_x p)^n_i \Delta V + (\rho_k g)^n_i \Delta V \quad . \tag{4.5}$$

In matrix form:

$$Au^{**} + H'u^* = r - \nabla p^* + \rho_k g^n \quad . \tag{4.6}$$

Introducing $H = r - H'u^*$, inverting A and taking the divergence of the above equation, one gets (because of the fact that $\nabla u^{**} = 0$)

$$\nabla^2(A^{-1}p^*) = \nabla(A^{-1}H + A^{-1}\rho_k g^n) \quad , \tag{4.7}$$

from which is computed the requested p^*, then solved the previous equation for u^{**}.
Eventually, a second corrector step can be performed finding a p^{**}, then solving for a u^{***}.Note that the algorithm is completely general and not bonded by the Euler method: any other implicit time stepping method, as a Crank-Nicholson, will be obtained just modifying the coefficients inside A and H.

4.1.1 Solving schemes

The derivative terms are calculated based on the choice of discretisation practice where standard Gaussian finite volume integration is the common choice [2]. Gaussian integration is based on summing values on cell faces, which must be interpolated from cell centres.

In the actual simulations, a Gauss linear interpolation scheme is adopted; time derivative are discretized with a backward Euler scheme, while calculations of the velocity advective terms are also done using a linear scheme.

Before using the linear scheme, a bounded version of the Gaussian scheme has been tested. The bounded scheme retains the discretization of the ∇U term

[2] `https://cfd.direct/openfoam/user-guide/v6-fvschemes/`

inside the equation even for incompressible flows because of the non-zero value that it assumes until numerical convergence of the solution. This gaussian scheme is hybridized with Upwind through a gamma parameter that has been manually set equal to 0.2. The results obtained from these schemes were not physically significant due to the strong diffusive effects of the bounding scheme and the artificious numerical treatement of the upwind.

4.2 Cases specification

Three different simulations are built based on the work of Liberzon (not yet published). Details of the simulations' set up are treated in Section 4.4. Each simulation is set having a different value of temperature at the surface, in order to simulate three different heat fluxes coming from the slope. This allows to test the sensitivity of the anabatic flow simulated to variations in Reynolds number.

Validation of the simulations is done selecting one of the three simulations and comparing the results obtained with three other results: the Prandtl laminar solutions described in Section 3.1.2, the Fedorovich's dataset produced with the DNS described in Section 3.2.1 and the Liberzon's dataset whose experiment details are described in the following Section 4.2.1. The reasons for choosing this datasets will be explained togheter with the validation analysis in Section 4.7.

4.2.1 Liberzon's case

The reference case for model validation is Liberzon's work in which the experiment is done in a tank full of water of dimensions $0.7 \times 0.5 \times 0.6cm$ with a double slope configuration as depicted in Figure 4.1 of dimensions $30 \times 50cm$. The slope angle is 35° and the surface is supplied by $992W/m^2$ of heat flux.

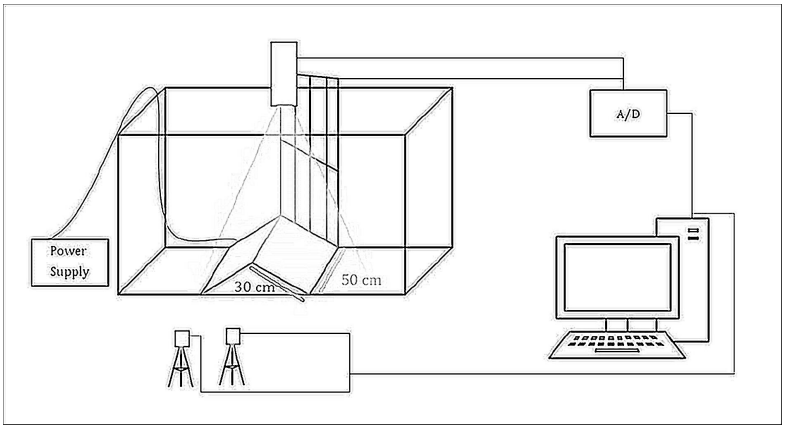

Figure 4.1: Liberzon's experiment configuration.

Temperature data are taken along the points aligned along the center of the slope, as showed in Figure 4.2, and measured with thermocouples; the velocity field is monitored by two cameras and a particle image velocimetry on a 2-dimensional grid along the central cross section of the domain. Both temperature and velocity data were given to us by the authors. Fluid is assumed in neutral stratification, and Reynolds number is 800.

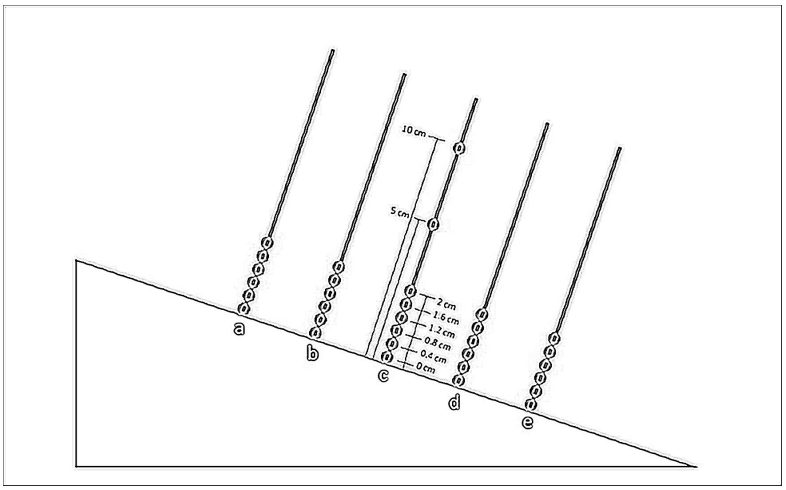

Figure 4.2: Sketch describing the points of temperature measurement along the slope

4.3 OpenFOAM toolbox

OpenFOAM (Open-source Field Operation And Manipulation) is a C++ toolbox for numerical solution of fluid dynamic problems. A typical workflow involving a simulation with OpenFOAM is depicted in figure 4.3

Based on the official website, OpenFOAM is defined as a C++ library used to create executable known as applications. The applications fall into two categories: the *solvers* designed to solve a specific problem in continuum mechanics, and the *utilities* designed to perform tasks that involve data manipulation in both the pre and post-processing phases.

The solver chosen for computing the simulations of this work is the *buoyantBoussinesqPimpleFoam*, the one prescribed for Newtonian incompressible fluids under Boussinesq approximation in heat transfer problems.

The equations solved by the *buoyantBoussinesqPimpleFoam* are those discussed in Section 4.1. The Smagorisky turbulent model is use along with the Van Driest dumping function for wall boundaries.

In order for the simulation to work, the solver in OpenFOAM must take informations from the case directory that must be prepared in the pre-processing

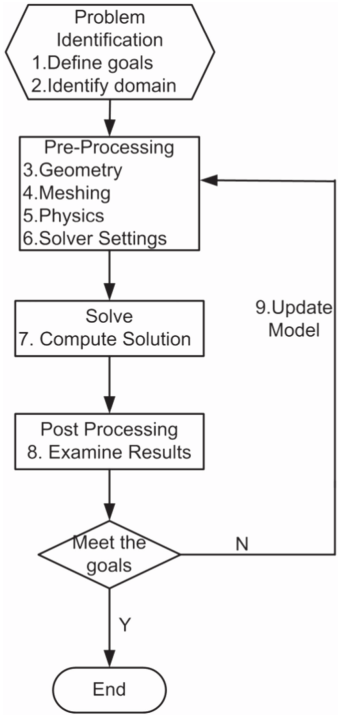

Figure 4.3: Workflow sketch for a typical CFD simulation. Taken by Pan et al.,(2017).

phase for the simulation to work. The tree structure of the files contained in a typical functioning case directory is as follows:

- *system/*:
  - *blockMesh* describes the geometrical domain in which the simulation occurs, the coordinate of its shape, the cell's number in each direction, the definition of each boundary and their physical type;
  - *fvSchemes* contains informations on which scheme to use for the discretization of each of the differential operators that appears in the equations;
  - *fvSolutions* permits to specify the details for the methods of calculation for handling the matrix operations;
  - *fvOptions* permits to add eventual source terms to the equations without the need to rewrite the solvers;
  - *controlDict* is the script containing the definition of resolution time Δt at which executing calculations, maximum Courant number permissible before blocking a simulation, as well as the total duration time of the simulation and the output saving options;
  - *probes* gives the possibility to specify coordinates inside the domain at which saving output field values for analysis purposes;
  - other configuration files.

- *constant/*:
  - *polyMesh* contains detailed informations about point's coordinates of the domain and specification of each type of boundary;
  - other dictionaries containing informations such as transport properties (in which the fluid involved is specified) and turbulence properties (in which the turbulent model is specified).
- 0/:
  - field's files containing, for each field, the initial conditions and the boundary conditions at each geometrical domain's face.

4.4 Simulations set up

The water tank simulated from the Liberzon's experiment in each of the three simulations implemented, has been generated as in Figure 4.11a by a parallelepiped of dimensions $L_x = 1$ m, $L_y = 0.6$ m, $L_z = 1.2$ m. A slope of 0.3 m with angle $\alpha = 35°$ has been set in the right bottom part of the domain (Figure 4.11b) with a symmetrical boundary condition simulating a double central slope configuration.

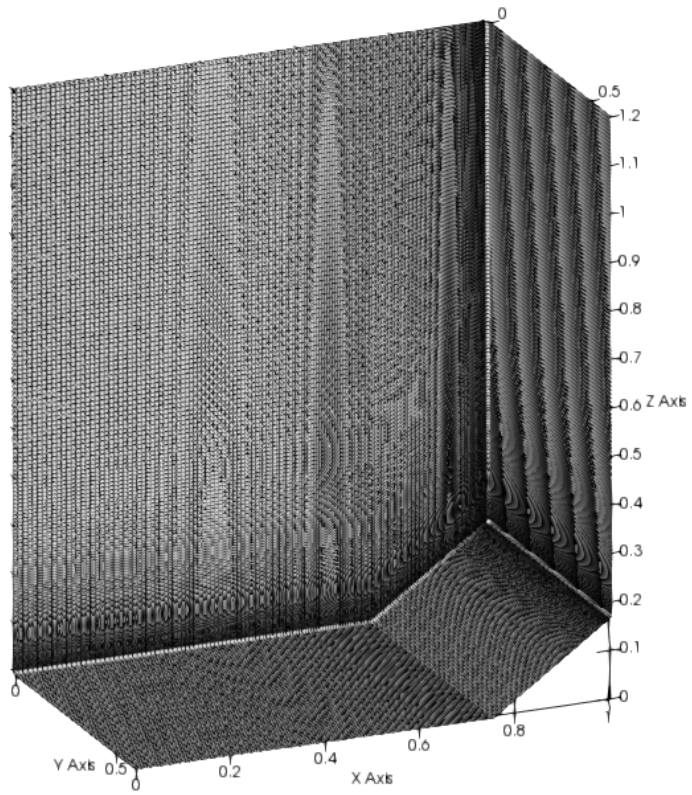

(a) Entire domain of the water tank.

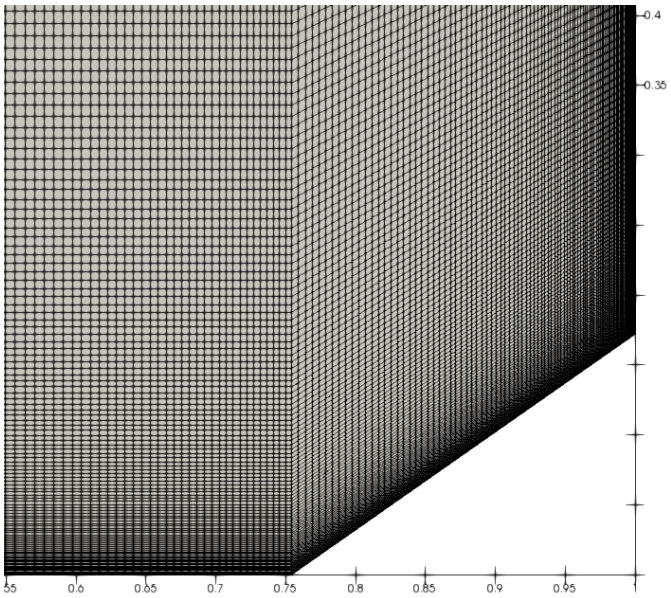

(b) Slope region.

Figure 4.4: Geometry of the water tank.

4.4.1 Simulation parameters

The fluid's physical properties and the domain geometric specifications used for setting the three simulations have been used also for the scale analysis and non-dimensionalization of velocity and temperature fields. Table 4.1 summarize the principal values of the slope geometrical parameters and water transport properties.

Physical properties	Value	Description
L	0.3 m	Slope length
$H = L\sin(\alpha)$	0.172 m	Height length
β_T	2.1×10^{-4} 1/K	thermal expansion coefficient
ρ	1×10^{3} kg/m^3	water density
ν	1×10^{-6} m^2/s	kinematic viscosity
D	1.63×10^{-7} m^2/s	thermal diffusivity
k_T	0.6 W/(m K)	thermal conductivity
c_p	3.68×10^{3} J/(kg K)	specific heat at constant pressure

Table 4.1: Physical property of the simulation. (Each of the thermodynamic quantities is referred to water.)

From the Reynolds number defined in Section 1.8.2

$$Re = \frac{UL}{\nu} = \frac{(q_0 H)^{1/3} H}{\nu} \quad ,$$

where $q_0 = \beta\overline{w'T'}$ is the buoyancy flux defined in Section 1.8.2, the characteristic velocity w_* has been derived. An alternative expression for q_0, based on the thermodynamic properties of the fluid is $q_0 = \frac{Q\beta g}{\rho c_p}$ (measured in J/s), from which a different formulation of the characteristic velocity scale is:

$$U_q = (q_0 H)^{1/3} = (\frac{Q\beta g}{\rho c_p} H)^{1/3} \quad , \tag{4.8}$$

From this definition of U_q it is possible to obtain a characteristic time $\tau = \frac{L}{U_q} =$ 103.45 s.

After comparing the results of a boundary condition based on the flux specification Q against a boundary condition based on the temperature difference specification ΔT (the comparison is not showed here), it has been chosen the latter as the selected method. For this reason in the present scaling analysis it has been used a different characteristic scale velocity, obtained from $\Delta T = T_s - T_e$, the difference between the slope temperature T_s and the environmental temperature T_e. From the Rayleigh number defined in section 1.5 $Ra = \frac{g\beta L^3 \Delta T}{\nu D}$ it is derived the characteristic velocity $U_T = \sqrt{g\beta L \Delta T}$.

The table 4.2 shows the values of this parameters for the present simulation, together with it's Prandtl number defined in Section 1.5 $Pr = \frac{\nu}{D}$.

Derived quantities	
Pr	6.135
q_0	1.48×10^{-7} m^4/s^3
Q	265.578 W/m^2
Re_Q	507.02
U_Q	0.0029 m/s
Ra	3.7×10^8
U_T	0.0261 m/s
τ	103.45 s

Table 4.2: quantities derived from the physical parameters of table 4.1

4.4.2 Similarity with environmental flows

in Section 1.5, the Rayleigh number has been presented as a non-dimensional parameter strongly related with natural convection. In order to have a reference value of Ra for environmental convective flows (such as the katabatic or anabatic flows along a mountain or a valley), the Rayleigh number is estimated for the case of Granite Mountain (USA) described by Hocut, (2015).

The physical and geometrical parameters, along with the estimated Ra value, are reported in Table 4.3. The same estimation is done for the present simulation and the reference experiment. The comparison shows that Ra is much larger in real case applications with respect to the reduce scale experimental and, consequently, the numerical simulation. This is due to the large characteristic length of real geometries, which practically determines the order of magnitude. In light of this, it is necessary to state if there is critical value up to which there is a sort of Rayleigh independence of the anabatic flows, or if with increasing Ra different flow regimes establish. Unfortunately, numerical simulations are still limited and cannot afford very high Ra such as that one of Granite Mountain.

In the present work, the flow regimes are analyzed at three Rayleigh, spanning into two order of magnitude: 2.8×10^7, 7.1×10^7, 1.8×10^8.

	Granite mountain (air)	Simulation (water)	Experiment (water)
ν	1.5×10^{-5} m$^2/s$	1.0×10^{-6} m$^2/s$	1.0×10^{-6} m$^2/s$
D	2.1×10^{-5} m$^2/s$	1.4×10^{-7} m$^2/s$	1.4×10^{-7} m$^2/s$
β_T	3.4×10^{-3} 1/K	2.1×10^{-4} 1/K	2.1×10^{-4} 1/K
H	6.0×10^2 m	1.72×10^{-2} m	1.72×10^{-1} m
ΔT	1 K	1.1 K	1.49 K
Ra	2.3×10^{16}	7.0×10^7	9.6×10^7

Table 4.3: Physical and geometrical parameters for the Granite Mountain measurement (Hocut,2015), present numerical simulation, reference experiment.

4.4.3 Geometry and Mesh

The tank simulated has been structured with a grid of 192x96x192 cells.

Along the vertical axis has been applied an hyperbolic stretching of the kind:

$$z(\eta) = \frac{1}{2}(1 + \frac{tanh(\delta(\eta - 1/2))}{tanh(\delta/2)}) \quad , \tag{4.9}$$

η being the original vertical coordinate, and z being the vertical coordinate stretched through the parameter δ.

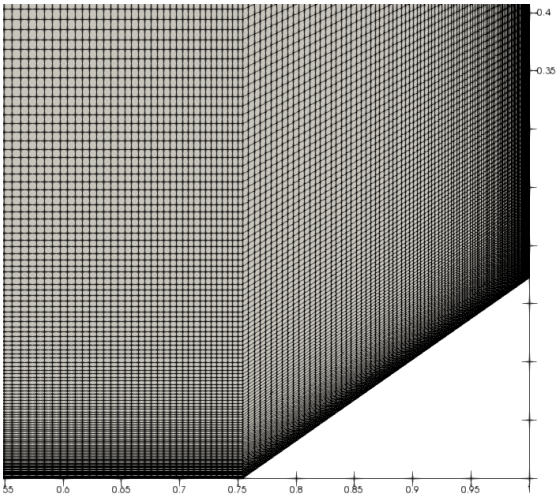

Figure 4.5: Hyperbolic grid spacing.

Hyperbolic stretching ensures that the grid points are asymmetrically distributed with greater density near the slope and lesser density far away from it, in order to focus on the slope dynamic and reduce the computational costs in regions of less interest. In the same way, an hyperbolic stretching has been applied over the horizontal direction in the domain region that does not contain the slope, so that grid is coarser moving toward the rear face.

4.4.4 Boundary Conditions

The six boundaries of the tank are defined as: floor, front, ceiling, back, right and left. For each of the simulations has been defined as *walls* the ceiling and floor of the domains. *Cyclic* conditions have been imposed on the homogeneity direction y, i.e. left and right, in order to reduce the computational cost. A *symmetry* condition has been imposed for the front face in order to account for a configuration that would be equivalent to Liberzon's experiment setup but with minor computational cost. The back face has been set as a generic *patch* on which gradients of temperature, pressure and velocity fields goes to zero. On the ceiling, the *nutUSpaldingWallFunction wall function* of the kind described in Section 2.4.2

has been applied in order to manually set respected the law of the wall and reducing possible numerical issues for the velocities that reach the ceiling.

$$T = \begin{cases} \begin{cases} T^*, & \text{slope region} \\ 296.15, & \text{elsewhere} \end{cases}, & \text{floor} \\ 296.15, & \text{back, ceiling} \\ symmetry, & \text{front} \\ cyclic, & \text{right and left} \end{cases}, \tag{4.10}$$

$$u(x,y,z) = \begin{cases} (0,0,0), & \text{floor, back, ceiling} \\ symmetry, & \text{front} \\ cyclic, & \text{right and left} \end{cases}, \tag{4.11}$$

$$\alpha_T, \nu_T = \begin{cases} \nabla \alpha_T = 0, & \text{floor} \\ wallfunction, & \text{ceiling} \\ symmetry, & \text{front} \\ wallfunction, & \text{back} \\ cyclic, & \text{right and left} \end{cases}, \tag{4.12}$$

$$g(x,y,z) = \begin{cases} (0,0,-9.81), & \text{floor} \\ (0,0,0), & \text{ceiling} \\ symmetry, & \text{front} \\ \nabla g = 0, & \text{back} \\ cyclic, & \text{right and left} \end{cases}, \tag{4.13}$$

$$p_{rgh} = \begin{cases} fixedflux0, & \text{floor, ceiling, back} \\ symmetry, & \text{front} \\ cyclic, & \text{right and left} \end{cases}, \tag{4.14}$$

$$p = \begin{cases} calculated, & \text{floor, ceiling, back} \\ symmetry, & \text{front} \\ cyclic, & \text{right and left} \end{cases}, \tag{4.15}$$

where T^* is set for each of the simulations in order to obtain the following ΔT with respect to the environmental temperature. Table 4.4 summarize the values.

Simulation label	ΔT
LES1.10	1.1°C
LES2.78	2.78°C
LES0.44	0.44°C

Table 4.4: Temperature differences for each simulation.

4.4.5 Modified solver

The buoyantBoussinesqPimpleFoam code has been modified in order to account for a clipping procedure for the temperature field. This procedure consists in imposing that temperature values lower than the environmental temperature are automatically set equal to it, avoiding non-physical temperatures arising from numerical calculations.

4.4.6 Initial conditions

Initial condition for temperature is set equal to the environmental temperature, while each other field has been set to zero, except gravity.

$$T = 296.15K \quad , \tag{4.16}$$

$$u(x, y, z) = (0 \quad ,0 \quad ,0) \quad , \tag{4.17}$$

$$\alpha_T, \nu_T, p, p_{rgh} = 0 \quad , \tag{4.18}$$

$$g(x, y, z) = (0 \quad ,0 \quad , -9.81) \quad . \tag{4.19}$$

4.4.7 Running simulation

Simulation has been let run for 1800 seconds for each of the cases studied, printing one time directory each 3 seconds. Fields are visualized through *paraView*, a graphical user interface for post-processing OpenFOAM cases. Figures 4.6 and 4.7 show the visualization of some representative time steps for velocity and temperature field time evolution inside the tank geometry. The displayed figures are to be intended as half of the real domain, due to the symmetric condition performed on the front face. The anabatic flow starts over the slope and detaches at the slope end as a warm ascending plume. The plume slowly circulates inside the tank perturbing the surrounding fluid. For the analysis of this thesis, the time range has been chosen in order to consider neglectable the boundary effects over the slope. The little transient structures along the slope that are observable in Figure 4.7 will be further investigated in Section 5.3.

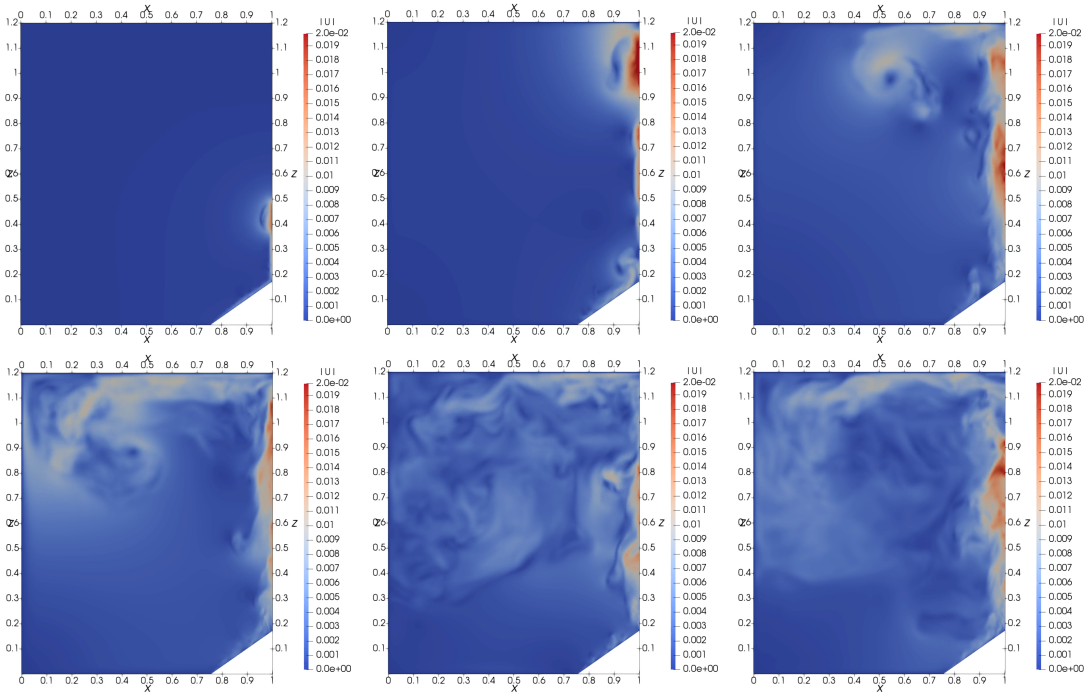

Figure 4.6: Velocity field visualization in the running simulation.

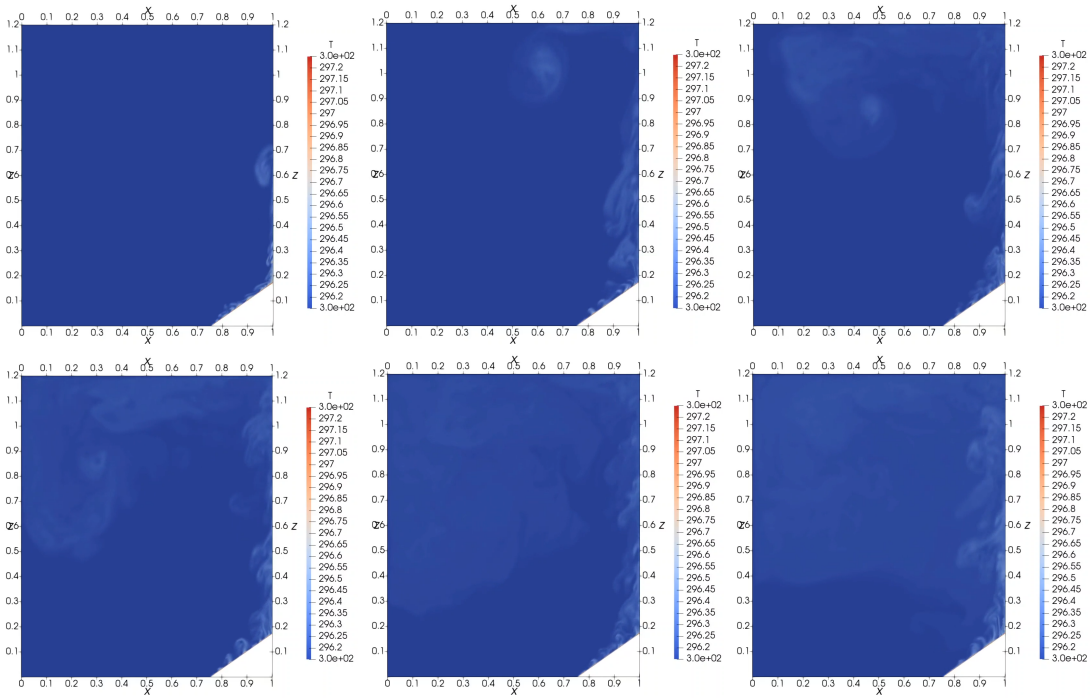

Figure 4.7: Temperature field visualization in the running simulation.

4.5 Probes time evolution

Velocity and temperature fields has been monitored in time during the simulation by the use of five rows of ten probes arranged along the slope in the normal direction as shown in Figure 4.8 (Table 4.5a and 4.5b).

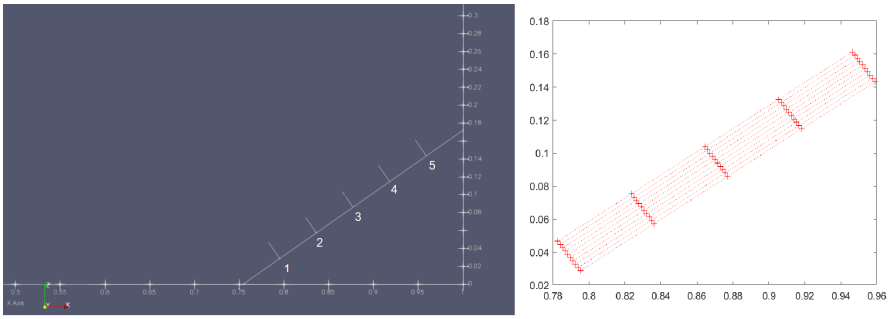

Figure 4.8: Probes arrangement along the slope.

Row	Distance (m)
1^{st}	0.05
2^{nd}	0.10
3^{rd}	0.15
4^{th}	0.20
5^{th}	0.25

(a) Distance of the rows of probes from the slope beginning.

Probe	Distance (m)
1^{th}	0.002
2^{th}	0.004
3^{th}	0.006
4^{th}	0.008
5^{th}	0.010
6^{th}	0.012
7^{th}	0.014
8^{th}	0.016
9^{th}	0.018
10^{th}	0.020

(b) Distance of the probes from the slope plain.

Table 4.5: Probes positions.

The time evolution of the along-slope velocity u, the normal-slope velocity w and the temperature T is showed in Figures 4.9,4.10 and 4.11 for the central line, monitored over a point chosen near the surface (second probe of the third row) and a point chosen far from it (eighth probe of the third row). A quasi-stationary behaviour has been recognized approximately in the time period spanning about 400-1000 s. After this period, a perturbation develops and is more visible in the along-slope velocity u near the slope (Figure 4.9(a) and (b)) and in the normal-slope velocity w far from the slope (Figure 4.10(a)).

For the following analysis, velocities and temperature has been firstly averaged in such time range (399-999 s) and then along the spanwise direction y. The range has been previously verified to be large enough to be at least equal to 5-6 times the characteristic time τ of the simulation, in order to be representative of the quasi-stationary oscillations of the turbulent fields.

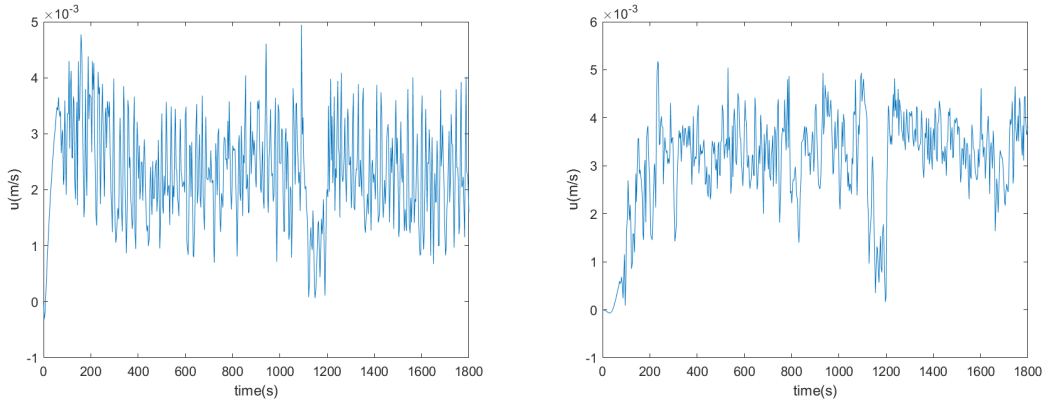

(a) (b)

Figure 4.9: Horizontal velocity (m/s) measured on (a) central line, second probe (0.004 m from the slope surface) and (b) central line, eighth probe (0.016 m from the slope surface) as a function of time (s).

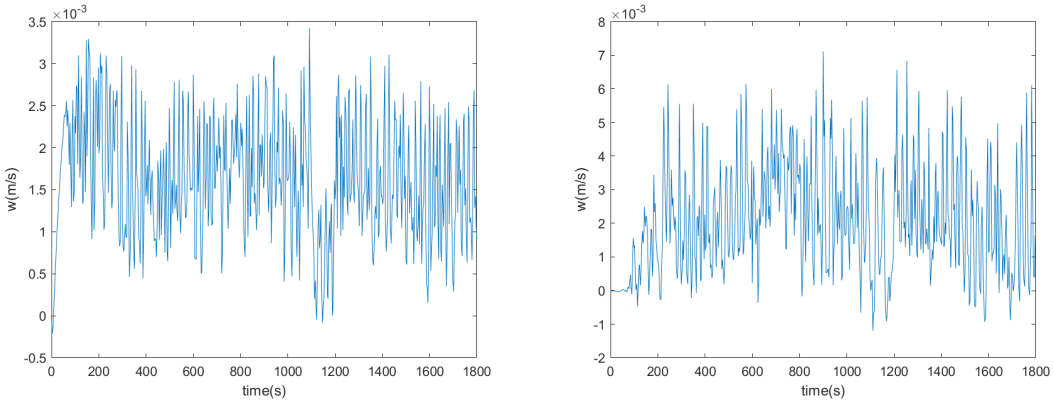

(a) (b)

Figure 4.10: Horizontal velocity (m/s) measured on (a) central line, second probe (0.004 m from the slope surface) and (b) central line, eighth probe (0.016 m from the slope surface) as a function of time (s).

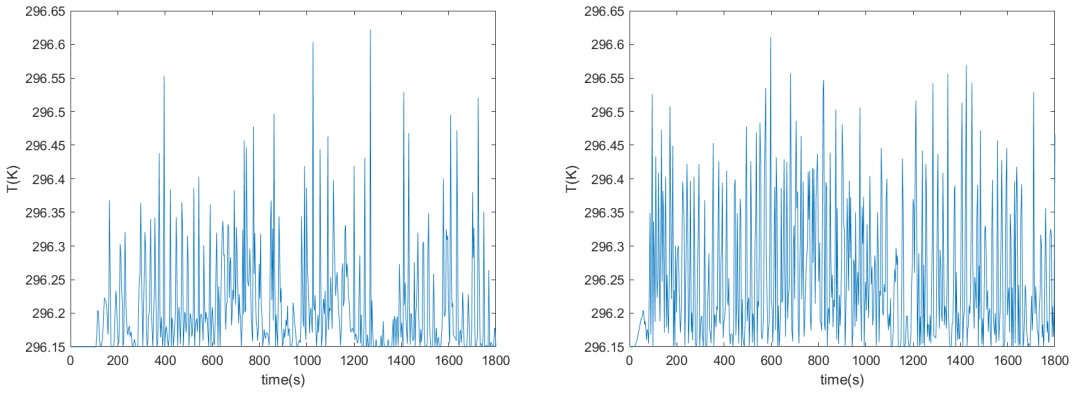

(a) (b)

Figure 4.11: Temperature (K) measured at (a) central line, second probe (0.004 m from the slope surface) and (b) central line, eighth probe (0.016 m from the slope surface) as a function of time (s).

4.6 Non-dimensional parameters and scaling

As discussed in Section 1.5, the non-dimensionalization procedure allows to characterize the dynamics with universal scales that do not depend upon the specific values of the problem. Non-dimensionalization can be beneficial if one is posed with similar physical situations, i.e. problems where the only changes are those of the basic dimensions of the system. The choice of the scaling quantity for the non-dimensionalization of a variable is arbitrary, but certain variables are better measured relative to some appropriate unit, intrinsic to the system, rather than a random unit of choice. If the scaling is adequate, a generic variable u/U_0 coming from different experiments, characterized by different conditions (such as a different ΔT specification, or a different geometry), will behave in the same manner, i.e. each of the different $u(z)$ profiles will collapse over the same curve. Thus the scaling choice is crucial to make a comparison between different datasets and to point out the general features.

4.6.1 Scaling

Velocity field is scaled as u/U_T, where U_T is the characteristic velocity defined in Section 4.4.1, based on fixed ΔT specification.

Temperature is scaled as $\frac{T-T_e}{\Delta T}$, where the temperature of the environment T_e is known in the case of the simulation, while for the experiment case T_e has been derived averaging the dataset over time and taking the minimum temperature value. Slope temperature T_s has been chosen taking the average of all the 5 probes positioned along the slope, as showed in Figure 4.12. From $T_s - T_e$, ΔT has been derived.

Table 4.6 summarizes values of temperature and velocity scales for both simulation and experiment. From here on, given a characteristic scale f_0, the notation used to indicate a scaled quantity f will be f/f_0, while the averaged quantities $\langle f \rangle$ and $\overline{f}$ will respectively the spanwise averaged f and the time averaged f. The scaled quantity averaged in time and subsequently in the spanwise direction will be indicated by $\frac{\langle \overline{f} \rangle}{f_0}$. The scaled fluctuation of such quantity will be $\frac{\langle \overline{f'} \rangle}{f_0}$, so that the scaled flux of f will be $\frac{\langle \overline{u'_j f} \rangle}{u_0 f_0}$.

4.6.2 Boundary Layer thickness estimation

In the work of Fedorovich and Shapiro discussed in Section 3.2.1, from the analysis of slope-normal profiles (Figure 4.13), depth of dynamic and thermal boundary layer has been estimated as the height at which transition occurs between

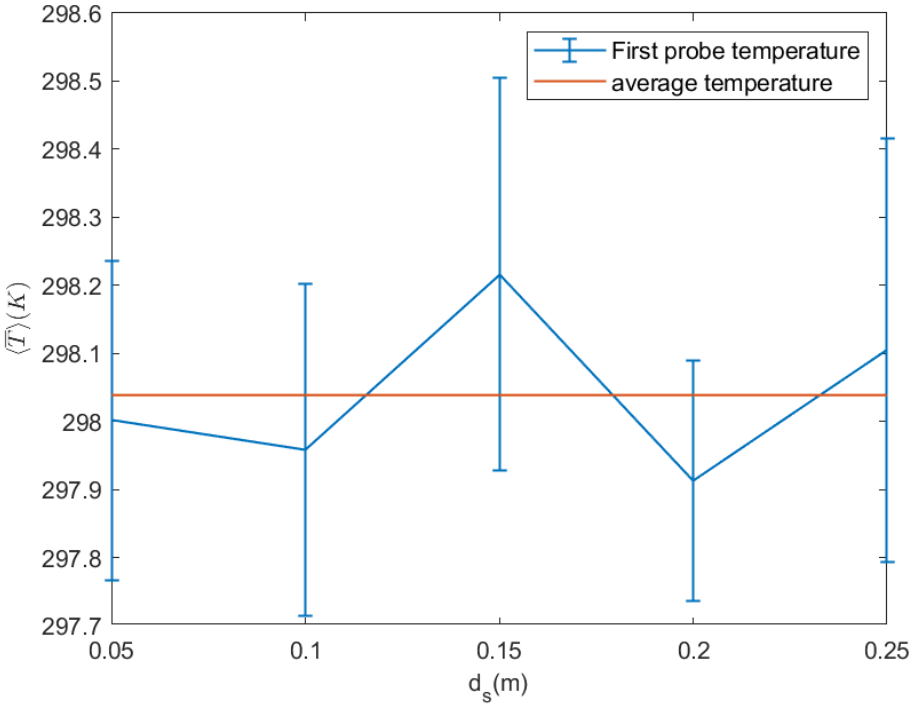

Figure 4.12: Temperature values and rms measured on the first probe of each row (blue color) plotted together with the average value (red color) as a function of the probe distance from the slope beginning d_s.

Scaling values		
	Simulation	Liberzon experiment
ΔT	1.1°C	1.49°C
T_e	23°C	23.752°C
U_T	0.0261 m/s	0.0303 m/s

Table 4.6: Scales used for normalization of temperature and velocity.

positive and negative buoyancy (for the thermal boundary layer, hereafter called TBL) and between upslope and downslope velocity (for the dynamical boundary layer, hereafter called DBL). The reference system adopted is depicted in Figure 4.14 and joint with the slope geometry.

The estimation of the height of the dynamic boundary layer, in Fedorovich's work, is based on the presence of a region of return flux developed in the stably stratified background atmosphere. This region is not present in the non-stratified simulation of this work, in which velocities and temperatures decrease in the whole slope boundary layer, without changing sign. For this reason, a different criteria of estimation has been chosen.

From Figure 4.15a, a snapshot of the spatial distribution of instantaneous along-slope velocity over a $y - z$ cross-section is showed.

In the bottom half of the section, a regular pattern of strong positive values

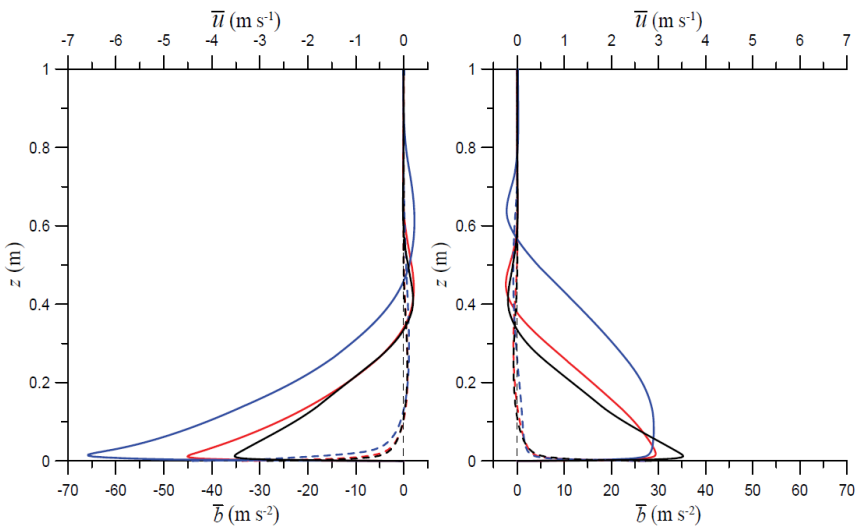

Figure 4.13: Figure from Fedorovich and Shapiro (2009). Mean along-slope velocity (u, solid lines) and buoyancy (b, dashed lines) profiles in the katabatic (left) and anabatic (right) flows with surface buoyancy flux $|Bs| = 0.5$ m^{2}s^{-3}, kinematic density $\nu = 10^{-4}$ m^{2}s^{-1}, and Brunt-Vaisala frequency N = 1 s^{-1} for three different slope angles: 30° (blue lines), 60° (red lines), and 90° (black lines).

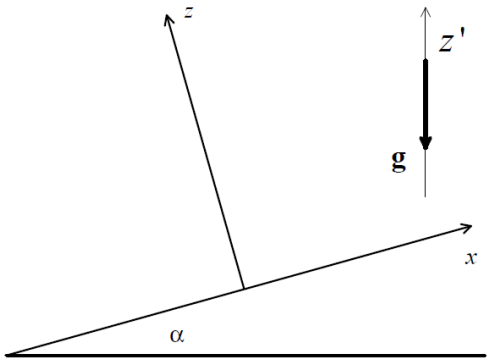

Figure 4.14: Slope-coordinate reference system.

appears in a thin region near the slope which is followed along the vertical axis by a region of uniformly weak velocity field.

Averaging the velocity along the spanwise direction, figure 4.15b is obtained. In such situation, the transition between the two aforementioned region is more clear. Note that, in both sections, above 0.3 m begins a region of strong velocity increase. This region is not representative of the dynamic above the slope because it include the rebounds of the plume interacting with the ceiling.

The profile over the normal-slope axis is showed in figure 4.16 for the first 60 cm above the central line. The region of rebound described for the cross-section is also confirmed here. The height at which the transition occurs is approximately at $L = 0.06$ m. This height has been chosen to be an analogous of the DBL's height

and will be used for scaling the height coordinate in the following analysis as z/L.

Figure 4.17 shows the y-averaged temperature field. It is notable that the temperature rapidly decreases to background value in the firsts 0.007 m from the slope, followed first by a more weak decrease and then by a second rapid assestment to the background value. The rebound region is visible in the last part of the profile. Thus if we assume this value as an estimation of the TBL's height, the TBL layer results shallower than the corresponding DBL layer, as in Fedorovich's work.

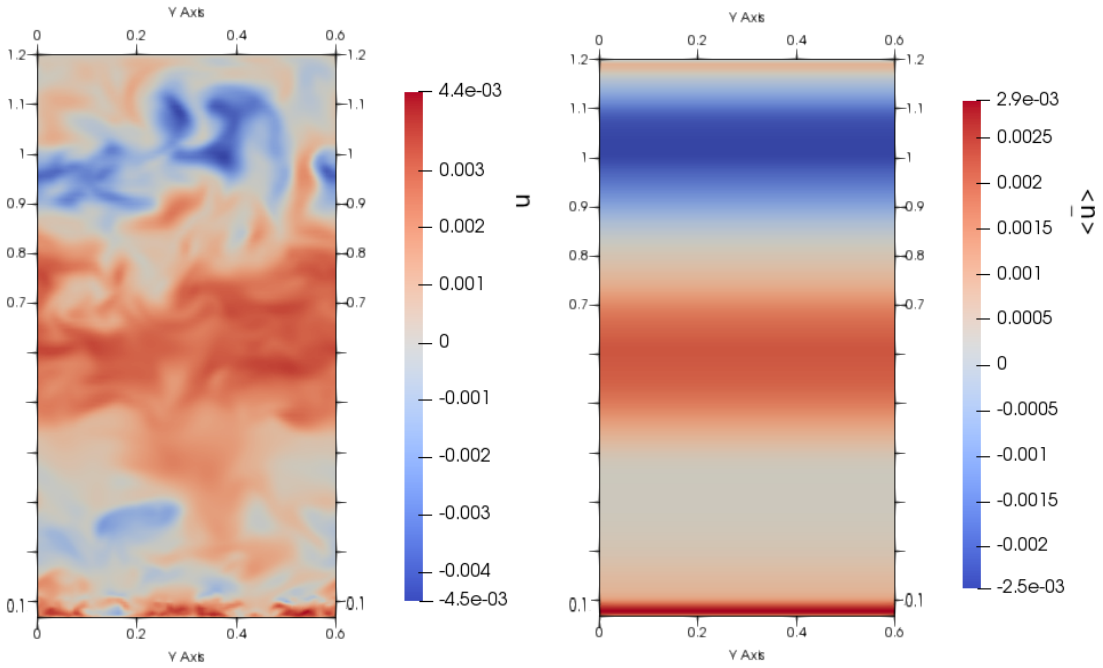

(a) (b)

Figure 4.15: Cross section along the $y - z$ plane, over the center of the slope, of instantaneous horizontal velocity spatial distribution (a) and average velocity spatial distribution (b).

4.6.3 Comparison between datasets

The results of the simulation LES1.10 (see Table 4.4) is validated against three datasets present in literature and coming from: Prandtl linear model discussed in Section 3.1.2, Fedorovich (2009) DNS simulation discussed in 3.2.1 and Liberzon experiment (not yet published) discussed in Section 4.2.1. Liberzon's dataset is chosen because the simulation geometry is based on it, and this facilitates a direct comparison. An analysis of the literature revealed that there is no previous work in literature regarding turbulent anabatic flows in neutral stratification, and a general lack of theoretical models able to describe them. On this basis, the Prandtl model and Fedorovich's DNS dataset are chosen in order to have a theoretical and numerical comparison, even though they both assume a stable stratification and

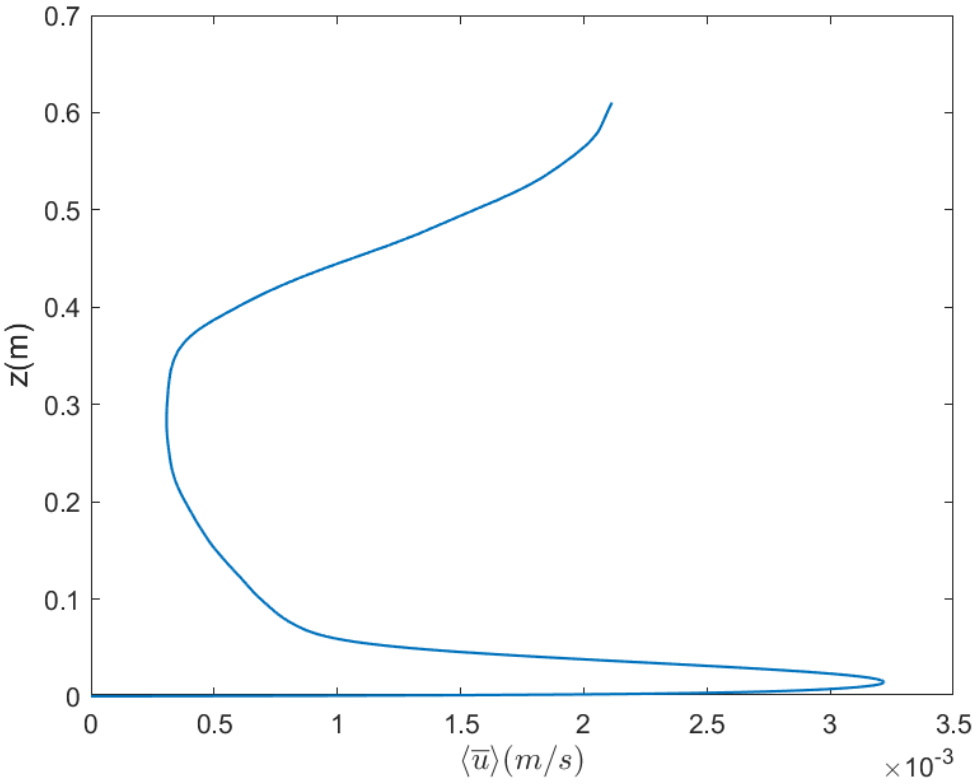

Figure 4.16: Averaged horizontal velocity profile for the first 60 cm above the slope along the central line.

an infinite slope extension. For these reasons, a perfect matching is not expected, but rather a general correspondence about the physics involved.

In the following subsections, each of the three datasets will be discussed in detail.

4.6.3.1 Prandtl solutions

Prandtl model assumes Pr=1, in the case of stationary laminar flow parallel to the slope. Introducing the generic scales used by Fedorovich (2009 L, V, B for length, velocity and buoyancy, the non-dimensional set of equations from the Prandtl model are:

$$b_n + \frac{vV}{L^2 \sin\alpha B} \frac{\partial^2 u_n}{\partial^2 z_n} = 0 \quad , \tag{4.20}$$

$$- u_n + \frac{vB}{L^2 \sin\alpha N^2 V} \frac{\partial^2 b_n}{\partial^2 z_n} = 0 \quad , \tag{4.21}$$

Being ν,N,B_s and α the governing parameters of the problem, each one of the the adimensional scales L, V, B can be completely expressed in terms of these 4 parameters. Simplification of the equation system is obtained by Fedorovich using

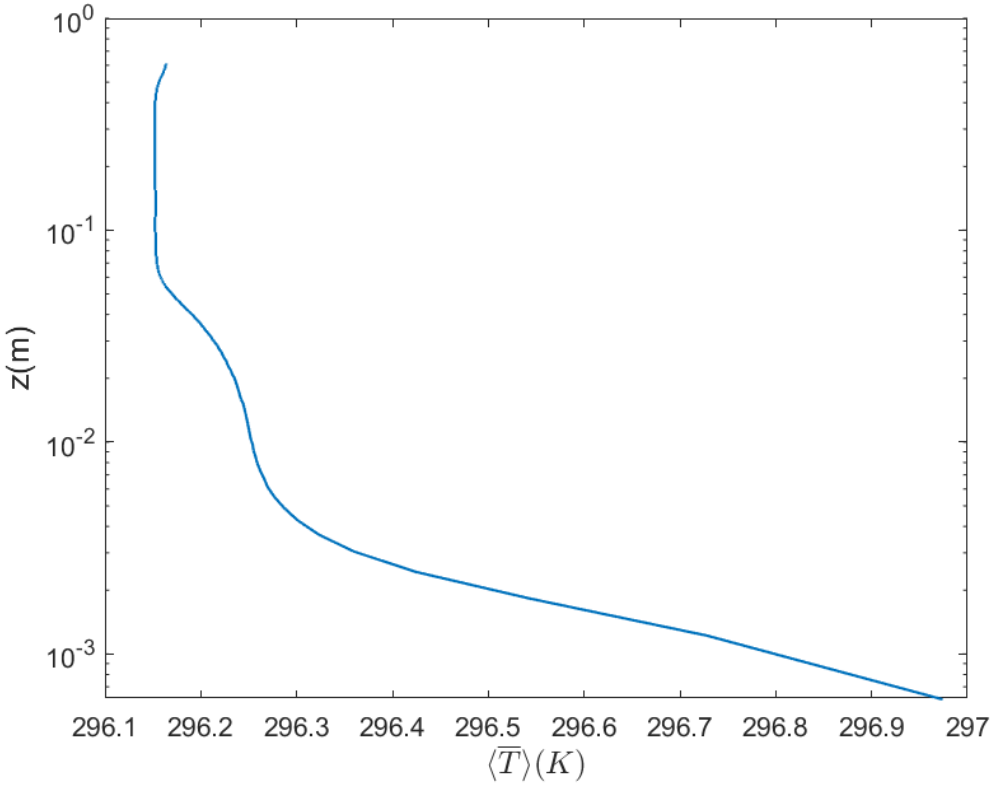

Figure 4.17: Logarithmic scale for averaged temperature profile of the first 60 cm above the slope along the central line.

the following representation: $L = \nu^{\frac{1}{2}} N^{\frac{-1}{2}} B_s^{-1} \sin^{\frac{-1}{2}} \alpha$, $V = \nu^{\frac{-1}{2}} N^{\frac{3}{2}} B_s^{-1} \sin^{\frac{-1}{2}} \alpha$, $B = \nu^{\frac{-1}{2}} N^{\frac{-1}{2}} B_s \sin^{\frac{-1}{2}} \alpha$ in order to have:

$$b_n + \partial_{z_n}^2 u_n = 0 \quad , \tag{4.22}$$

$$- u_n + \partial_{z_n}^2 b_n = 0 \quad , \tag{4.23}$$

which can be analytically solved giving:

$$u_n = \sqrt{2} \sin\left(\frac{z_n}{\sqrt{2}}\right) e^{-\frac{z_n}{\sqrt{2}}} \quad , \tag{4.24}$$

$$b_n = \sqrt{2} \cos\left(\frac{z_n}{\sqrt{2}}\right) e^{-\frac{z_n}{\sqrt{2}}} \quad . \tag{4.25}$$

Solutions are shown in Figure 4.18.

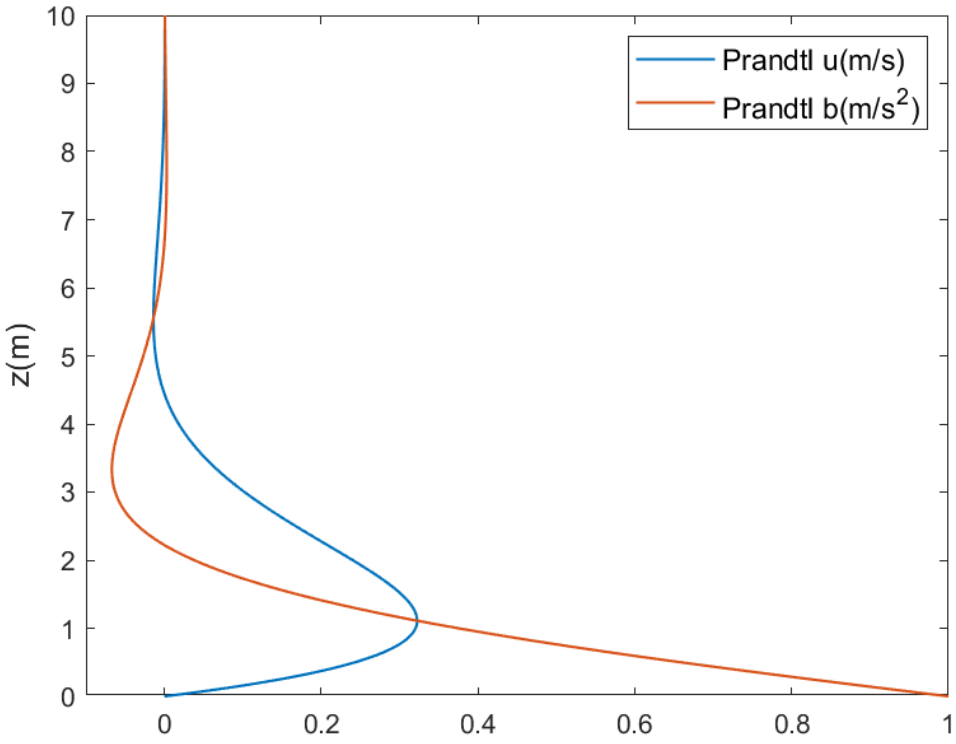

Figure 4.18: Prandtl model solutions for upslope velocity and buoyancy.

From the scaling method chosen in this work and discussed in the previous section, the length scale Lp has been chosen for the Prandtl profiles at $Lp = 5$.

4.6.3.2 Fedorovich data

Fedorovich's DNS (2009) has been already discussed in Section 3.2.1. The equations solved in the simulation were the (4.26), (4.27) and (4.28), which are reported here for convenience:

$$\overline{b} sin\alpha + \nu \partial_z^2 \overline{u} - \partial_z \overline{u'w'} \quad , \tag{4.26}$$

$$- N^2 \overline{u} sin\alpha + \nu \partial_z^2 \overline{b} - \partial_z \overline{b'w'} \quad , \tag{4.27}$$

$$- d_z \overline{\pi} + \overline{b} cos\alpha - \partial_z \overline{w'w'} = 0 \quad , \tag{4.28}$$

with boundary conditions $\overline{u} = 0$, $-\nu d_z \overline{b} = B_s$ at $z = 0$, and $\overline{u} = 0$, $\overline{b} = 0$ at $z \to \infty$. As discussed in section 3.2.1, Fedorovich showed that the volume flux defined by the integral length scales L_I and V_I is $V_I L_I = \frac{B_s}{N^2 \sin\alpha}$, so that flows characterized by different values of the governing parameters share the same value of volume flux, and consequently the same integral slope-flow's Reynolds number

$Re_I = \frac{|V_I L_I|}{\nu} = \frac{|B_s|}{\nu N^2 \sin\alpha} = \frac{|Fp_b|}{\sin\alpha}$. The Re_I number that will be used for comparison with this work is the maximum value considered in the article (10^4) using the fixed combination $B_s = 0.5m^2s^{-3}$, $N = 1s^{-1}$, $\nu = 10^4 m^2 s^{-1}$, $\alpha = 30°$.

From the profiles obtained in such conditions (Figure 4.19), length scale has been chosen as $L_f = 0.6$.

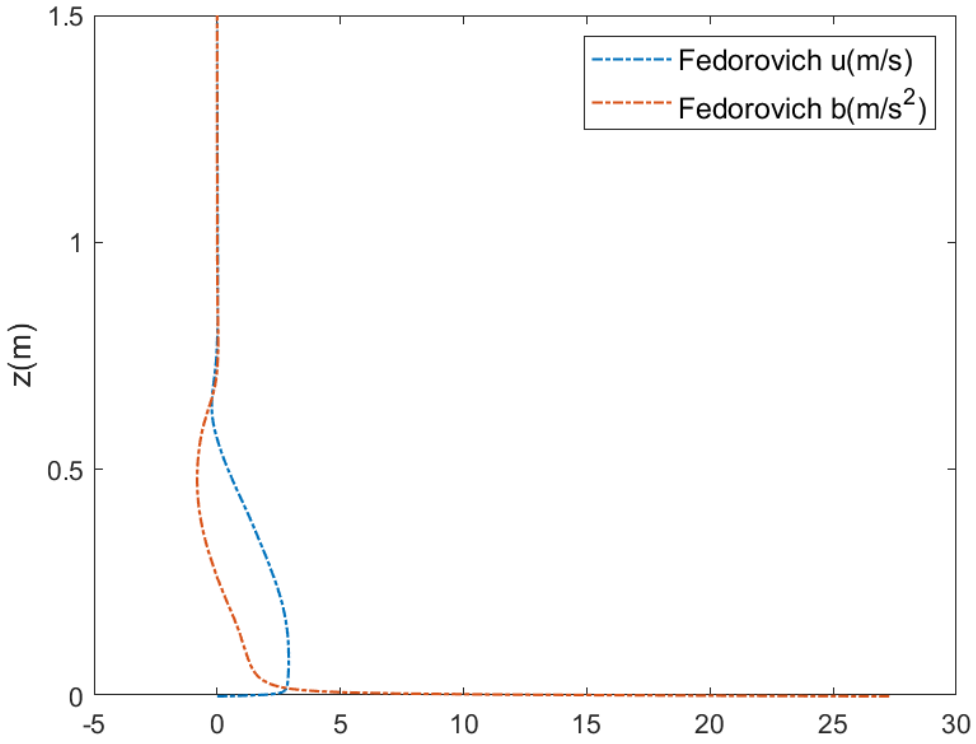

Figure 4.19: Original Fedorovich data for $B_s = 0.5m^2s^{-3}$, $N = 1s^{-}1$, $\nu = 10^4 m^2 s^{-1}$, $\alpha = 30°$

In the case of Fedorovich data, buoyancy has been adimensionalized by a factor $B = b_s$ in which appears the buoyancy surface value b_s. Velocity scale has been then derived as $U_b = \sqrt{b_s L_f}$. This is equivalent to the other cases of temperature normalization because one obtains again $b_n = \frac{b}{b_s} = \frac{g\beta(T-T_e)}{g\beta(T_s-T_e)}$.

4.6.3.3 Liberzon data

Liberzon's experiment shares the same geometrical characteristics of the simulation performed in this work. Configuration and measurement methods are specified in Section 4.2.1. Velocity data are measured over a 2-d grid in a small region over the slope as shows Figure 4.20 in which horizontal and vertical velocities data of the whole region detected by the particle image velocimetry are plotted as a function of x and z. Each gridpoint is colored by the velocity component value; zero values in

the figure corresponds to the slope obstacle, while the blue area shows the anabatic flow development above it.

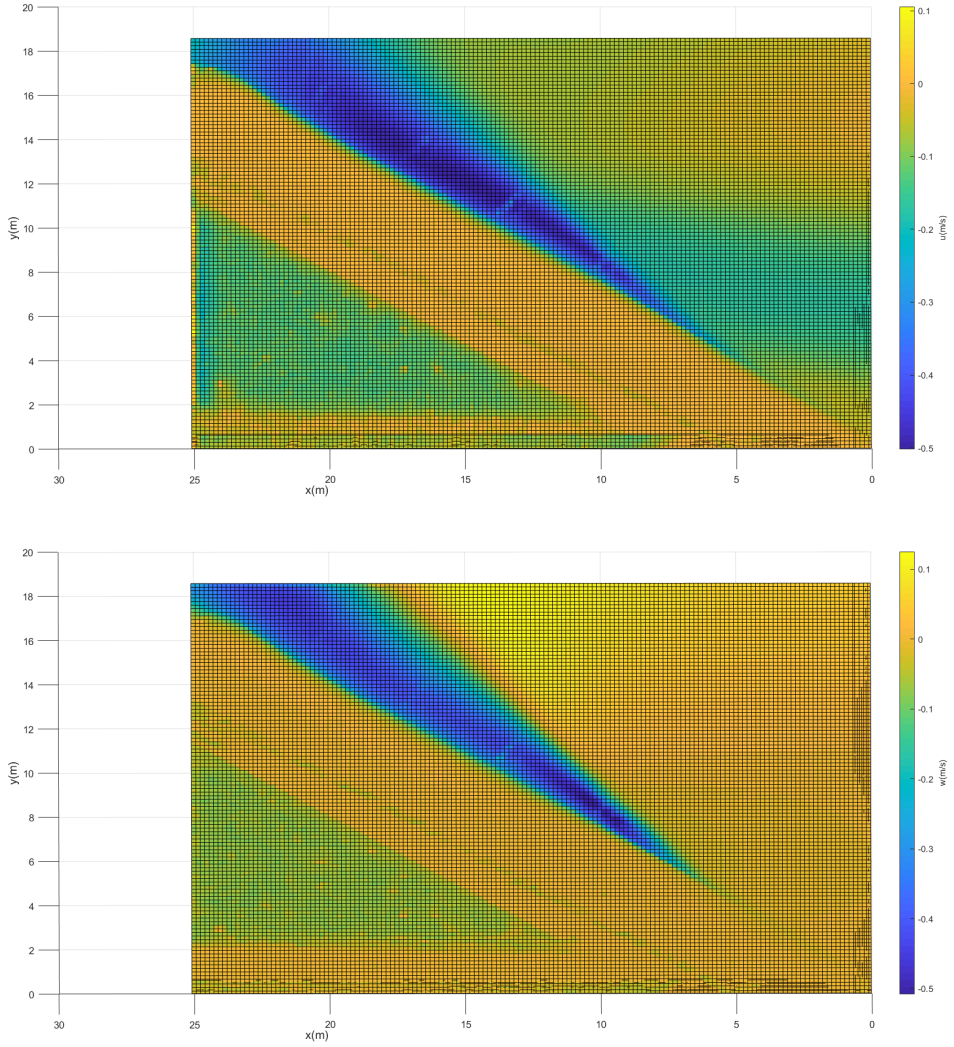

Figure 4.20: Liberzon horizontal velocity u and vertical velocity w data visualization over the grid.

Length scale for Liberzon and LES1.10 datasets has been estimated from their profiles. The Figure 4.21 show them plotted togheter over the central line along the slope. It can be seen that the criteria of choice described in Section 4.6.2 is satisfied for $L_l = 0.07$ m in Liberzon profile case and $L_s = 0.06$ m in LES1.10 case.

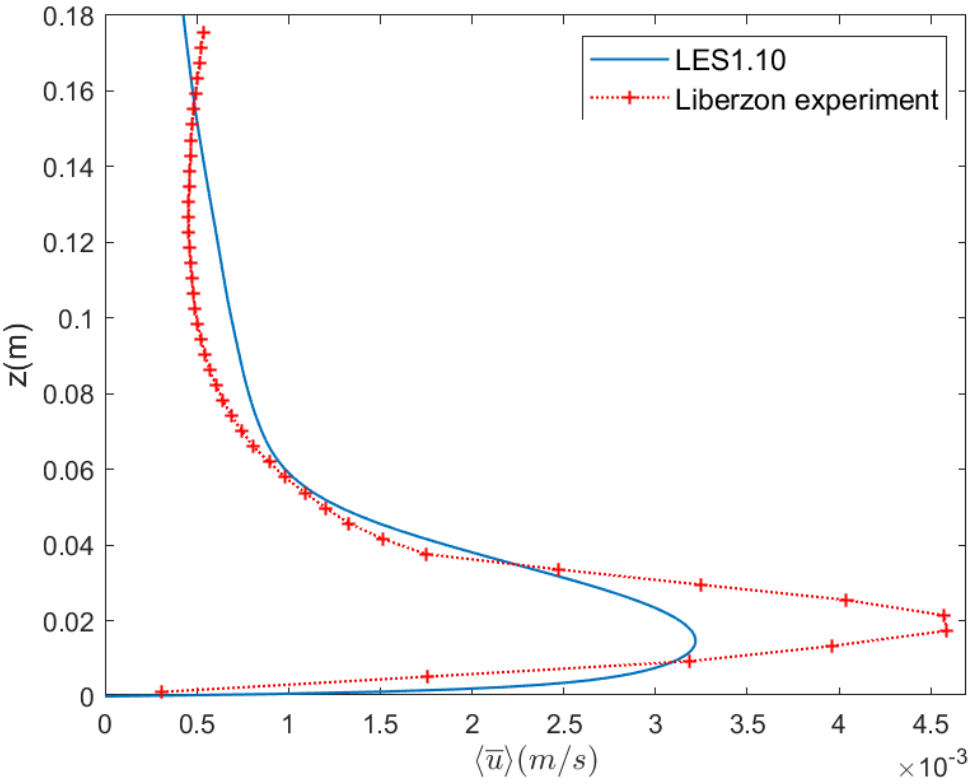

Figure 4.21: Comparison between horizontal velocity of LES1.10 and Liberzon data along the central line above the slope.

The Table 4.7 summarizes the scales used for each of the cases described (Prandtl solutions are already in normalized form of u_n and b_n).

Length scale	Velocity scale	Temperature scale
$L_p = 5$	–	–
$L_f = 0.6$	$U_f = 4.0453$	$B = 27.27$
$L_s = 0.06$	$U_s = 0.0114$	$T_e = 296.15, \Delta T = 1.1$
$L_l = 0.07$	$U_l = 0.0123$	$T_e = 296.902, \Delta T = 1.48$

Table 4.7: Scales used for normalization.

4.7 LES1.10 validation

The validation of the LES1.10 is here presented against the Prandtl model dataset, the Fedorovich's dataset and the Liberzon's dataset.

Figure 4.22 shows, for each of the four cases investigated, normalized horizontal velocity and temperature profiles measured, in the case of LES1.10 and Liberzon's data, over the central line of the slope. Scaling is done with the criteria of Table 4.7.

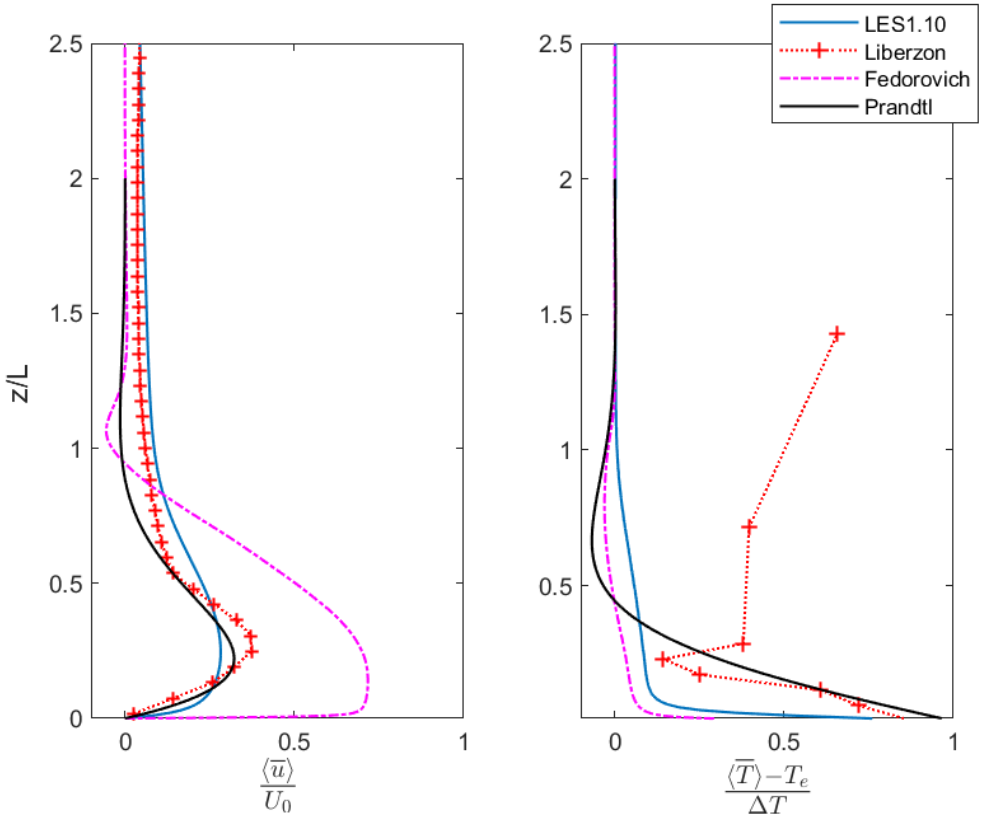

Figure 4.22: Comparison between each of the four cases involved for normalized horizontal velocity $\langle\overline{u}\rangle/U$ (a) and normalized temperature difference $\frac{\langle\overline{T}\rangle - T_e}{\Delta T}$ (b).

From Figure 4.22(a), it can be noted that each of the 4 profiles shares the presence of a near-slope peak's region, a decreasing velocity region and a stabilization around a fixed value. For both Prandtl and Fedorovich datasets this value is zero, such as expected from a stable stratification assumption. A region of negative velocities is present at about $z/L = 1$, this difference is also expected because of the stable stratification, while in the thermal convection generated inside a neutral background, velocities and temperatures are expected to decrease monotonically.

Fedorovich profile differs the most from the others in term of intensity of the peak region and the smoothness of this area. The higher intensity can be explained considering that turbulence may be much more developed on the infinite plane

assumption, while for the LES1.10 and Liberzon's experiment, the finite plane does not permit the total turbulence development. This can be confirmed also considering the profiles in Section 5.5 which will show a gradual enhanchement of the peak's value and turbulence as the flux travels above the slope length. The more extended region of the peak in Fedorovich dataset is also explainable by a stronger turbulence diffusion. Differences between Fedorovich datasets and Prandtl solutions are most visible in the temperature profiles and are expected because of the laminar and steadyness assumptions. Despite this, as Fedorovich obtained from his work, this simple model keeps many features that can be recognized in the more complex ones. Maximum value for velocity is expected to be found at $z_{nmax} = \pi\sqrt{2}/4$ and Fedorovich observed that this height keeps independence from the Reynolds number. The height at which maximum is expected from the Prandtl model is conserved in the other cases too. Velocity profiles of simulation and Liberzon data are in good agreement, and it is notable that integrating the two curves gives approximately the same value, while the differences can be explained in terms of more mixing involved in the LES1.10.

Temperature profiles in figure 4.22(b) shows a typical shape for all the 3 profiles characterized by a strong decreasing in a thin near-surface layer, a negative value above this region followed by a quasi-linear tendency to a zero-value. Liberzon's data shows more similarity to the Prandtl laminar solution compared to the other profiles, except for the last 3 data points which are completely out of range and do not seems to be reliable. This similarity could mean a less developed turbulence in the experiment's flow. Simulation is not in good agreement with Liberzon's data, but a strong agreement is found with Fedorovich's fully turbulent DNS.

Figure 4.23 shows the same graph in logarithmic scale, and points out more clearly the agreement between Liberzon and Prandtl.

4.7.1 Velocity and temperature profiles along the slope

In this Section will be considered comparisons between LES1.10 and Liberzon's data over the other rows along the slope, aside from the central one already discussed. Comparison is not significant with Fedorovich and Prandtl datasets because of the infinite slope's length assumption.

Discordance between the two datasets in Figures 5.5 is progressively attenuated along the slope, being highest at the slope beginning. In particular, Liberzon's experiment shows a secondary maxima in the upper region of the first profile, around $z/H = 0.9$, that begins to mitigate in the second profile and become absent in the following profiles. This indicates a perturbation that originates at the beginning of the slope and is not part of the upflow dynamic. Since datasets has been taken for

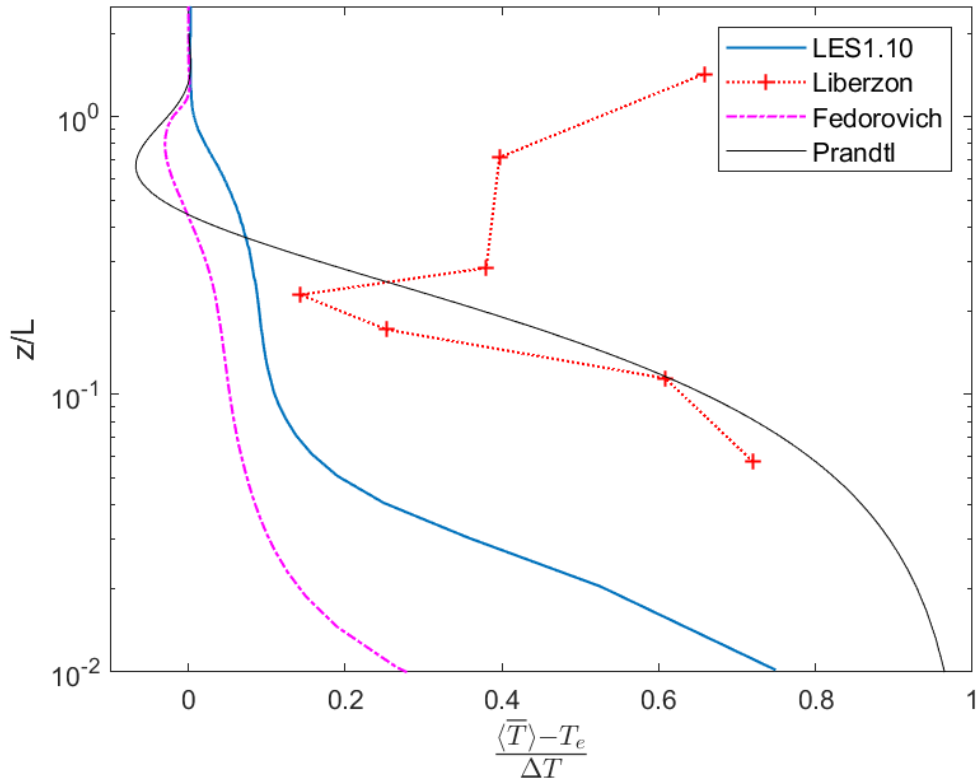

Figure 4.23: Comparison of normalized temperature differences $\frac{\langle\overline{T}\rangle - T_e}{\Delta T}$ in logaritmic scale.

9000 time steps at a frequence of 5Hz in the experiment case (for a total of 1800 seconds), the field measured probably contains developed perturbations coming from boundary effects, altering the original flow dynamic.

Simulation's profiles transport upward more momentum at the end of the slope with respect to the beginning, smoothing the vertical velocity gradient. It may be due to the fact that the end of the slope is the region in which the plume generates and turbulence is enhanced.

Temperature profiles of figure 4.25 are comparable with simulation's profiles in the monotonically decreasing inside the firsts cm of the boundary layer, and the much higher thermal boundary layer of Liberzon experiment suggests again a laminar behaviour, but no information can be assessed above this region. As a final remark, it is possible to affirm that the LES1.10 verifies all the features of a turbulent anabatic flux. For this reason, validation can be considered satisfactory.

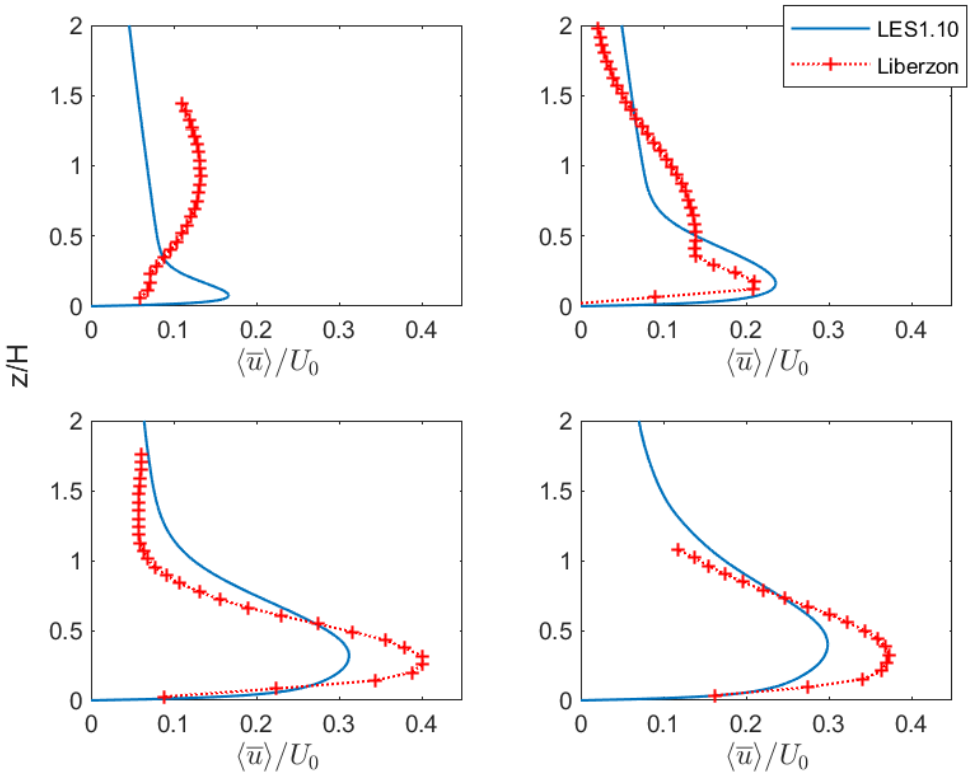

Figure 4.24: Scaled horizontal velocity $\langle\overline{u}\rangle/U$ profiles comparison between simulation and Liberzon data along the 1st, 2nd, 4th and 5th row.

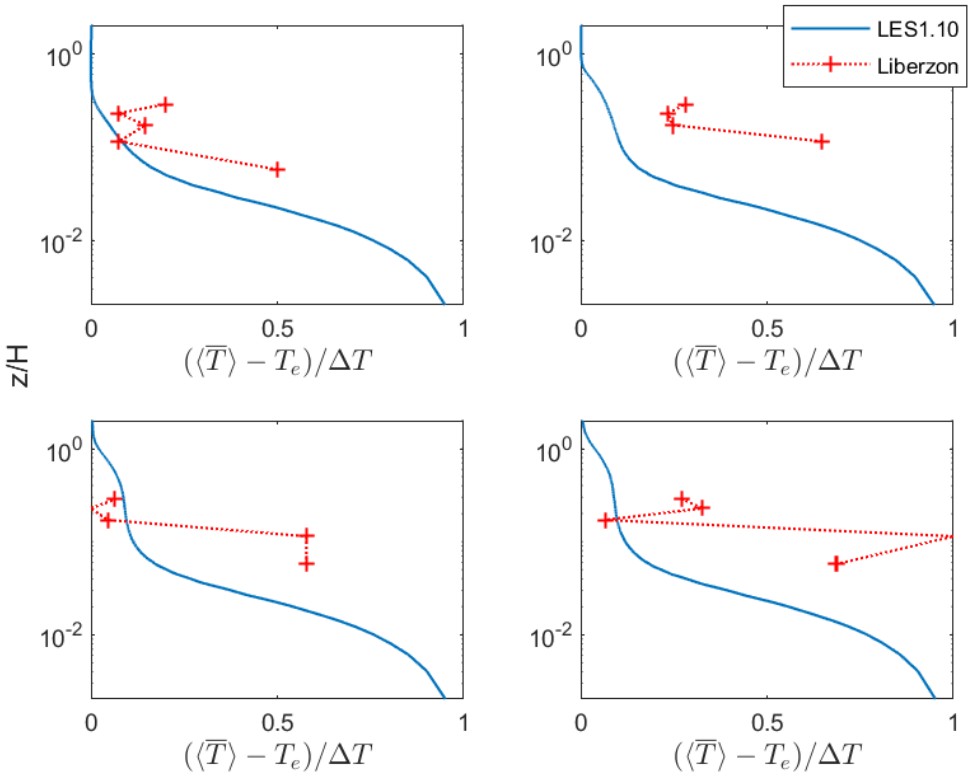

Figure 4.25: Scaled temperature difference $\frac{\langle\overline{T}\rangle - T_e}{\Delta T}$ profiles comparison between simulation and Liberzon data along the 1^{st}, 2^{nd}, 4^{th} and 5^{th} row.

Chapter 5

Results and discussion

5.1 Alternative length scale definition

In the comparison with Fedorovich and Shapiro work, it has been used a method of scaling analogous to the one used in their article, taking into account that they were dealing with a stably stratified background atmosphere. In order to find a parametrization suitable to the neutral stratification, independent from the Brunt-Vaisala frequency N, two approaches are considered. The first one accounting for the height of the slope H, the second one using the thermal diffusivity D to define a thermodynamic length scale able to estimate the thermal boundary layer depth. Each approach is evaluated over the three simulations defined in Section 2.4.2. Table 5.1 summarize the ΔT for each of the three cases.

Scaling parameters	
	ΔT
LES1.10	1.1
LES2.78	2.78
Liberzon	1.49

Table 5.1: Temperature differences for the cases analyzed.

Original non-scaled profiles for the three cases are showed in figure 5.1 for the firsts 0.6m from the slope. Note that, in such profiles, is included the rebound region described in Section 4.6.2 above 0.3m. A more in-depth analysis of the log temperature profile will be done in Section 5.1.2.

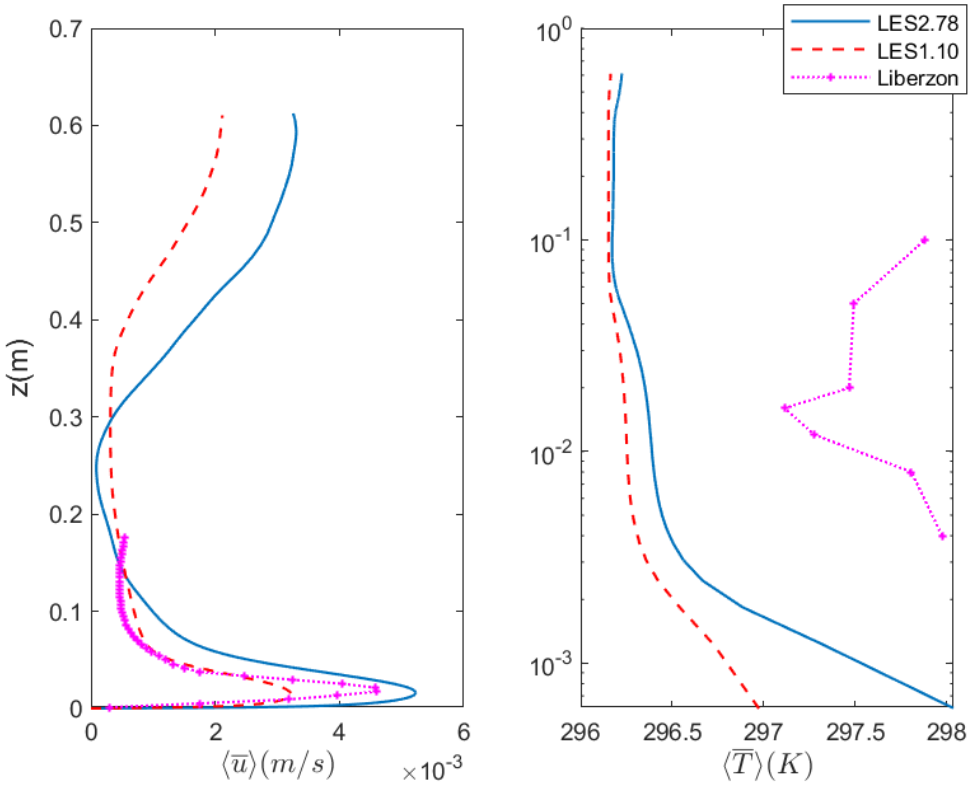

Figure 5.1: Original profiles of velocity and temperature for the 3 cases.

5.1.1 Scaling with the slope height

The characteristic length, velocity and time that are obtained from the slope length Ls and the temperature difference, reads:

$$L_0 = H = L_s \sin\alpha \quad , \tag{5.1}$$

$$U_0 = \sqrt{g\beta\Delta T L_0} \quad , \tag{5.2}$$

$$t_0 = \frac{L_0}{U_0} = \sqrt{\frac{L_s \sin\alpha}{g\beta\Delta T}} \quad . \tag{5.3}$$

Where the characteristic length L_0 is the slope height, and U_0 is the buoyant velocity. Table 5.2 summarised the value of such parameters in the three cases under consideration.

Scaling parameters			
	L_0	U_0	t_0
LES1.10	0.1721	0.0193	8.9292
LES2.78	0.1721	0.0306	5.6167
Liberzon	0.1721	0.0224	7.6721

Table 5.2: Length, velocity and time scale estimated for the experiment and the two simulations.

Figure 5.2 shows the non-dimensional temperature and the streamwise velocity scaled with L_0 and U_0 along a slope-normal line at the center of the slope. Near the slope, the profiles of the two simulations collaps one each other, while the experimental profile exhibits a larger velocity peak. The thickness of the surface DBL is more similar between the three profiles.The simulation temperature profiles are close, and is notable the presence of an intersection point between the LES1.10 and LES2.78 profile, according to which LES1.10 is warmer than LES2.78 in the near-surface layer and cooler than LES2.78 in the layer above $\frac{z}{L_0} = 0.3$. As already noted in Section 4.7, Liberzon temperature profile appears out of range and does not seems trustworthy.

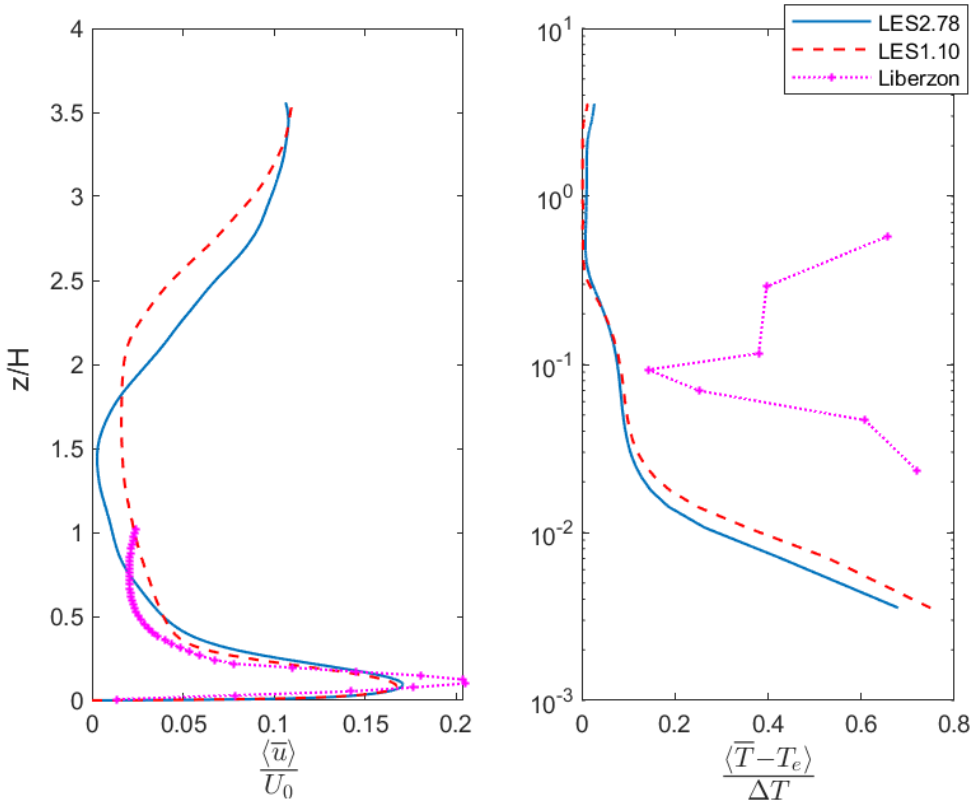

Figure 5.2: Horizontal velocity and temperature difference scaled with slope height H: Normalized horizontal velocity is $\langle \overline{u} \rangle / U_0$, normalized temperature difference is $\frac{\langle \overline{T} \rangle - T_e}{\Delta T}$.

5.1.2 Scaling with the thermal boundary layer height

In Section 4.6.2, the height of the thermal boundary layer is empirically estimated from the temperature profiles as that height separating a region of rapid decrease of temperature from a region of more weak approaching to the background temperature.

The depth of the thermal boundary layer will be now estimated by the diffusion length parameter l_0 related to the characteristic time at which temperature diffuses in the atmosphere over the slope (Cintolesi, Petronio, and Armenio, 2015):

$$l_0 = 2\sqrt{Dt_0} = 2\left(\frac{D^2 L_s \sin\alpha}{g\beta\Delta T}\right)^{(1/4)} \tag{5.4}$$

Table 5.3 shows the values of l_0 for each case, along with the empirical estimation l_0^{emp} made in Section 4.6.2. For the two simulations, the two quantities exhibit the same order of magnitude of the old estimation. Liberzon's new length scale shows a discrepance in the two values, but this is not significant since the estimation of l_0^{emp} for the experiment has been done over a temperature profile of only ten points.

Further comparison of the empirical l_0^{emp} and computed l_0 estimation of the

Thermal boundary layer height		
	l_0^{emp}	l_0
LES1.10	0.0079	0.0024
LES2.78	0.0079	0.0019
Liberzon	0.016	0.0022

Table 5.3: Comparison between empirical estimation of the thermal boundary layer height l_0^{emp} with the characteristic temperature length l_0 defined in equation (5.4).

thermal boundary layer can be done looking to the termal profile in logarithmic scale reported in Figure 5.3. For both LES1.10 and LES 2.78 it is possible to recognize the thin layer close to the slope surface, where temperature experiences an exponential drop. This layer depth extends approximately 0.004 m from the surface. Above this height, temperature has a less marked reduction till a point of transition at $z = 0.06$ m, where the environmental temperature is reached. Around $z = 0.3$ m, temperature is perturbed by the flow coming form the upper par of the domain. The quantity l_0 seems therefore to be representative of the thin layer containing most of the temperature decrease, thus being a good estimation of the thermal boundary layer depth.

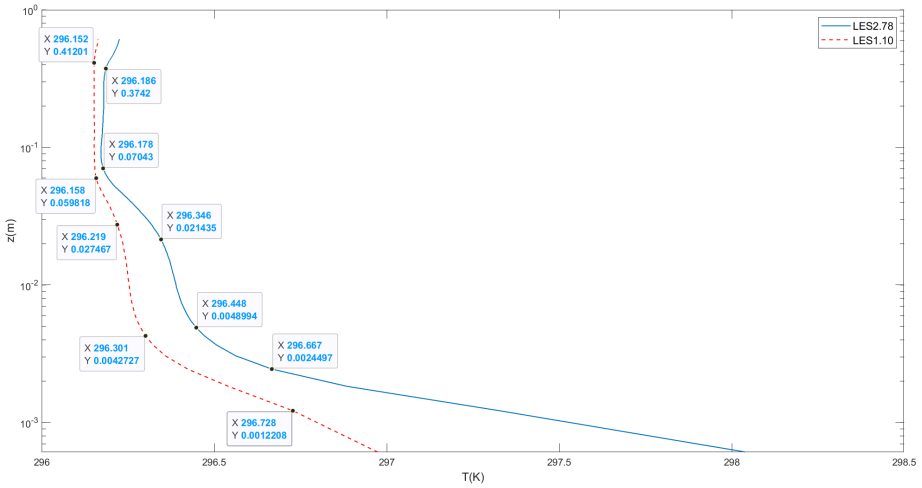

Figure 5.3: Temperature profiles of the two simulations and reference points over the curves.

The parameter l_0 is tested as a length scale, and is adopted to define a new velocity scale as follows:

$$u_0 = \sqrt{g\beta\Delta T l_0} \quad . \tag{5.5}$$

Table 5.4 reports the values of the characteristic velocity based on l_0.

Figure 5.4 shows the scaled profiles limited to the firsts 0.24 m.

Scaling parameters		
	l_0	u_0
LES1.10	0.0024	0.0023
LES2.78	0.0019	0.0032
Liberzon	0.0022	0.0026

Table 5.4: length scale and velocity scales.

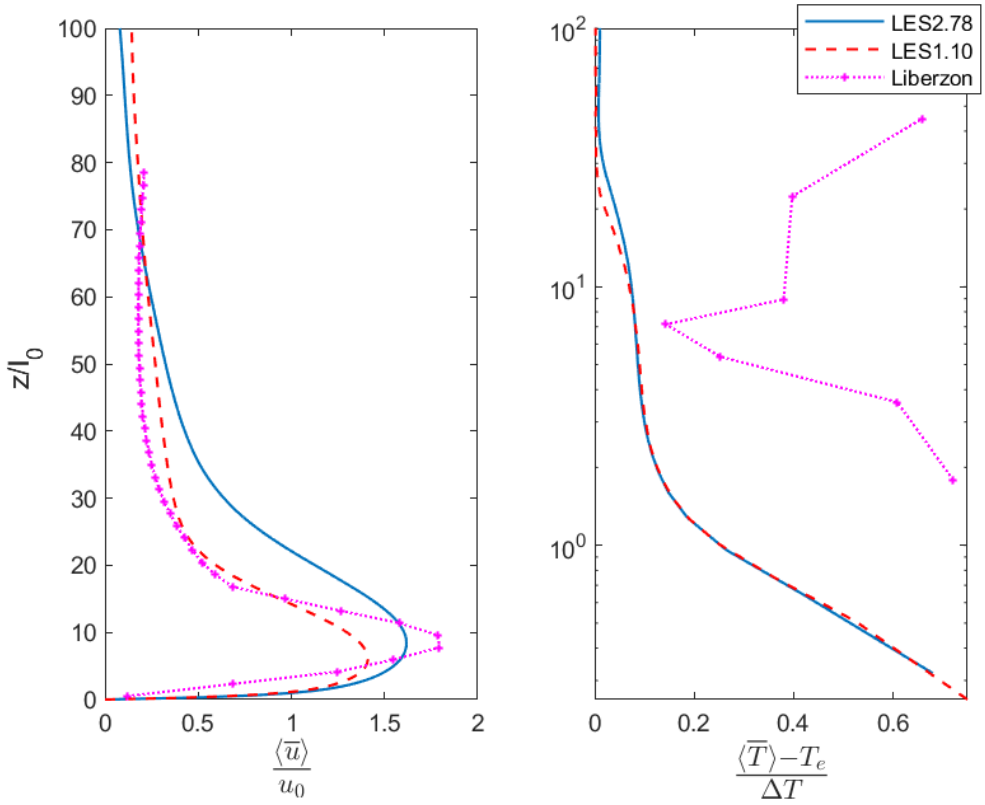

Figure 5.4: Scaled profiles with diffusion length l_0. Normalized horizontal velocity is $\langle\overline{u}\rangle/u_0$, normalized Temperature difference is $\frac{\langle\overline{T}\rangle - T_e}{\Delta T}$.

Comparing the horizontal velocity in Figure 5.4 and 5.1, the velocity peaks of the simulations still underestimate the experimental one. The simulation LES2.78, setted up with a larger difference of temperature, shows high velocity values farther to the slope (up to $z/l_0 \simeq 35$) with respect to the LES1.10 and the experiment. This can be due to a larger turbulent transport of momentum in the slope-normal direction. The length l_0 shows more clearly the differences in the DBL thickness of the three profiles caused by the differences in Ra number. This is because, unlike the H length, l_0 is related to the thickness of the TBL in the near surface region, thus, far from the surface, the three scaled profiles does not collapse on the same curve, and this length is not accurate to represent the DBL region; viceversa, the simulations temperature data practically collapse on the same profile (which is not the case of the previous scaling). Temperature data of experiment shows non

comparable values. As a conclusive remark, l_0 behave as an interesting scaling parameter for the TBL phoenomenas that could be used for future works of anabatic flow analysis, although in what follows will be used the scaling based on slope height, which is more diffuse in the current literature.

5.2 Analysis of LES2.78

Simulation LES2.78 has been chosen for an in-depth analysis of the turbulent flow features and behaviour along the slope. An investigation of the instantaneous turbulent structures observable thanks to the LES approach will be also carried out in Section 5.3.

5.2.1 Mean field analysis

Figure 5.5 displays the normalized spanwise averaged velocity and temperature difference along the five rows over the slope reported in Section 4.5. The difference in velocity profiles consists principally in a vertical extension of the peak region, an increase in its intensity and a vertical shift of the maximum's height. Each of these features reflects the increasing in turbulence diffusion from the first row to the fifth, as the anabatic flow develops and became stronger. Also, for $z/H > 0.3$, negative vertical velocities appear. The horizontal velocity profile closer to the slope top (fifth row), registers lower maximum value with respect to the fourth row. This is an evidence of the presence of the ascending flow at the slop end, which deviates the horizontal velocity into vertical velocity. The peak's height in horizontal velocities seems to be co-located with the corresponding peaks of vertical velocities. Figure 5.6 shows the logarithmic scale of temperature difference, which allows to recognize three principal region: the rapid-decrease region ($0 < z/H < 0.02$) dominated by heat conduction and where the temperature follows an exponential decay; the convective region ($0.02 < z/H < 0.5$) dominated by flow convection, which exhibits a gently decay; the equilibrium region ($0.5 < z/H$) that is almost not influenced by the heated slope. In the convective region, temperature profile presents an inflection point.

5.2.2 Second order statistics

Figure 5.7(a) reports the averaged scaled turbulent kinetic energy defined as $\frac{TKE}{U_0^2} = \frac{1}{2U_0^2}(\langle\overline{u'u'}\rangle^2+\langle\overline{v'v'}\rangle^2+\langle\overline{w'w'}\rangle^2)$, taken over the first, third and fifth row. Along these three rows, maximum in TKE changes in intensity, from about $\frac{TKE}{U_0^2} \simeq 2.5$ to $\frac{TKE}{U_0^2} \simeq 7$ at the third row and $\frac{TKE}{U_0^2} \simeq 11$ at the fifth row, while his height

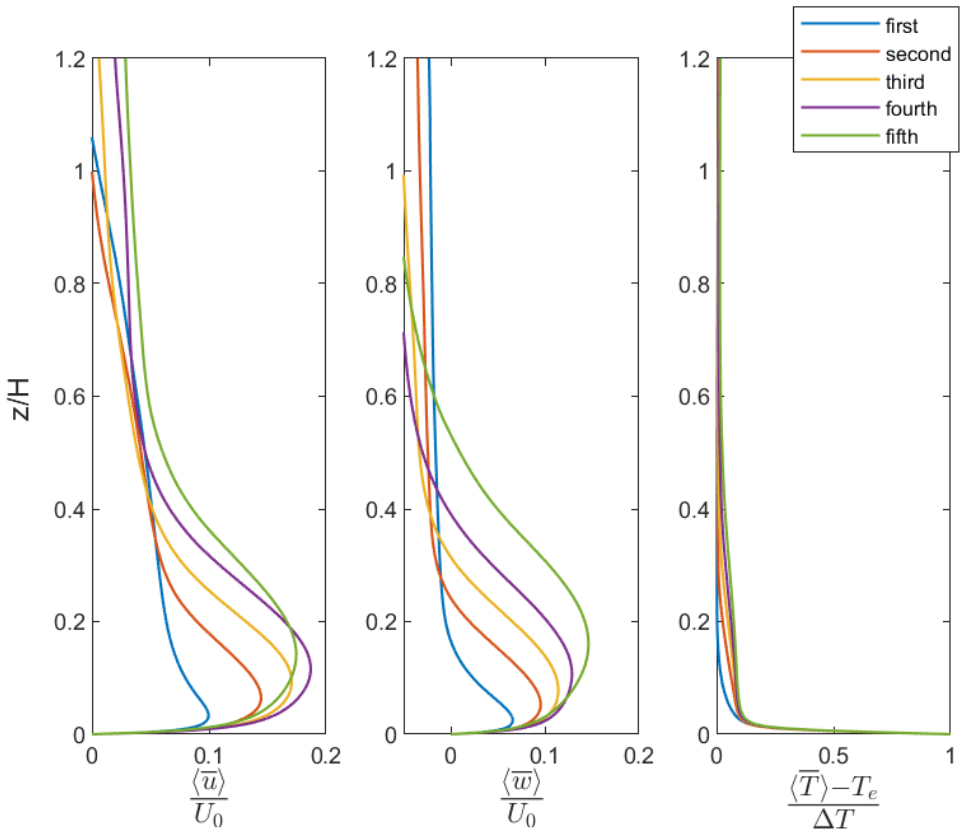

Figure 5.5: Profiles comparison along the slope for normalized horizontal velocity $\langle\overline{u}\rangle/U_0$, normalized vertical velocity $\langle\overline{w}\rangle/U_0$ and normalized temperature difference $\frac{\langle\overline{T}\rangle - T_e}{\Delta T}$.

changes from around $z/H \simeq 0.05$, at the first row, to $z/H \simeq 0.2$ at the second row and to $z/H \simeq 0.3$ at the third row. The enhancement in turbulence energy is explained by the turbulence development along the slope, while the vertical shift of TKE is related to the stronger role of vertical momentum in the development of anabatic flow along slope. This is confirmed by Figure 5.7(a), which shows the scaled vertical turbulent momentum flux over the same rows: turbulent momentum transported upward observed at these rows doubles the value of his near-surface peak ($z/H \simeq 0.05$), from about $\frac{\langle\overline{u'w'}\rangle}{U_0^2} = 1.25$ to $\frac{\langle\overline{u'w'}\rangle}{U_0^2} = 2.5$. From the first to the second row, a local maximum appears at about $z/H \simeq 0.2$, rising to $z/H \simeq 0.3$ in the third row. The position of both the maxima result co-located to the regions of maximum gradient in the mean profiles of $\frac{\langle\overline{u}\rangle}{U_0}$ and $\frac{\langle\overline{w}\rangle}{U_0}$. The local minumum found at about $z/H \simeq 0.1$ is co-located to the region of zero gradient observable in $\frac{\langle\overline{u}\rangle}{U_0}$ and $\frac{\langle\overline{w}\rangle}{U_0}$ profiles. The relation between fluxes and gradients can be explained by the turbulence action that displays stronger fluxes in the region in which gradient are stronger. Viceversa, regions already mixed as those with zero gradient do not exhibit relevant fluxes. For this same reason, the peaks of turbulence flux profiles shift upwards along the slop analogously to the mean profiles behaviour. A similar behaviour is found by Fedorovich and Shapiro, 2009a, which argued in their work that this is a validation of the turbulent eddy-viscosity model discussed in Section

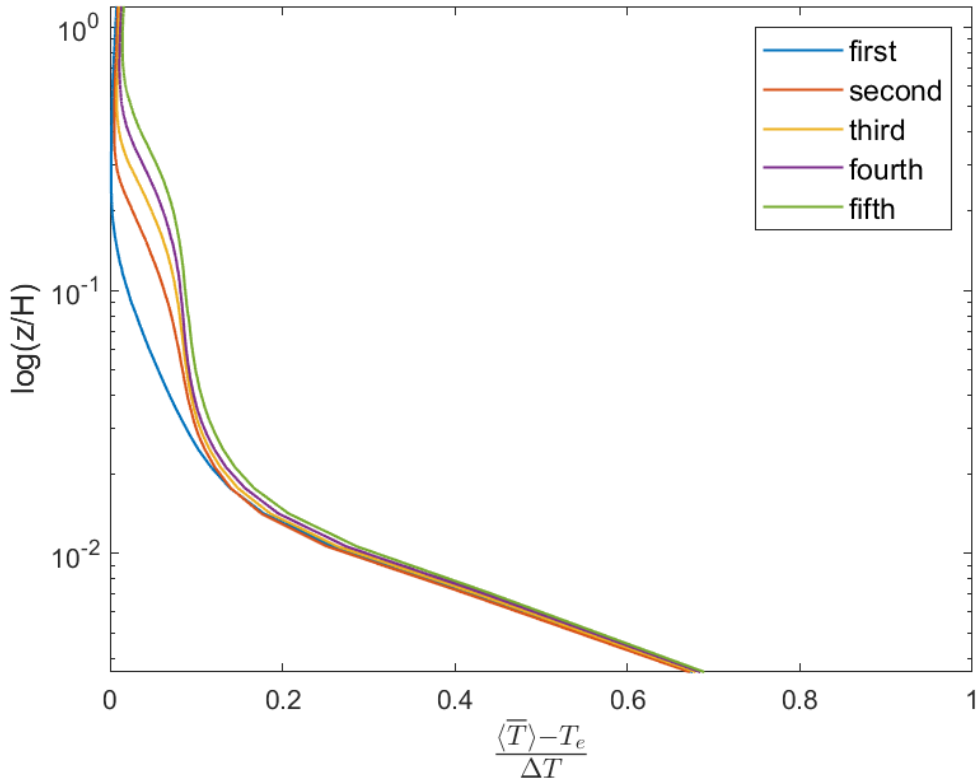

Figure 5.6: Profiles comparison along the slope for normalized temperature difference $\frac{\langle\overline{T}\rangle - T_e}{\Delta T}$ in logarithmic scale.

1.7. In this case the same conclusion cannot be assumed, because the minimum in turbulent fluxes are not zero as expected. This different observation may be due to the different method of turbulence resolution: Fedorovich used a DNS to reslove all the turbulent scales, while the present work shows filtered fluctuations, in which the contribution of the sub-filtered scales is absent. It is notable, however, that along the first row, in which turbulence is less significant, minimum value of vertical momentum flux is near zero, probably because more scales are resolved.

The R_{xz} profiles in Figure 5.7(b) are characterized by a progressive reduction along the rows of his value in the upper area (above $z/H = 0.3$). This feature can be better analyzed in the streamwise cross-section in Figure 5.9(a). Above the last part of the slope between $x/H = 5.4$ and 5.8 and over approximately $z/H = 1.6$ there is a negative area of R_{xz}. This means that the product $\langle\overline{u'w'}\rangle$ is negative, thus characterized by an anticorrelation between $\langle\overline{u'}\rangle$ and $\langle\overline{w'}\rangle$. Since it is expected that the region of enhanced vertical heat flux and velocity is featured by a positive fluctuation $\langle\overline{w'}\rangle$, it is reasonable that $\langle\overline{u'}\rangle$ is negative in that region. This could indicate the turbulence action that widens the principal thermal plume detached at the end of the slope (visible also in the vertical flux of Figure 5.9(c)). This is confirmed looking at the horizontal heat flux cross section of the same Figure

5.9(b), which has negative values in that region, indicating an horizontal exchange of heat in the negative direction.

Figure 5.8 shows the scaled heat fluxes $\frac{\langle\overline{T'u'}\rangle}{U_0\Delta T}$, $\frac{\langle\overline{T'w'}\rangle}{U_0\Delta T}$ and the temperature variance $\frac{\langle\overline{T'T'}\rangle}{\Delta T^2}$. Vertical heat flux profile is strongly affected by the overall convective motion and progressively extends his layer of high values along the slope. The property of having maximum and minimum values respectively co-located with the minimum and maximum gradient in the mean profiles is also observed for the heat fluxes with respect to $\frac{\langle\overline{T}\rangle - T_e}{\Delta T}$ profile.

Momentum fluxes shows high values in a more extended area, up until about $z/H = 0.5$, compared to temperature variances, and decay vertically more gradually.

Horizontal heat flux profile in Figure 5.8(a) shows a region of negative values that disappear after the third profile, after which the flux is always positive.

Both the vertical heat flux profile of Figure 5.8(b) and his cross section in Figure Figure 5.9(c) shows the strong enhancing of the near surface region extension along the slope. After $x/H = 5.4$, the plume column of separated flux is visible in the cross section, and higher values are observed just above the surface. The $\frac{\langle\overline{T'w'}\rangle}{U_0\Delta T}$ surface layer can be compared with the mean velocity layer of Figure 5.5, noting that they extend to the same height.

There is no region characterized by costant fluxes for any of the flux profiles considered. This implies that it is not possible to recognize a definite mixed layer region, so that a layer distinction analogous to that done in Hunt, Fernando, and Princevac (2003)'s work, in which the authors recognized a mixed and an inversion layer above the thermal and dynamical surface layers, is not viable. As Moroni and Cenedese (2015) pointed out, even though Hunt's distinction can be used as a reference for slope wind simulations' results, it is not certain that they will have a complete correspondence with this scheme. From the observations done by them on anabatic flow developed in laboratory, no significant distinction emerged inside the surface layer.

This feature of not having regions of constant fluxes is also noted by Fedorovich and Shapiro (2009) in their article. In such work, they argued the possibility that it may be a specific feature of the slope flows in presence of ambient stratification, but the results of the present work suggest that this absence of a clear mixed layer in tank simulations or experiments could be more general.

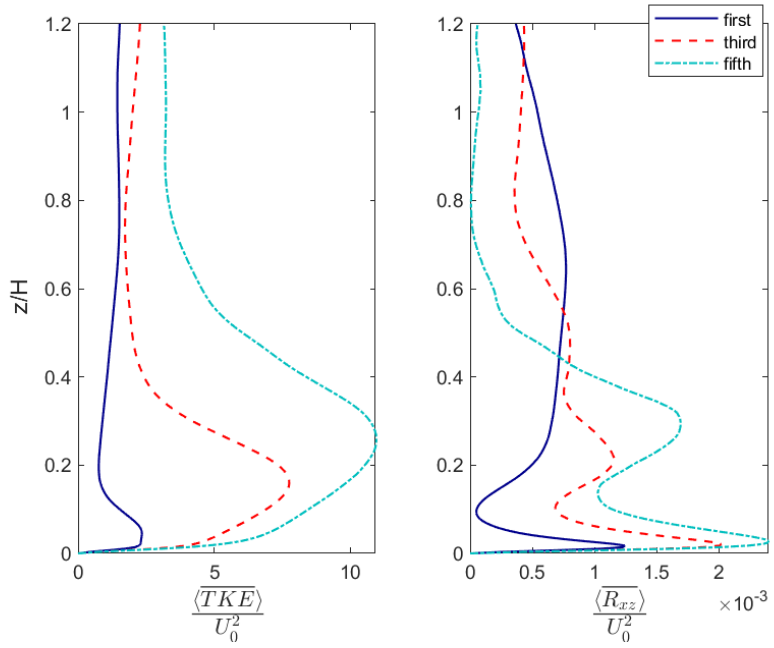

Figure 5.7: Normalized Turbulent Kinetic Energy $\langle \overline{TKE} \rangle / U_0^2$ (a) and normalized Reynolds stress $\langle \overline{R_{xz}} \rangle / U_0^2$ (b)

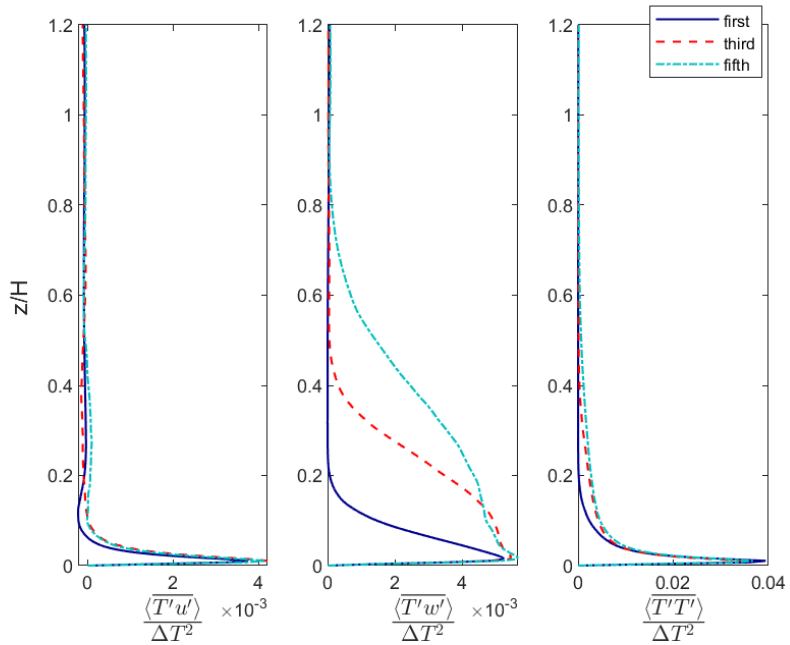

Figure 5.8: Normalized turbulent horizontal heat flux $\langle \overline{T'u'} \rangle / (U_0 \Delta T)$ (a) Normalized turbulent vertical heat flux $\langle \overline{T'w'} \rangle / (U_0 \Delta T)$ (b) and normalized Temperature rms $\langle \overline{T_{rms}} \rangle / (\Delta T^2)$ (c)

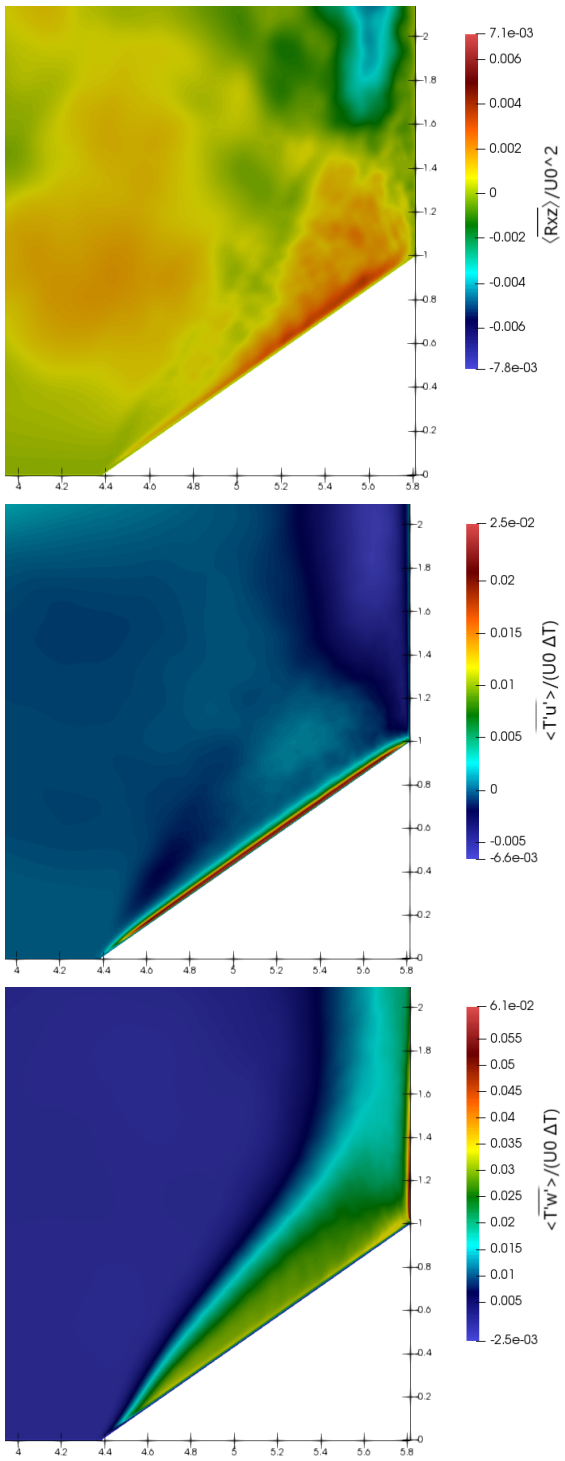

Figure 5.9: Averaged turbulent fluxes along slope.

5.3 Instantaneous fields patterns

Instantaneous fields visualization allows to see the development of peculiar turbulent structures that will be lost in the time and space average operation. The instantaneous fields of vertical velocity (Figure 5.10) and temperature (Figure 5.11) are visualized over three superimposed cross sections, over x-z planes at the begin of the slope, at the center and near the end of the slope (coordinate along slope $s/H = 0$,$s/H = 2.32$,$s/H = 4.65$), focusing on the region near the slope. Both fields show higher values related to the same structures. The dimensions of this structures are clearer in the vertical velocity cross section of Figure 5.10: they arise as little plumes of width $y/H \simeq 0.6$, spaced by an equivalent amount in a quasi-periodic pattern, reaching a height of about $z/H \simeq 0.25$ at half slope. This structures may be generated by the strong near-surface change of temperature arising mainly in the l_0 layer, developing a fluid Rayleigh-Taylor's instability where the warmer near surface fluid pushes the coldest fluid above.

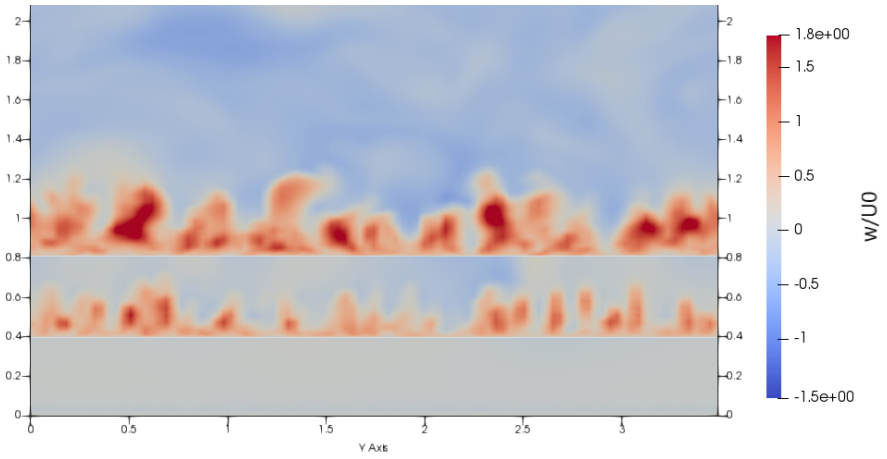

Figure 5.10: Instantaneous normalized vertical velocity w/U_0.

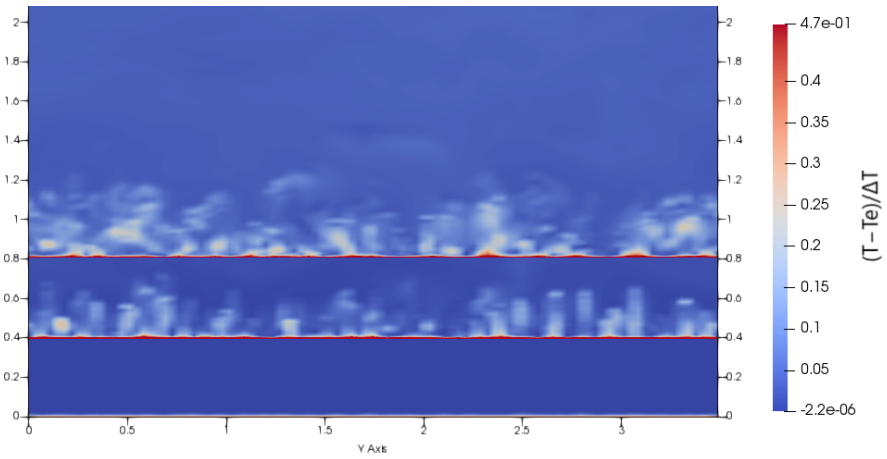

Figure 5.11: Instantaneous normalized temperature difference $\frac{T-T_e}{\Delta T}$.

5.3.1 Along slope distribution

Instantaneous temperature fields in Figure 5.12, shows the same instabilities of Section 5.3 viewed from a slice along the streamwise direction at several simulated times. The different shape is explained by the upslope flow which advect the plumes parallel to the surface, while they are continuously generated by the vertical buoyancy. The structure extension in x-direction is approximately the same of those evaluated in the y-directions: their vertical length evolves along the slope reaching approximately $z/H \simeq 0.35$; their width near the surface, where they are less advected by the anabatic flow, is approximately $x/H \simeq 0.6$. The progressive stretching of the plumes alon the slope can be compared with the enhancement and extension of the turbulent fluxes displayed in Figure 5.9, most clear in the vertical heat flux. This suggest that these plumes are related to the vertical transport of temperature.

An ulterior slice has been done over a plane parallel to the slope allowing a perspective of the plumes from the above. Visualization of the field temperature in Figure 5.13 has been done for four selected time steps in the range analyzed: 402 s,604 s,803 s and 999 s. The structures are observed as a spatial distribution of isolated circular spots of higher values in temperature. This temperature pattern has been compared with the vertical velocity field of Figure 5.14. From this section is visible how this plumes are characterized by a higher positive vertical velocity compared to the surrounding.

The pattern is persistent in time, suggesting a continuous destruction and regeneration of the plumes. This can be explained as the aforementioned process of advection by the anabatic flow that dissipate the plumes while they are continuously generated by the vertical component of buoyancy force. Using the along-slope coordinate s, this generation process begins in the first quarter of the slope ($0 \leq s/H \leq 1.16$), in which the plumes appears well defined in a round shape and separated by spacing intervals of about $y/H \simeq 0.6$. In the last quarter of the slope ($4.65 \leq s/H \leq 5.8$), instead, the plumes begin to enlarge along the y-direction. This may be due to the strengthening of the anabatic flow along the slope that dissipates the structures more efficiently as the end of the slope is approached.

Figure 5.15 shows the time travel estimation of a single plume from the beginning to the end of the slope. A rough estimation of this time through snapshots of a single case is approximately 100 s.

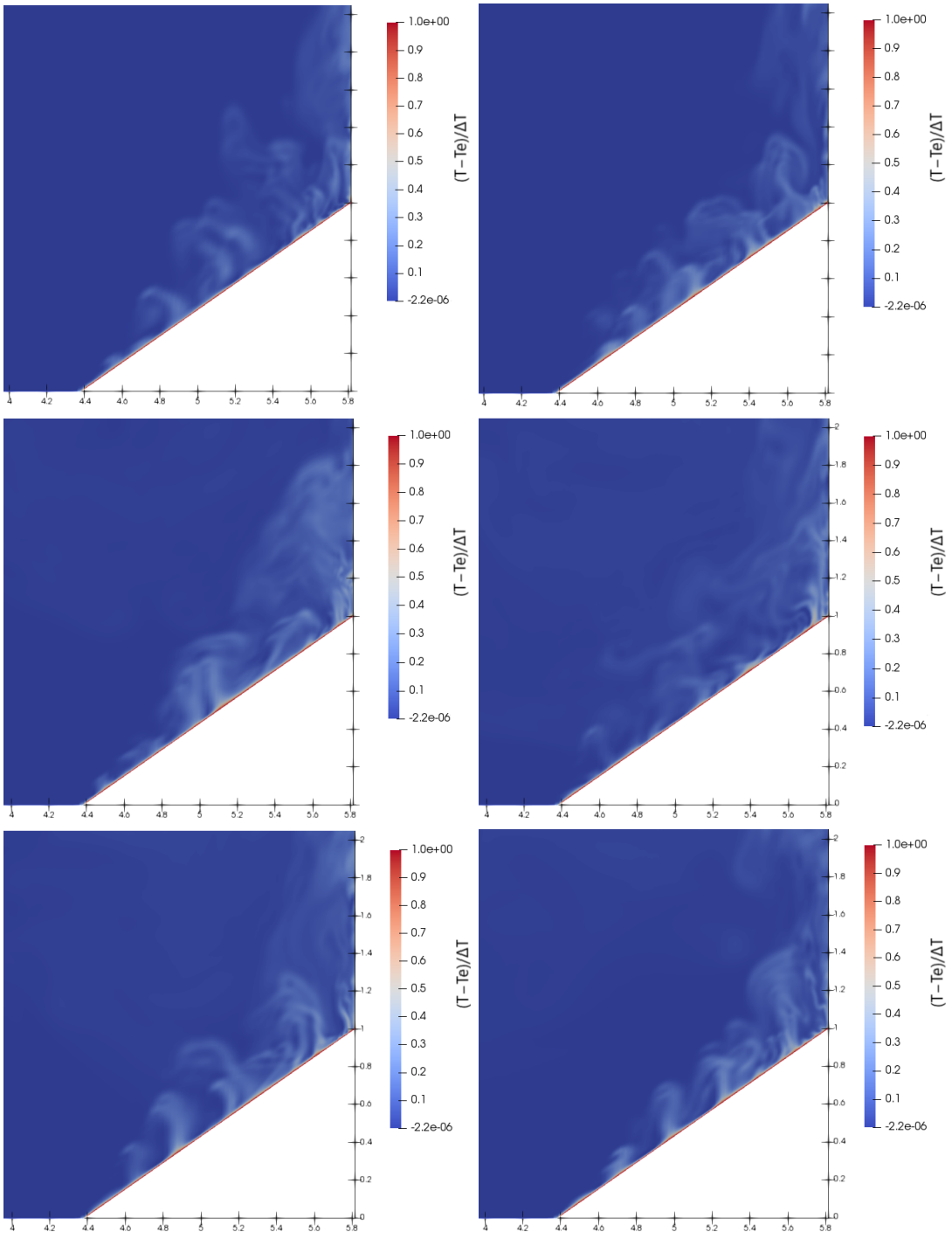

Figure 5.12: Pattern evolution along slope for the instantaneous normalized temperature difference $\frac{T-T_e}{\Delta T}$.

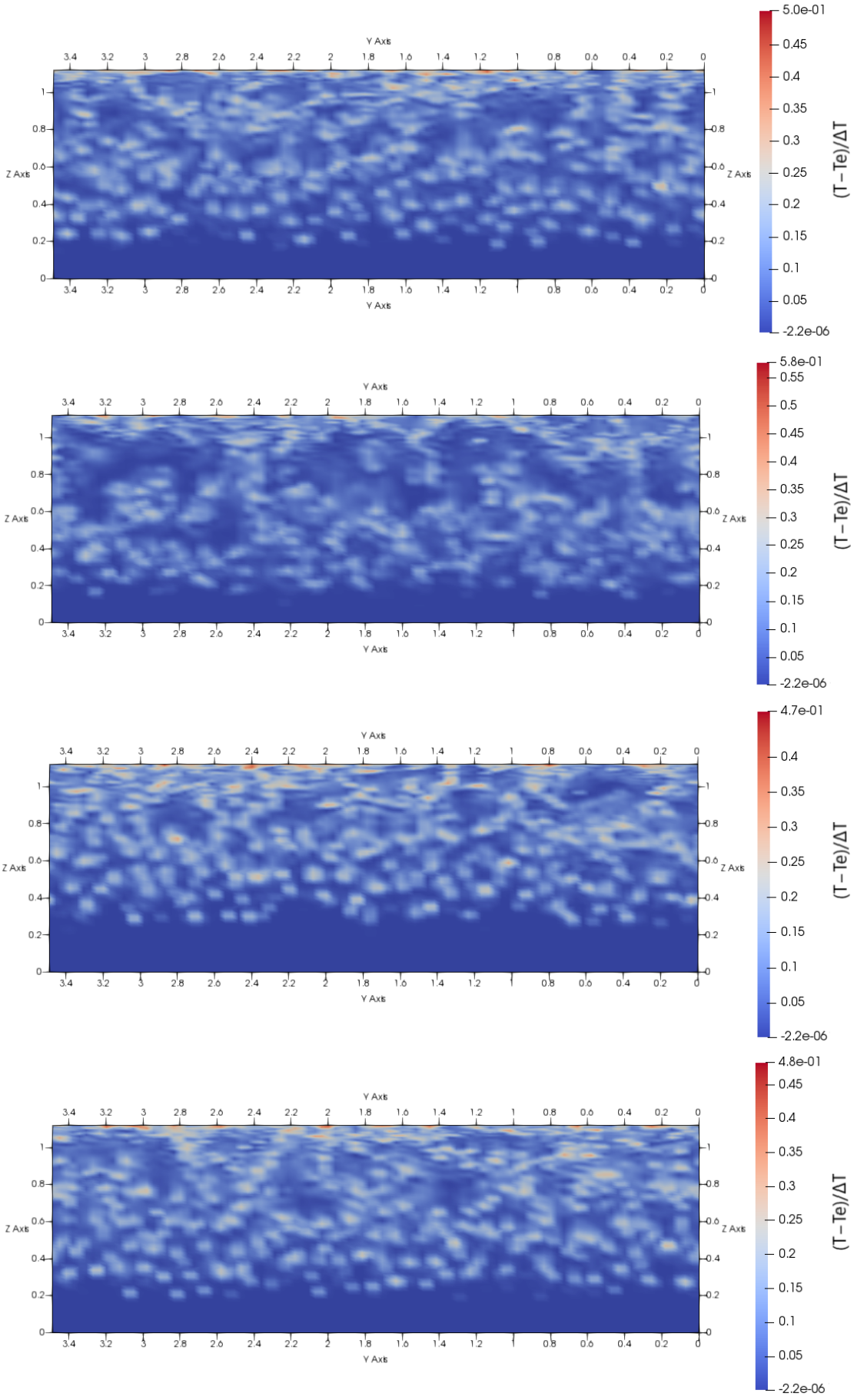

Figure 5.13: Instabilities development over time for instantaneous normalized temperature difference $\frac{T-T_e}{\Delta T}$.

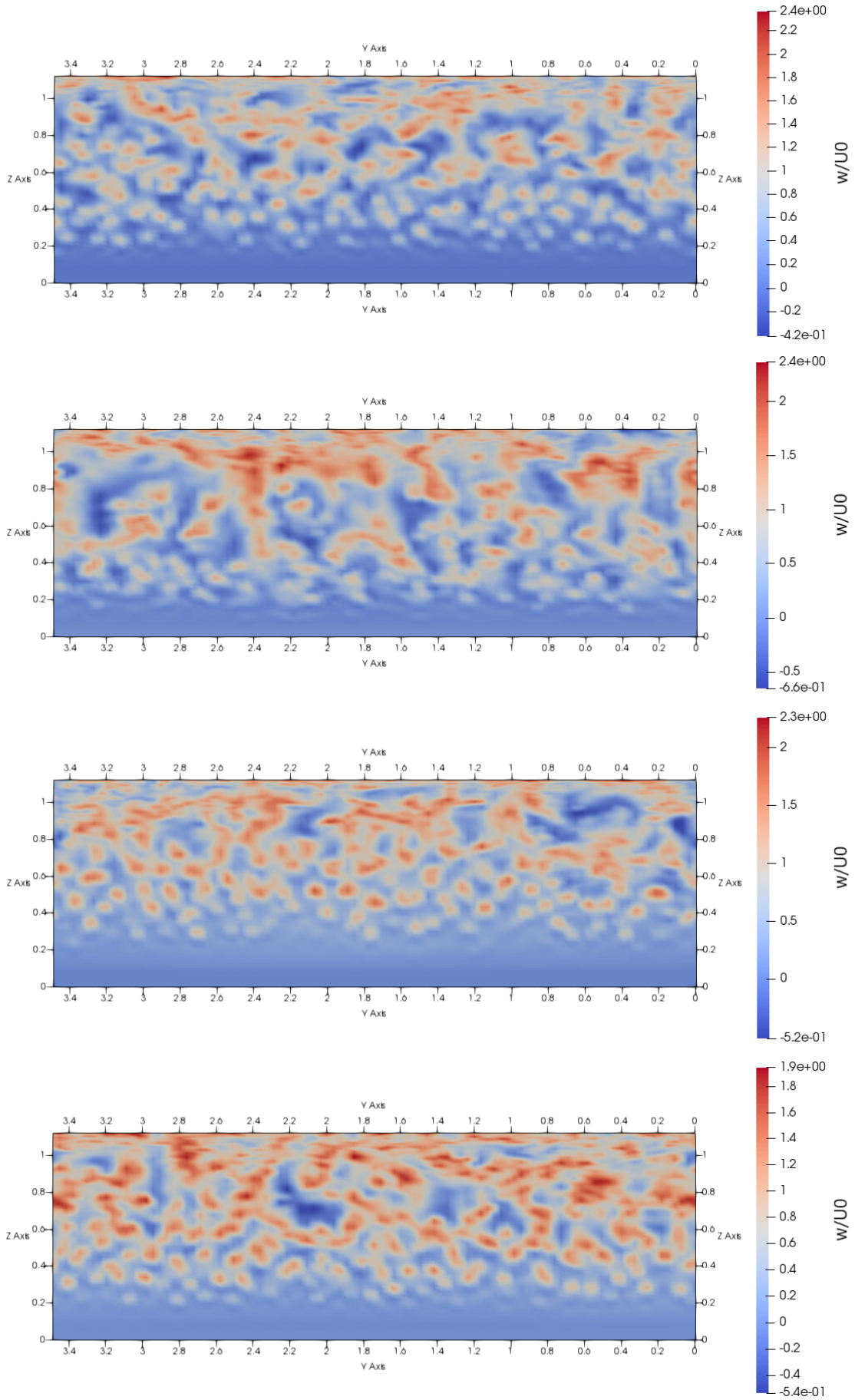

Figure 5.14: Instabilities development over time for instantaneous normalized vertical velocity w/U_0.

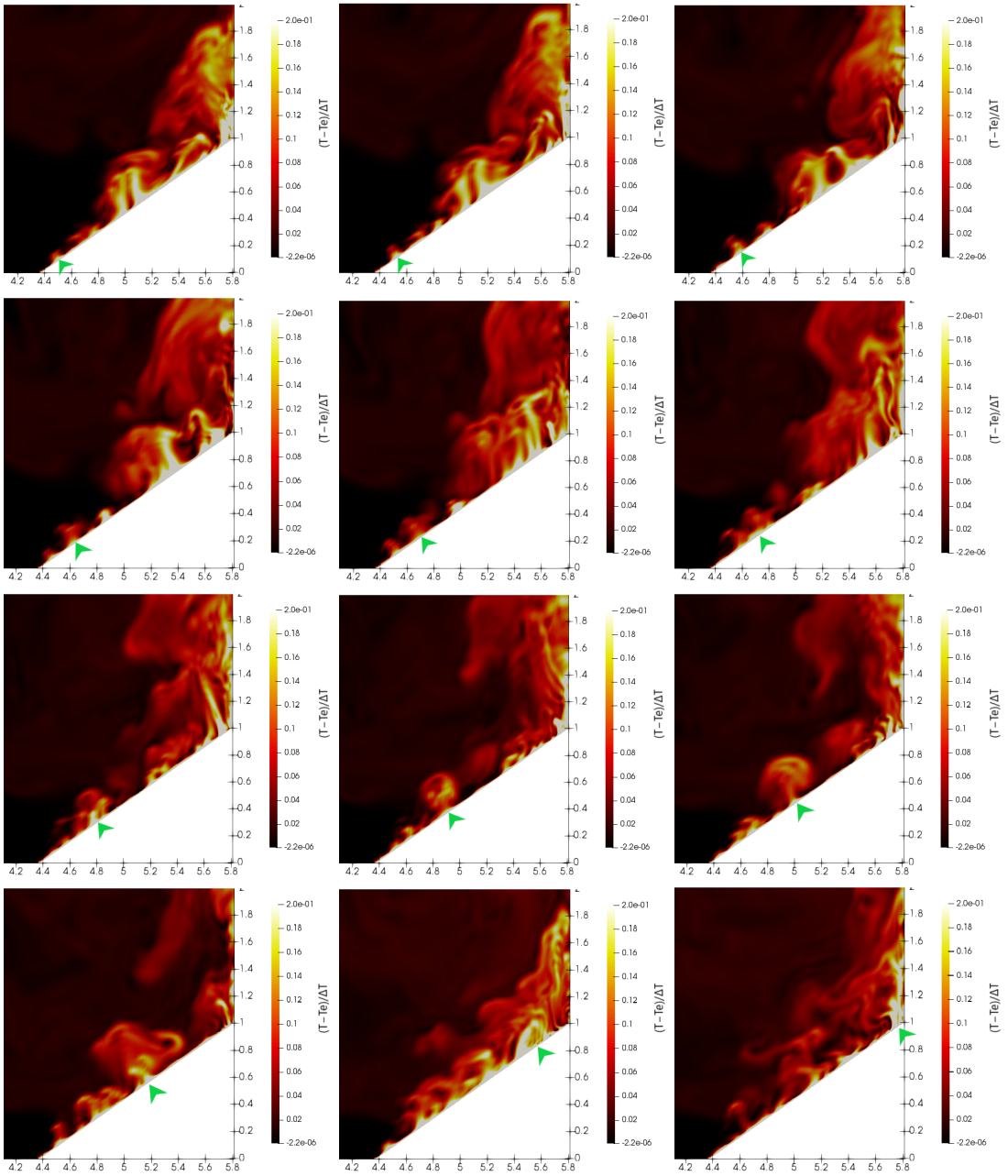

Figure 5.15: Path of a plume generated by the thermal instability and advected by the anabatic flow. Snapshots starts from time 603s and goes to 606s, 612s, 618s, 624s, 630s, 636s, 642s, 648s, 660s, 687s and 702s

5.3.2 Frequency analysis of thermal plumes

An estimation of the characteristic time of the plumes occurrence can be done through a spectral analysis of the temperature and velocity time-series. Ten virtual probes are placed at different levels and distances from the slope (see Table 4.5b) to record temperature and velocity components during the simulated time period. The average sampling frequency is $f_{ave} = 28.8$ Hz. The power spectra density is estimated by the Welch (1967) method, based on the Fast Fourier Transform[1]. All the probes are scrutinised and show similar features; hence, for the seek of conciseness the probe n.2, for analyzing the near-surface region, and the probe n.10, for analyzing the far surface region, are reported and discussed.

Figure 5.16 displays the dimensional temperature time-series and the relative power spectrum density of probe n.10. The primary frequency is clearly detected at $f_3 = 0.028$ Hz. The same value is found at virtual probe n.1 and is also visible as secondary frequency at larger distance from the slope. A secondary frequency is detected at $f_2 = 0.0176$ Hz. Such frequency appears persistently and becomes predominant from probe n.4 on. At highest level, also the frequencies $f_4 = 0.039$ Hz and $f_5 = 0.045$ Hz becomes relevant.

Figure 5.18 depicts the time-series of dimensional horizontal and vertical velocity components, and the relative power spectrum densities. In both components, f_2, appears as the primary frequency of u and the second maximum frequency of w. This same frequency becames predominant for both components at each of the probes between n.4 and n.9. Another frequency $f_1 = 0.006$ Hz emerges, which can be detected in all the probes, although f_1 and f_3 assumes lower spectral values with respect to f_2. The temperature frequency f_4 is also clearly identified in correspondence of a local maxima of w's spectrum.

Figure 5.17 reports dimensional temperature time-series and power spectrum density for probe n.2. The primary frequency is found at $f_6 = 0.081$ Hz. Probe n.1 shows the same maximum and probes at larger distance from the slope shows it as a secondary maximum. It is worth to notice a secondary frequency $f_2 = 0.0176$ Hz, that becomes predominant farther form the surface (from probe n.4 on). At highest level, appears the frequency $f_7 = 0.120$ Hz.

Velocity components u and w are not reported, but shows the primary frequency f_2 already found, while emerges also $f_1 = 0.006$ Hz and $f_3 = 0.028$ Hz. The temperature frequencies f_6, f_7 are also clearly identified. The principal and secondary frequencies detected are summarised in Table 5.5, along with the corresponding time-period.

[1]Specifically, we used the Octave function *pwelch* with the Gaussian window-function. See the Octave documentation of package "signal" for additional details.

Two extra probes are analyzed at non-dimensional distances d/H = 0.29 and d/H = 0.058, the first being approximately the estimated maximum length reached by the plumes, and is notable that f_2 remains persistently as a secondary maxima in the temperature while disappear from velocity components at probes n.12.

The time-period of the frequency detected can be related to characteristic time scales. Suitable characteristic velocities are the heat flux velocity defined in Section 4.4.1 $U_q = (q_0 H)^{1/3}$ and the diffusion velocity defined in Section 5.1.2 $u_0 = \sqrt{g\beta\Delta T l_0} = 0.0032$ m/s. The surface heat flux is estimated by avaraging Q in time and at the slope surface. The final value is Q=910.11 W/m^2, giving $U_q = 0.0053$ m/s. Both velocities can be used to find characteristic times. The length used for this purpose are: the width of the slope base $W = Lcos(\alpha)$, in order to detect phoenomena propagating horizontally along the slope and the height of the slope $H = Lsin(\alpha)$, for phoenomena propagating vertically normal to the slope.

Table 5.6 shows characteristic times for each of the four length scale choiced.

From a comparison between the characteristic times and primary frequencies, the following observations can be made:

- low frequencies (< 0.01 Hz) that appears in the probes analysis have a very large period and can be possibly related to weak interferences from the recirculation arising in the upper part of the domain;
- frequencies f_3 and f_2 can be related to vertical and horizontal motion of the anabatic flow.
- frequency f_6 has a period of 12 seconds, that has no correspondences with the characteristic times calculated, but has approximately the same value of $\tau_T = L/U_0$, where $U_0 = 0.030$ is defined in Section 5.1.1. This is recognised to be the frequency of the thermal plumes, since it is predominant in temperature time-series and also present in velocity components time-series, at the probes close to the slope surface, at the base of the plumes generated, where they and are expected to assume the highest temperature values in the form of heat waves (see Figure 5.19).

	Frequency [Hz]	Period [s]	Principal for u,w	Principal for T
1	$f_1 = 0.006$	$T_1 = 166.66$		
2	$f_2 = 0.0176$	$T_3 = 56.8$	*	*
3	$f_3 = 0.028$	$T_2 = 35.71$	*	
4	$f_4 = 0.039$	$T_5 = 25.64$		
5	$f_5 = 0.045$	$T_4 = 22.22$		
6	$f_6 = 0.081$	$T_4 = 12.34$		*
7	$f_7 = 0.12$	$T_4 = 8.33$		

Table 5.5: Highest frequencies and dimensional time-period from the spectral analysis of the probes n.2 and n.10 along the central row. The principal frequency for the velocity components and the temperature is also marked.

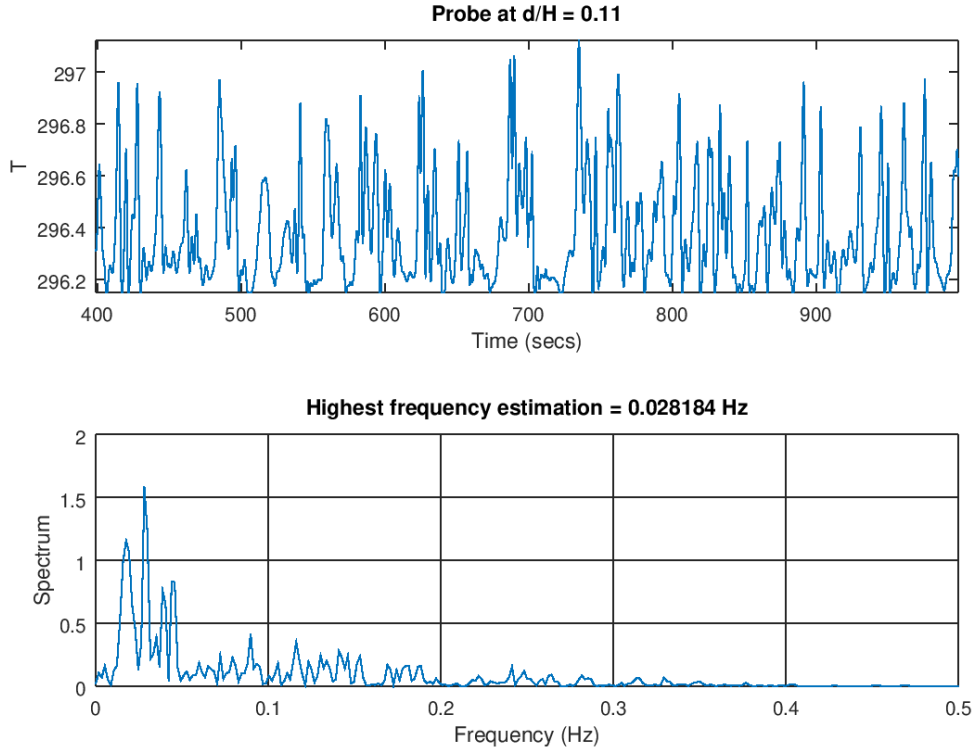

Figure 5.16: Temperature time-series (first and third panels) and Power Spectrum Density (second and fourth panels) for the virtual probe n.10, at the non-dimensional slope distance d/H = 0.11.

length [m]	τ_q [s]	τ_0 [s]
$W = 0.2457$	46.26	76.78
$H = 0.1721$	32.47	53.78
$L_{tot} = 1$	188.67	312.5
$H_{tot} = 1.2$	226.41	375

Table 5.6: Characteristic times calculated from heat flux velocity $U_q = 0.0053$ and thermal diffusion velocity $u_0 = 0.0032$, for the following length: the width of the slope base W, the maximum height of the slope H, the total doamin length L_tot and the total domain height H_tot.

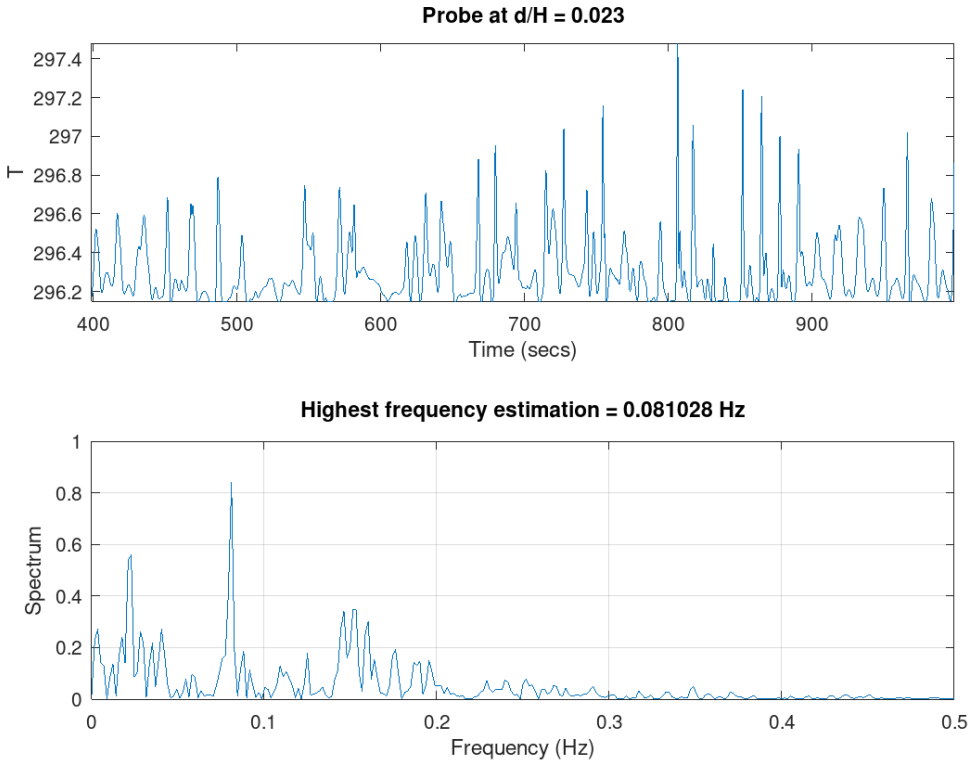

Figure 5.17: Temperature time-series (first and third panels) and Power Spectrum Density (second and fourth panels) for the virtual probe n.2, at the non-dimensional slope distance d=H = 0.023.

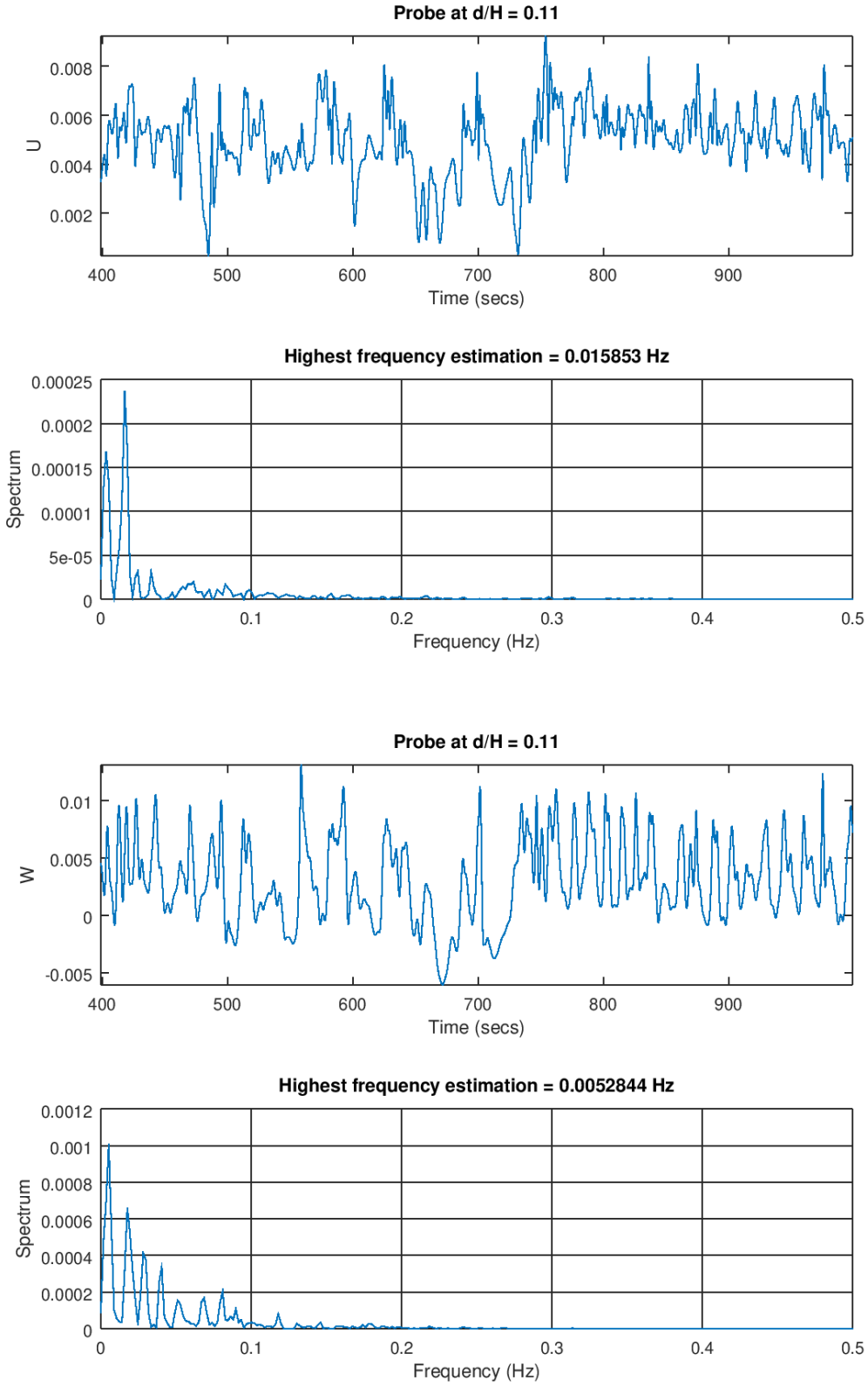

Figure 5.18: Velocity components time-series (first and third panels) and Power Spectrum Density (second and fourth panels) for the virtual probe n.10, at the non-dimensional slope distance d/H = 0.11.

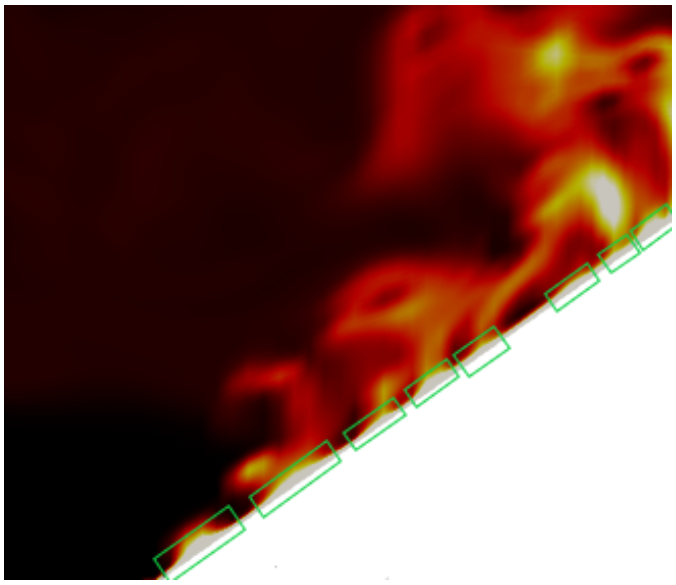

Figure 5.19: Heat waves displayed inside the green markers at the base of the plumes.

5.3.3 Summary on thermal plumes structure

The purpose of this section is to outline the principal features highlighted in the last sections about the thermal plumes. Figure 5.20 presents the sketch of the plumes evolution along the slope. The slope can be divided into three region:

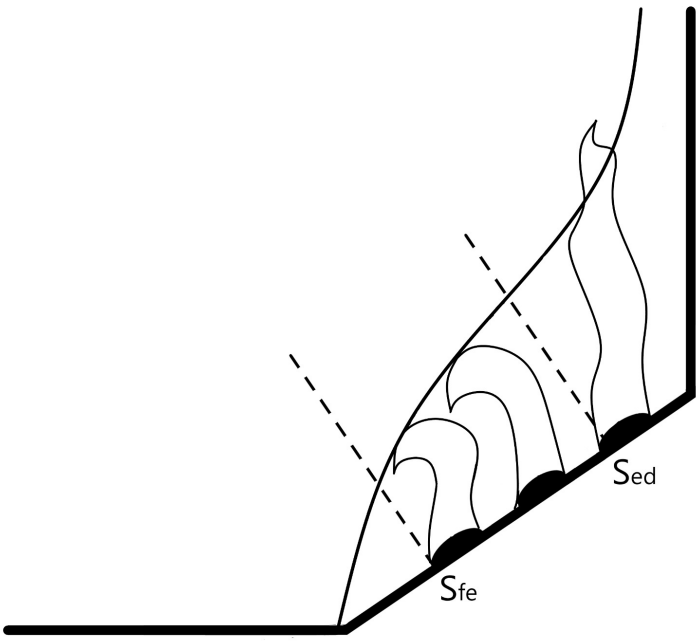

Figure 5.20: Sketch of the plume evolution along the slope. The S_{fe} depicts the point of transition between the free region (in which no plumes are detected) and the evolution region, the S_{ed} depicts the point of transition between the evolution and the dissipation region.

the first region ($0 < s/H < 1.16$) where no plumes are detected; the second

region ($1.16 < s/H < 4.65$) in which the plumes are generated and evolves; the third region, the dissipation zone ($s/H > 4.65$), in which the plumes are mainly dissipated. The absence of the plumes in the first region may be due to weaker turbulence which could be not enough to trigger the instability mechanism. At the plumes' bases are the heat waves, generated as Raileigh-Taylor instabilities by the action of the buoyancy force at the interface between the conduction and convective layer defined in Section 5.2.1 and displayed in the temperature profile in Figure 5.6. Their frequency of occurrence, measured at the central row, results of approximately 12 seconds.

Above each of the heat waves, the instabilities evolve vertically as plumes, which assume a particular hook-like shape under the advection of the anabatic flow that drives them in the upslope direction (see Figure 5.12). The hook-like shape develops opposite to the upslope flow direction. Such plumes are confined inside the convective layer reported in Figure 5.6.

The extension of these plumes is also linked to the vertical turbulent heat fluxes $\langle\overline{T'w'}\rangle$. The evolution of such fluxes along the slope can be seen in Figure 5.9. It is clearly visible an area of turbulent vertical convection characterized by highly energetic vertical turbulent heat fluxes. The height of this area is $z/H \simeq 0.2, 0.4, 0.8$ at the first, the third and the fifth rows respectively. The heights of the plumes (see Figure 5.12) are comparable to this value, hence, the plume develops within the turbulent vertical convection area.

The presence of these plumes enhances the vertical transport of temperature, strenghtening the vertical mixing inside the convection layer.

5.4 Comparison between simulations at different Rayleigh number

In this section, a sensitivity analysis based on the Rayleigh number will be performed. LES0.44, LES1.1 and LES2.78 are characterized by $Ra = 2.83 \times 10^7$, $Ra = 7.08 \times 10^7$ and $Ra = 1.79 \times 10^8$. The three simulations will be compared along the slope over the first, third and fifth row defined in Section 4.8.

5.4.1 Mean profiles over the slope

Turbulence enhances diffusion, enlarging the peak region and smoothing the gradients. For this reason, as showed in Figure 5.21, increasing Ra number in the simulations has the effect of making velocity profiles more uniform along the z/H direction and peak's regions larger. Along the slope, this effect influences

each of the three profiles, bringing them closer and making them approach to a similar shape. The differences at the beginning of the slope for both the velocity components, can be explained in terms of Ra differences, because lower Ra implies that turbulence in the flow is triggered further on in the path over the slope. For all the simulations, both the peaks height and intensity increases along slope. Vertical velocity of LES2.78 and LES1.10 shows negative values over the first row above the peak region, suggesting that the more turbulent simulation is characterized by a descending flux along the slope.

Figure 5.22 presents the non-dimensional temperature profile along the selected vertical lines. The three thermal regions described in Section 5.1.2 can be identified for all the cases. The larger differences among the profiles are detectable in the conduction region ($0 < z/H < 0.02$) where temperature exhibits an intense drop: the average temperature decreases as the Rayleigh number increases. This is due to the turbulence diffusion that transfers heat from the near slope layer to the vertical direction, also by means of instantaneous thermal plumes described in section 5.3. It is worth to note that increasing turbulence tends to generate cooler profiles in the near surface region and warmer profiles in the above region. Along the slope it is visible in each of the three simulations the generation of the convection region, which reaches around $z/H \simeq 0.1$ in the last row, associated with the strong vertical heat flux and plume generation. This association will be confirmed in the turbulent flux analysis.

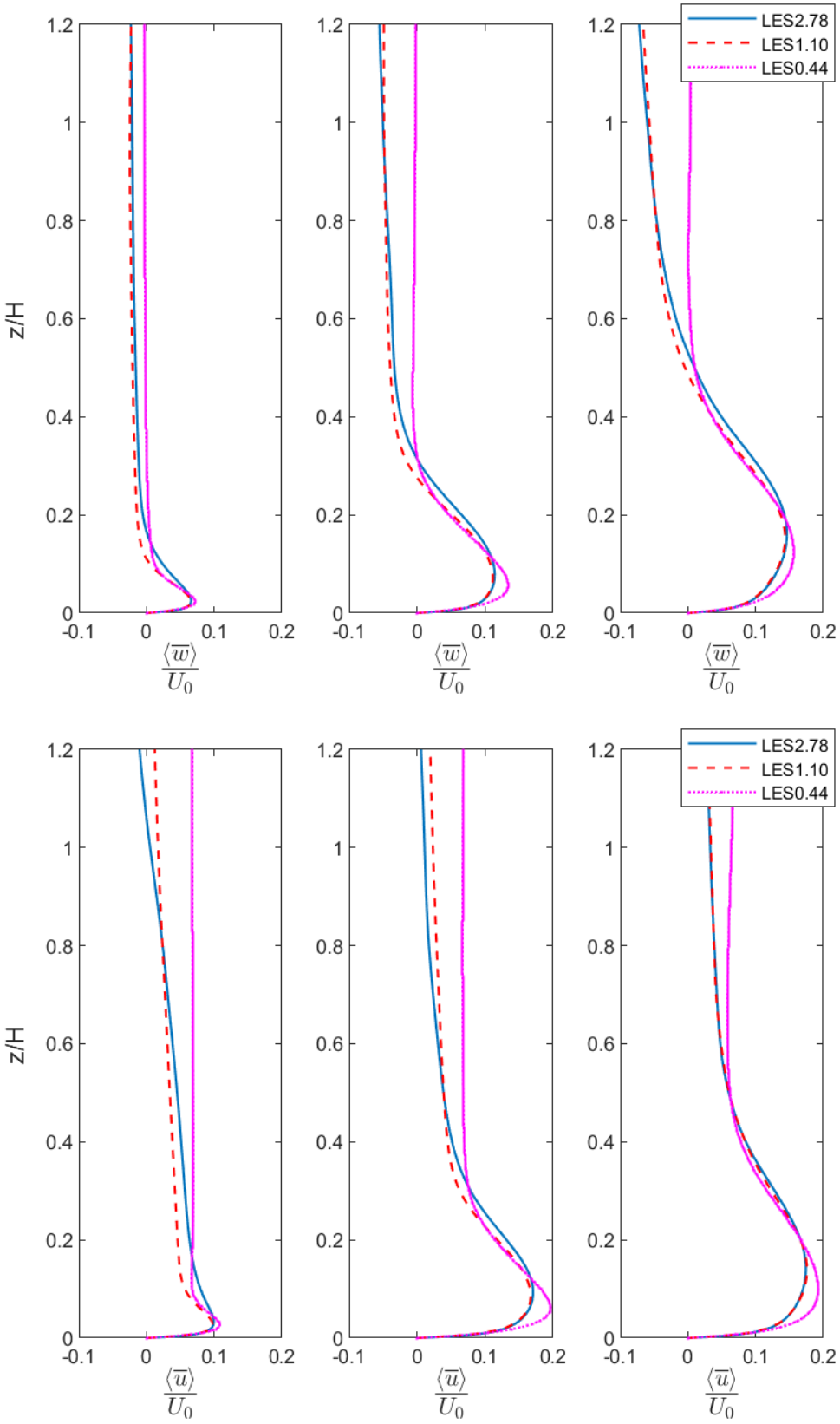

Figure 5.21: Scaled horizontal velocity $\langle \overline{u} \rangle / U_0$ and scaled vertical velocity $\langle \overline{w} \rangle / U_0$ profiles comparison of the three simulation for the bottom line over the slope (first plot), central line over the slope (second plot) and top line over the slope (third plot).

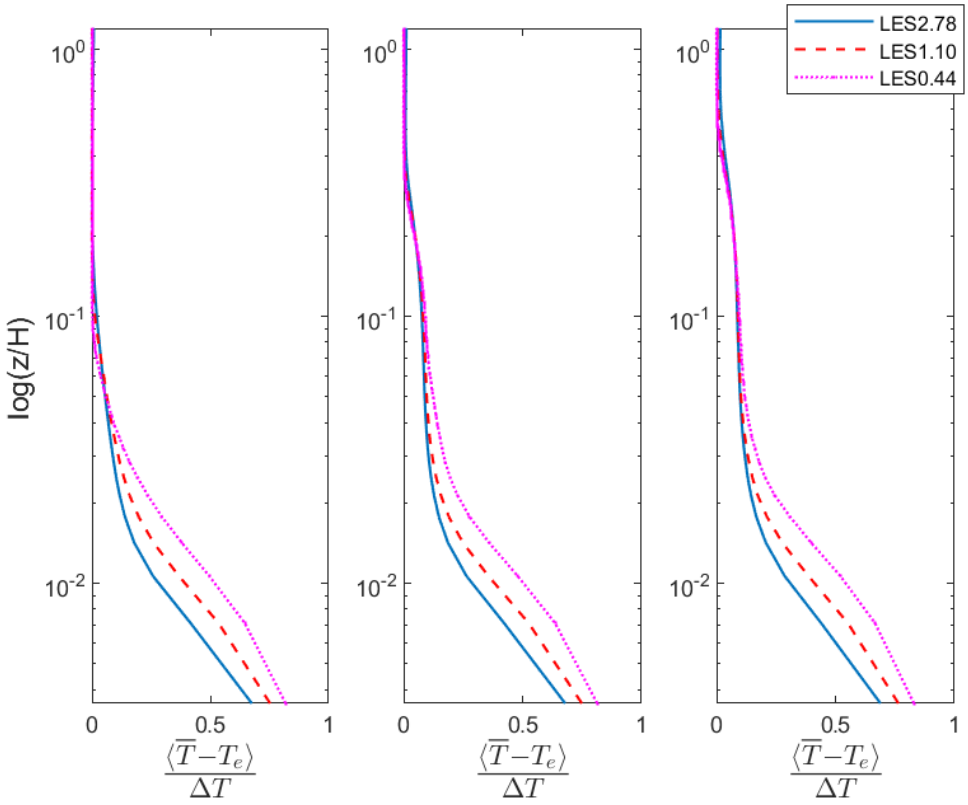

Figure 5.22: Scaled temperature difference $\frac{\langle\overline{T}\rangle-T_e}{\Delta T}$ logarithmic profiles comparison of the three simulation for the bottom line over the slope (first plot), central line over the slope (second plot) and top line over the slope (third plot).

5.4.2 Turbulent heat flux profiles over the slope

Figure 5.23 reports horizontal heat flux and vertical heat flux profiles. Horizontal heat flux maximum at about $z/H = 10^{-2}$ results co-located to the maximum gradient heigth inside the conduction layer in the mean temperature profile. It is notable that the peak in LES0.44 starts the slope at the lowest height ($z/H = 10^{-2}$) of the three simulations and reaches the end of the slope above the other simulation's maxima ($z/H = 2 \times 10^{-2}$). Simulation LES1.10 also appears to have stronger variations than LES2.78 but weaker than LES0.44. The variations in intensity for the LES0.44 and LES1.1 are also more pronounced, while LES2.78 changes very little his maximum intensity. This suggests that less turbulence implies more reactivity in horizontal heat flux variations.

Vertical heat fluxes in Figure 5.23 progressively generates for each of the simulations an extended region of high heat transport between $10^{-}2 < z/H < 3 \times 10^{-}1$ at the end of the slope. The production of this region takes place inside the convection region that generates over the same rows in Figure 5.22. This points out the relation between the convective region and the enhancing of vertical heat flux. Even in this case is observed the same features seen for the horizontal flux case: variations in vertical heat fluxes are higher for simulation of less turbulence. For both the cases the explanation can be the following: simulations of higher Ra are characterized by more developed turbulence, thus they have reached a more stationary regime; lower Ra implies that turbulence requires more space to develop along the slope, thus undergoing stronger variations along the path of the flow. Arguably, if the slope was longer, the three simulation would have a more similar behaviour over the different rows.

5.4.3 Turbulent momentum flux profiles over the slope

As shown in Figure 5.24a, even in the vertical momentum flux it is observed a tendence of the less turbulent simulations to be more prone to variations along the slope, with both the LES0.44 and the LES1.10 starting below the peak intensity of the LES2.78 and surpassing it at the end of the slope, also increasing more rapidly their peak's height. The explanation may be the same of that discussed in Section 5.4.2. There is a notable region between $z/H \simeq 0.05$ and $z/H \simeq 0.1$ above the near surface peak region in which upward transfer of momentum is weak or negative, as in the case of LES0.44. This region extends and smooths along slope, while a second low-flux region generate for each of the simulations between $z/H \simeq 0.5$ and $z/H \simeq 0.2$. This second minimum region stretches up to $z/H \simeq 0.6$ for the LES1.10 case and up to $z/H \simeq 0.8$ for the LES2.78. For the LES2.78, the most turbulent one, the same argument of Section 5.2.2 about the co-located flux minima

and gradient maxima is still valid here. For LES1.10 and LES0.44, this co-location is detectable only on the third profile, where turbulence is most enhanced. Thus the discrepances observed over the other two rows could be explained by the less developed turbulent regime, already observed in section 5.4.2.

In the TKE profiles (Figure 5.24b) is visible the strong tendency to increasing the peaks height as the turbulence increase, reaching an overlapped configuration for the LES1.10 and LES2.78, while the LES0.44 shares the same general shape but displays lower intensities. This is another difference due to different turbulent regime of LES0.44.

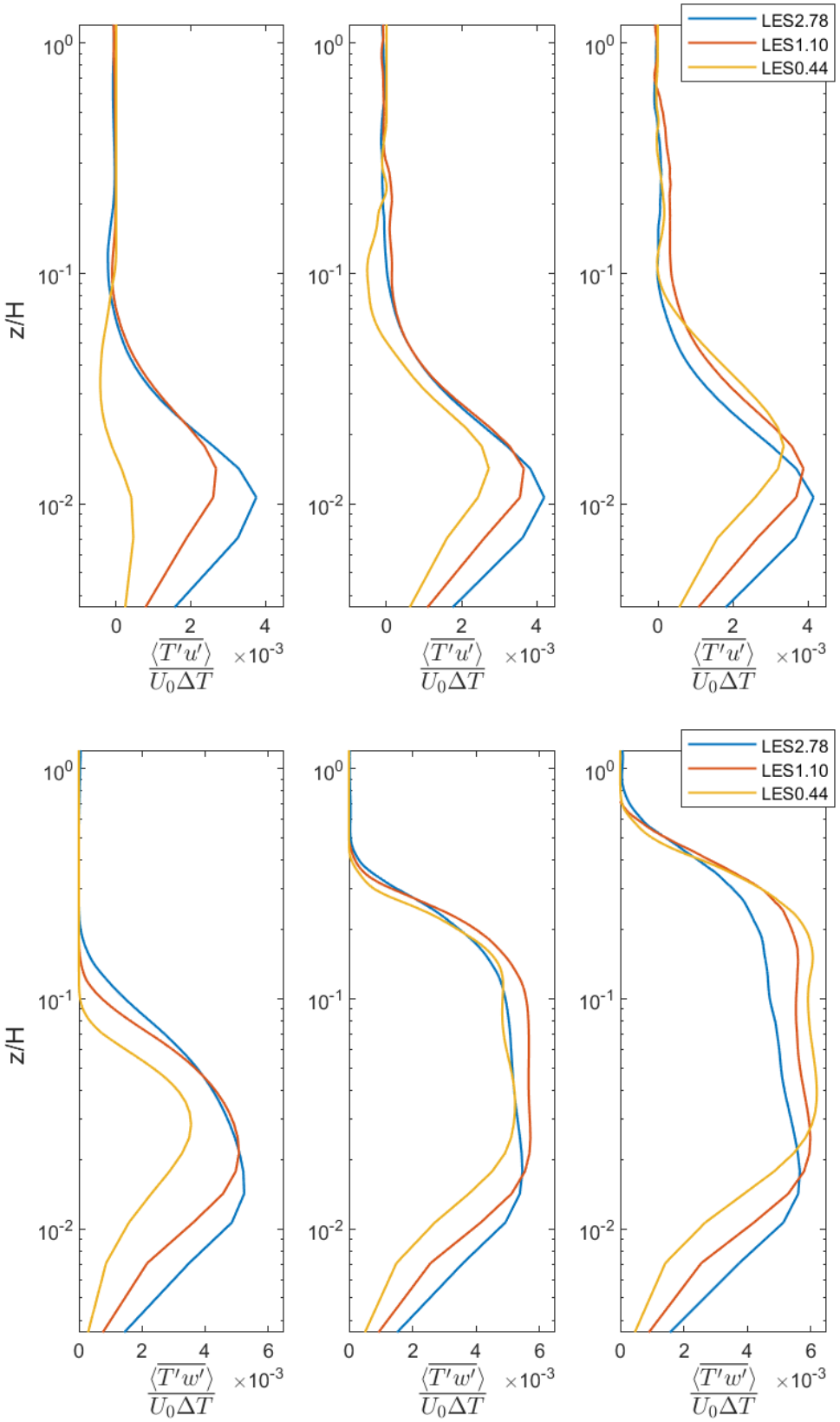

Figure 5.23: Scaled horizontal heat flux $\langle \overline{T'u'} \rangle / (U_0 \Delta T)$ and scaled vertical heat flux $\langle \overline{T'w'} \rangle / (U_0 \Delta T)$ logarithmic profiles comparison of the three simulation for the bottom line over the slope (first plot), central line over the slope (second plot) and top line over the slope (third plot).

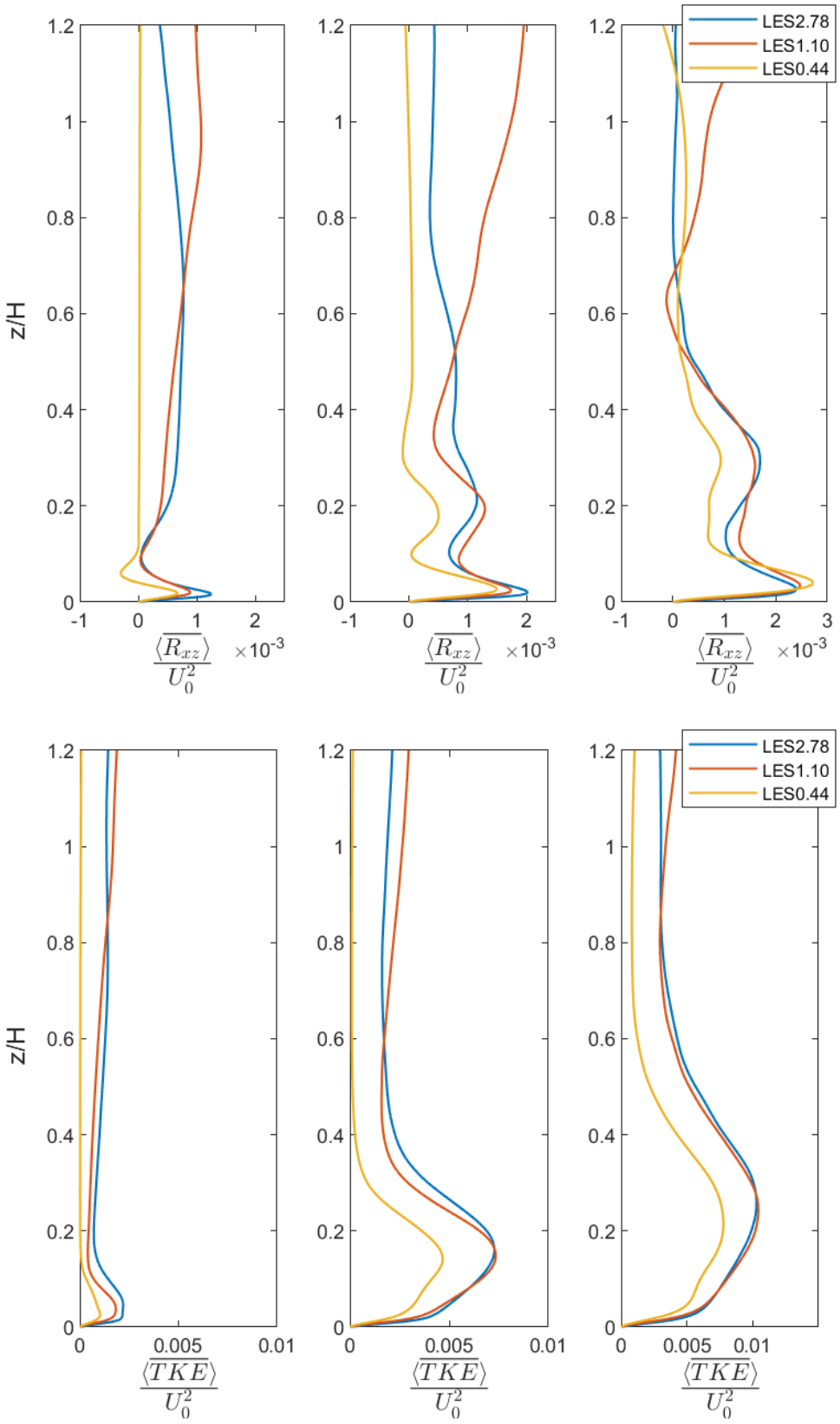

Figure 5.24: scaled vertical momentum flux $\langle \overline{R_{xz}} \rangle / U_0^2$ and scaled turbulent kinetic energy $\langle \overline{TKE} \rangle / U_0^2$ profiles comparison of the three simulation for the bottom line over the slope (first plot), central line over the slope (second plot) and top line over the slope (third plot).

Conclusions

This thesis focused on the numerical simulation of a turbulent anabatic flow over a uniformly heated slope in a simplified geometry, using the large-eddy simulation (LES) method and the Smagorinsky model for sub-grid scale motion.

Three simulations are performed at different Rayleigh numbers ($Ra = 2.83 \times 10^7$, $Ra = 7.08 \times 10^7$ and $Ra = 1.79 \times 10^8$), reproducing a tank full of water with a sufficiently high ceiling, in order to not affect the slope with boundary effects. The computational grid is adequate to directly solve the wall boundary layer ($y^+ < 1$). The selected Rayleigh numbers are based on three differences of temperature (between the slope and the surrounding fluid) that can be used in laboratory experiments. A sensitivity analysis on these Ra values wants to investigate the presence of different fluid regimes.

The simulation with $Ra = 7.08 \times 10^7$ is validated against three datasets: the experimental data provided by the work of Liberzon; the DNS in stable stratification reported in the work of Fedorovich and Shapiro (2009); the theoretical Prandtl model for stationary and laminar slope flows. Despite the differences due to different assumptions in such studies, the simulation adequately reproduces the reference data and displays the characteristic features of a turbulent anabatic flow.

A new thermal diffusion length scale l_0 has been introduced and tested as a scaling parameter. This length has been derived from the characteristic diffusion length used in other heat transfer problems. The l_0 resulted to be a good estimation of the thermal boundary layer thickness.

The numerical simulation at $Ra = 1.79 \times 10^8$ has been chosen for an in-depth analysis of the turbulent flow features. The normal slope coordinate z has been scaled with the slope's maximum height H. Three principal regions are detected in the near-surface temperature profiles: a rapid-decrease region ($0 < z/H < 0.02$) dominated by heat conduction where the temperature follows an exponential decay; a convective region ($0.02 < z/H < 0.5$) dominated by flow convection, which exhibits a gently decay; an equilibrium region ($0.5 < z/H$) that is almost not influenced by the heated slope.

Transient turbulent plumes were detected over the slope. These structures are not easily detectable in experiments and not reproduced by RANS (which are widely used in literature). These plumes are recognized as Rayleigh-Taylor instabilities, which are generated by the strong temperature gradient present in the

thin layer near the surface and are continuously dissipated by the advection of the anabatic flow along the slope. Their characteristic frequency has been measured with a spectral analysis. The corresponding characteristic time is comparable with the time scale based on l_0 and the convective velocity. The analysis of the plumes' spatial dimensions along the slope pointed out a correlation between the vertical extension of the plumes and the depth of the convection region, interested by higher turbulent heat fluxes. This can be interpreted as a contribution of the plumes in enhancing the vertical mixing.

The comparison between the three numerical simulations at different Ra displayed differences over three profiles selected along the slope. The low-Ra simulations undergo stronger variations along the flow path; this is probably due to the less developed turbulence that needs a longer path to reach a stationary regime. The conclusion of this sensitivity test is that turbulent anabatic flows in this Ra range and simplified geometry are not Rayleigh-independent.

In summary, we performed one of the first LES studies of turbulent anabatic flow. Such a numerical investigation presents several difficulties because natural convection requires accurate numerical schemes and a reliable turbulent model to be correctly reproduced. Simulations allow to analyse in detail the underlying physics of anabatic flow, to gain important knowledge for the improvement of weather prediction models and to understand the mechanisms of circulation in the lower troposphere that have the greatest impact on human activities.

Future developments

Different aspects of this work can be further investigated:

The dependency on the Ra number can be further investigated in relation to the work of Hocut, Liberzon, and Fernando (2015) on flow separation (2015) discussed in Section 3.1.1, in which the authors found independence of the length separation from the Reynolds number. Separation has not been found in the three LES analyzed in the present work. This suggests that the range in which it is possible to observe separation independence and similarity could be limited to the specific range of Hocut's work and not valid in general.

An interesting analysis related to the work of Hocut, Liberzon, and Fernando (2015) could be the investigation of the mechanisms acting in the transition between under-critical and super-critical slope angles (see Figure 3.5, p. 50). In order to observe the regime change reported in the article, different LES can be performed choosing different slope angles ranging from 15° to 30°.

The difference in background stratification defines different developments of the anabatic flows. This work treated a specific case of turbulent anabatic flow

developed in neutral background stratification. To the knowledge of the author, there is nearly no previous work in literature which makes a simulation in this configuration and there is also a lack of theoretical models able to describe it. Thus the role of neutral stratification and the behaviour under the addition of a non-zero stratification should be investigated more in depth. In order to test a numerical solution's accuracy, results of performed simulations should be verified on experimental ground. In particular, if the streamlines' separation has to be further investigated, a possible field work could be done over real slopes subjected to the diurnal cycle with the aid of thermocameras detecting the slope wind development. Thus measuring the separation length after a numerical simulation prediction, for a specified Ra range, could help test the similarity hypothesis.

Bibliography

Allen, T. and A. R. Brown (2006)
"Modeling of turbulent form drag in convective conditions". In: *Boundary-Layer Meteorol.* 118, pp. 421–429.

Arduini, G., C. Staquet, and C. Chemel (2016)
"Interactions between the nighttime valley-wind system and a developing cold-air pool". In: *Boundary-Layer Meteorology* 161, pp. 49–72.

Argyropoulos, C. and N.C. Markatos (Jan. 2015)
"Recent advances on the numerical modelling of turbulent flows". In: *Applied Mathematical Modelling* 39, pp.693–732.

Axelsen, S.L. and H. van Dop (2009a)
"Large-eddy simulation of katabatic winds, Part I: comparison with observations". In: *Acta Geophys.* 57, pp. 803–836.

Axelsen, S.L. and H. van Dop (2009b)
"Large-eddy simulation of katabatic winds, Part II: sensitivity study and comparison with analytical models". In: *Acta Geophys.* 57, pp. 837–856.

Bader, D. C. and T. B. McKee (1983)
"Dynamical model simulation of the morning boundary layer development in deep mountain valleys". In: *Journal of Climate and Applied Meteorology* 22, pp. 341–351.

Banerjee, Supratik (Nov. 2014)
"Compressible turbulence in space and astrophysical plasmas : Analytical approach and in-situ data analysis for the solar wind". PhD thesis.

Banta, R. M. (1984)
"Daytime boundary-layer evolution over mountainous terrain. Part I: observations of the dry circulations". In: *Mon. Weath. Rev.* 112, pp. 340–356.

Bonafede, M. (Nov. 2016)
"Appunti dal corso di Fondamenti di Geofisica 2". In:

Brown, R. A. (1980)
"Longitudinal instabilities and secondary flows in the planetary boundary layer: A review". In: *Reviews of Geophysics and Space Physics* 18, pp. 683–697.

Burns, P. and C. Chemel (2015)
"Interactions between downslope flows and developing cold-air pool". In: *Boundary-Layer Meteorol.* 154, pp. 57–80.

Chao, W. C. (2012)
"Correction of excessive precipitation over steep and high mountains in a GCM". In: *J. Atmos. Sci.* 69, pp. 1547–1561.

Chapman, Dean R. (1979)
"Computational Aerodynamics Development and Outlook". In:

Chemel, C., C. Staquet, and Y. Largeron (2009)
"Generation of internal gravity waves by a katabatic wind in an idealized alpine valley". In: *Meteorol. Atmos. Phys.* 103, pp. 187–194.

Cheng-Nian, X. and Inanc S. (2019)
"Stability of the Prandtl model for katabatic slope flows". In: *J. Fluid Mech* 865.

Chow, F. K., A. P. Weigel, R. L. Street, M. W. Rotach, and M. Xue (2006)
"High resolution large-eddy simulations of flow in a steep Alpine valley. part I: Methodology, verification, and sensitivity experiments". In: *J. Appl. Meteorol. Climatol.* 45, pp. 63–86.

Cintolesi, C., A. Petronio, and V. Armenio (Sept. 2015)
"Large eddy simulation of turbulent buoyant flow in a confined cavity with conjugate heat transfer". In: *Physics of Fluids* 27.

Crook, N. A. and D. F. Tucker (2005)
"Flow over heated terrain. Part I: Linear theory and idealized numerical simulations". In: *Mon. Weath. Rev.* 133, pp. 2552–2564.

De Wekker, S. F. (2008)
"Observational and numerical evidence of depressed convective boundary layer height near a mountain base". In: *J. Appl. Meteorol. Climatol.* 47, pp. 1017–1026.

Defant, F. (1951)
"Local Winds. Compendium of Meteorology". In: *American Meteorological Society*, pp. 655–672.

Egger, J. (1981)
"On the linear two-dimensional theory of thermally induced slope winds". In: *Beitrage zur Physik der Atmosphare* 54, pp. 465–481.

Ellis, A. W., M. L. Hildebrant, W. M. Thomas, and H. J. S. Fernando (2000)
"Analysis if the climatic mechanisms contributing to the summertime transport of lower atmospheric ozone across metropolitan Phoenix, Arizona, USA". In: *Clim. Res.* 15, pp. 13–31.

Everard, K., M. G. Giometto, C. Hang, M. B. Parlange, and G. Lawrence (2018)
"On the Parameterization of Turbulence in Katabatic Flow". In: *AGU Fall Meeting Abstracts* 2018, A53B–08.

Fedorovich, E. and A. Shapiro (2009a)
"Structure of numerically simulated katabatic and anabatic flows along steep slopes". In: *Acta Geophysica* 57, pp. 1895–7455.

Fedorovich, E. and A. Shapiro (2009b)
"Turbulent natural convection along a vertical plate immersed in a stably stratified fluid". In: *Journal of Fluid Mechanics* 636, pp. 41–57.

Fernando, H. J. S. (2008)
"Fluid dynamics of urban atmospheres in complex terrain". In: *Annu. Rev. Fluid Mech.* 42, pp. 365–389.

Fernando, H. J. S., S. M. Lee, J. Anderson, M. Princevac, E. Pardyjak, and S. Grossman-Clarke (2001)
"Urban fluid mechanics: air circulation and contaminant dispersion in cities". In: *Environ. Fluid Mech.* 42, pp. 365–389.

Garnier, E., P. Sagaut, and N. Adams (Jan. 2009)
Large Eddy Simulation for Compressible Flows (Google eBook), p. 276. ISBN: 9048128188.

Giometto, M. G., R. Grandi, J. Fang, Monkewitz P. A., and Parlange M. B. (2016)
"Katabatic Flow: A Closed-Form Solution with Spatially-Varying Eddy Diffusivities". In: *Boundary-Layer Meteorol.* 162, pp. 307–317.

Giometto, M. G., R. Grandi, J. Fang, P. A. Monkewitz, and M. B. Parlange (2017a)
"Katabatic flow: a closed-form solution with spatially-varying eddy diffusivities". In: *Boundary-Layer Meteorol.* 162, pp. 307–317.

Giometto, M. G., G. G. Katul, J. Fang, and M. B. Parlange (2017b)
"Direct numerical simulation of turbulent slope flows up to Grashof number $Gr = 2.1 \times 10^{11}$". In: *Journal of Fluid Mechanics* 829, pp. 589–620. DOI: 10.1017/jfm.2017.372.

Grisogono, B. and S. L. Axelsen (2009)
"A note on the pure katabatic wind maximum over gentle slopes". In: *Boundary-Layer Meteorol.* 145, pp. 527–538.

Grisogono, B., T. Jurlina, Z. Vecenaj, and I. Guttler (2014)
"Weakly nonlinear Prandtl model for simple slope flows". In: *Boundary-Layer Meteorol.* 153, pp. 1–17.

Hang, C., M. G. Giometto, H.J. Oldroyd, E. Pardyjak, and M.B. Parlange (2018)
"Similarity function for katabatic flows from field observations". In: *AGU Fall Meeting Abstracts* 2018, A31K–3022.

Hanley, K. E., D. J. Kirshbaum, S. E. Belcher, N. M. Roberts, and G. Leoncini (2011)
"Ensemble predictability of an isolated mountain thunderstorm in a high resolution model". In: *Q. J. R. Meteorol. Soc.* 137, pp. 2124–2137.

Hocut, C. M., D. Liberzon, and H. J. S. Fernando (2015)
"Separation of upslope flow over a uniform slope". In: *Journal of Fluid Mechanics* 775, pp. 266–287.

Hunt, J., H. Fernando, and M. Princevac (2003)
"Unsteady thermally driven flows on gentle slopes". In: *Journal of the Atmospheric Sciences* 59, pp. 1105–1123.

Ingel, L.K. (2018a)
"Generalization of a Prandtl Slope Flow Model with a Heavy Admixture". In: *J Appl Mech Tech Phy* 59, pp. 857–861.

Ingel, L.K. (2018b)
"On the Theory of Slope Flows". In: *J Eng Phys Thermophy* 91, pp. 641–647.

Kundu, P. K. and I. M. Cohen (2001)
Fluid mechanics. Elsevier.

Kuwagata, T. and J. Kondo (1989)
"Observation and modeling of thermally induced upslope flow". In: *Boundary-Layer Meteorology* 46, pp. 265–293.

Lebonnois, S., G. Schubert, F. Forget, and A. Spiga (2018)
"Planetary boundary layer and slope winds on Venus". In: *Icarus* 314, pp. 149–158.

Lehner, M. and C. D. Witheman (2012)
"The thermally driven cross-basin circulation in idealized bains under varying wind conditions". In: *J. Appl. Meteorol.* 51, pp. 1026–1045.

Liberzon, D. (n.d.). In: ().

Łobocki, L. (2017)
"TTurbulent Mechanical Energy Budget in Stably Stratified Baroclinic Flows over Sloping Terrain". In: *Boundary-Layer Meteorology* 164, pp. 1573–1472.

Lu, R. and R. P. Turco (1994)
"Air pollutant transport in a coastal environment. Part I: 2-D simulations of sea breeze and mountain effects". In: *J. Atmos. Sci.* 51, pp. 2285–2308.

Moroni, M. and A. Cenedese (2015)
"Laboratory Simulations of Local Winds in the Atmospheric Boundary Layer via Image Analysis". In: *Advances in Meteorology* 2015.

Nielsen, Peter and Ian Teakle (Jan. 2011)
"Differential Diffusion: Often a Finite-Mixing Length Effect". In:

Nillson, H (n.d.)
How to implement your own application. URL: `http://www.tfd.chalmers.se/~hani/kurser/OS_CFD_2008/implementApplication.pdf`.

Noppel, H. and F. Fiedler (2002)
"Mesoscale Heat Transport Over Complex Terrain By Slope Winds – A Conceptual Model And Numerical Simulations". In: *Boundary-Layer Meteorology* 104, pp. 1573–1472.

Oldroyd, H. J., E. R. Pardyjak, C. W. Higgins, and M. B. Parlange (2016)
"Buoyant turbulent kinetic energy production in steep-slope katabatic flow". In: *Boundary-Layer Meteorol.* 161, pp. 405–416.

Oliveira, P.J. and R.I. Issa (2001)
"an improved piso foam algorithm for the computation of buoyancy-driven flows". In: *Numerical Heat Transfer, Part B: Fundamentals* 40.6, pp. 473–493.

OpenFOAM (n.d.)
OpenFOAM v6 User Guide: 4.4 Numerical schemes. URL: `https://cfd.direct/openfoam/user-guide/v6-fvschemes/`.

Orville H, D. (1964)
"On mountain upslope winds". In: *Journal of the Atmospheric Sciences* 21, pp. 622–633.

Pan, N., Y. Li, Y. Fan, W. Ma, J. Huang, P. Jiang, and S. Kong (2017)
"Structural Optimization of the Retractable Dome for Four Meter Telescope (FMT)". In: *Publications of the Astronomical Society of the Pacific* 129.

Piomelli, U. (Jan. 2018)
"Large-Eddy Simulation of turbulent flows: Part 1: Introduction". In: ISBN: 9782875161369.

Politovich, M. K., R. K. Goodrich, C. S. Morse, A. Yates, R. Barron, and S. A. Cohn (2011)
"The Jueau terrain-induced turbulence alert system". In: *Bull. Atm. Meteorol. Soc.* 92, pp. 299–313.

Prandtl, L. (1942)
"Fuhrer durch die Stromungslehre". In: *Veweg und Sohn*, pp. 373–375.

Princevac, M. and H. J. S. Fernando (2008)
"Morning break-up of cold pools in complex terrain". In: *J. Fluid Mech* 616, pp. 99–109.

Princevac, M., J. C. R. Hunt, and H. J. S. Fernando (2008)
"Quasi-steady katabatic winds on slopes in wide valleys: hydraulic theory and observations". In: *J. Atmos. Sci.* 65, pp. 627–643.

Reuten, C., D. G. Steyn, and S. E. Allen (2007)
"Water tank studies of atmospheric boundary layer structure and air pollution transport in upslope flow systems". In: *J. Geophys. Res.* 112.

Saeedipour, Mahdi, Simon Schneiderbauer, Stefan Pirker, and Salar Bozorgi (Sept. 2014)
"Numerical simulation of turbulent liquid jet breakup using a sub-grid criterion with industrial application". In:

Schumann, U. (1990)
"Large-eddy simulation of the up-slope boundary layer". In: *Quarterly Journal of the Royal Meteorological Society* 116, pp. 637–670.

Segal, M., Y. Ookuchi, and R. A. Pielke (1987)
"On the effect of steep slope orientation on the intensity of daytime upslope flow". In: *Journal of the Atmospheric Sciences* 122, pp. 3587–3592.

Serafin, S. and D. Zardi (2010a)
"Daytime heat transfer processes related to slope flows and turbulent convection in an idealized mountain valley". In: *J. Atmos. Sci.* 67, pp. 37939–3756.

Serafin, S. and D. Zardi (2010b)
"Structure of the atmospheric boundary layer in the vicinity of a developing upslope flow system: a numerical model study". In: *J. Atmos. Sci.* 67, pp. 1179–1185.

Shapiro, A. (June 2012)
"Theory of Slope Flows and Low-Level Jets diffusion". In:

Shapiro, A. (2016)
"a unified theory for the great plains nocturnal low-level jet". In: *J. Atmos. Sci.* 73, pp. 3037–3057.

Shapiro, A. and E. Fedorovich (2008)
"Coriolis effects in homogeneous and inhomogeneous katabatic flows". In: *Q. J. R. Meteorol. Soc.* 134, pp. 353–370.

Shapiro, A. and E. Fedorovich (2014)
"A boundary-layer scaling for turbulent katabatic flow". In: *Boundary-Layer Meteorol.* 153, pp. 1–17.

Shapiro, A. and E. Fedorovich (2017)
"Oscillations in Prandtl slope flow started from rest". In: *Q. J. R. Meteorol. Soc.* 143, pp. 670–677.

Shapiro, A. and Evgeni Fedorovich (2003)
"Unsteady convectively driven flow along a vertical plate immersed in a stably stratified fluid". In: *Journal of Fluid Mechanics* 498, pp. 333–352.

Shapiro, A. and Evgeni Fedorovich (2004)
"Unsteady convectively driven flow along a vertical plate immersed in a stably stratified fluid". In: *Journal of Fluid Mechanics* 498, pp. 333–352.

Skyllingstad, E. D. (2003)
"Large-eddy simulation of katabatic flows". In: *Boundary-Layer Meteorol.* 106, pp. 217–243.

Smith, C. M. and E. D. Skyllingstad (2005)
"Numerical simulation of katabatic flow with changing slope angle". In: *Mon. Weath. Rev.* 133, pp. 3065–3080.

Spalding, D. B. (1961)
"A Single Formula for the "Law of the Wall"". In: *Journal of Applied Mechanics* 28.3, pp. 455–458.

Tampieri, F. (Sept. 2013)
"Planetary boundary layer and turbulent diffusion". In:
Welch, P. (1967)
"The use of fast Fourier transform for the estimation of power spectra: A method based on time averaging over short, modified periodograms". In: *IEEE Transactions on Audio and Electroacoustics* 15.2, pp. 70–73.
Wenger, R. (1923)
"Neue Theorie der Berg-und Talwindes". In: *Meteorogische Zeitshrift* 40, pp. 193–204.
Ye, Z. J., M Segal, and R. R. Pielke (1987)
"Effects of atmospheric thermal stability and slope steepness on the development of daytime thermally induced upslope flow". In: *Journal of the Atmospheric Sciences* 44, pp. 3341–3354.
Zardi, D. and S. Serafin (2015)
"An analytic solution for time-periodic thermally driven slope flows". In: *Q. J. R. Meteorol. Soc.* 141, pp. 1968–1974.

Acknowledgements

Grazie alla prof. Silvana per aver avuto fiducia in questo lavoro e avermi dato motivazione quando ce n'è stato bisogno.

Grazie a Carlo di aver mantenuto così a lungo la pazienza con la mia inesperienza.

Grazie ai miei genitori per aver investito su di me per tutto questo tempo.

Grazie a mia sorella di continuare a chiamarmi fratello.

Grazie a Francesco, Melissa, Giacomo, Gianluca e Costanza, perché comunque cambino le cose restate sempre i miei punti di riferimento, sappiate che io resterò sempre il vostro.

Grazie a Letizia e Martina di esistere, perché siete il mio mondo, e il bene che vi voglio mi insegna il modo di volere anche un po' più bene a me stesso.